Radio observations as a tool to study shock interactions and mass ejections in novae

Mumbua Nyamai

NYMMIR001

Thesis presented for the Degree of

DOCTOR OF PHILOSOPHY

in the Department of Astronomy

UNIVERSITY OF CAPE TOWN

Supervisors: Prof. P. A. Woudt, Dr. V. A. R. M. Ribeiro, Prof. L Chomiuk

05 February 2021

AUTHOR'S DECLARATION

I, Mumbua Nyamai hereby declare that the work in this thesis, except for that which is properly acknowledged is my original work. I also declare that the whole thesis nor any part of it has been submitted to any other institution for another degree. The work presented in this thesis that has been done in collaboration with others has been acknowledged. I grant the university permission to reproduce either the whole or any part of this thesis for the purposes of research.

SIGNED: ..... Signed by candidate ..... DATE: .....05 FEBRUARY 2021.....

Mumbua Nyamai
NYMMIR001
Degree Name
Astronomy
University of Cape Town
South Africa

I confirm that I have been granted permission by the University of Cape Town Doctoral Degrees Board to include the following publication(s) in my PhD thesis, and where co-authorships are involved, my co-authors have agreed that I may include the publication:

Radio light curves and imaging of the helium nova V445 Puppis reveal seven years of synchrotron emission by M M Nyamai, L Chomiuk, V A R M Ribeiro, P A Woudt, J Strader, K V Sokolovsky, 2021, MNRAS, 501, 1394.

Abstract

This thesis presents radio frequency studies of three novae, namely V445 Puppis, V3890 Sagitarii and V339 Delphini. The new data, in this thesis, represent some of the most detailed and comprehensive radio light curves to date. In these systems a thermonuclear eruption occurs on the surface a white dwarf following extensive periods of accretion of material from a companion star. The result of the thermonuclear eruption is the explosive ejection of the outer layers of the accumulated material. Since the ejected material emits at radio wavelengths at some point in its evolution, radio data obtained for the three objects are utilised to test the hypothesis of radio emission models.

First, radio data of V445 Pup are presented. V445 Pup is the only helium nova observed to date; its eruption in late 2000 showed high velocities up to 8500 km s^{-1}, and a remarkable bipolar morphology cinched by an equatorial dust disc. Here we present multi-frequency radio observations of V445 Pup obtained with the Very Large Array (VLA) spanning 1.5 – 43.3 GHz, to 2001 January and 2008 March (~ 89 – 2700 days after eruption). The radio light curve is dominated by synchrotron emission over these seven years, and shows four distinct radio flares. Resolved radio images obtained in the VLA's A configuration show that the synchrotron emission hugs the equatorial disc, and comparisons to near-IR images of the nova clearly demonstrate that it is the densest ejecta—not the fastest ejecta—that are the sites of the synchrotron emission in V445 Pup. The data are consistent with a model where the synchrotron emission is produced by a wind from the white dwarf impacting the dense equatorial disc, resulting in shocks and particle acceleration. The individual synchrotron flares may be associated with density enhancements in the equatorial disc and/or velocity variations in the wind from the white dwarf. This overall scenario is similar to a common picture of shock production in hydrogen-rich classical novae, but V445 Pup is remarkable in that these shocks persist for almost a decade, much longer than the weeks or months for which shocks are typically observed in classical novae.

Second, the radio observations following the 2019 August eruption of V3890 Sgr obtained with the MeerKAT radio telescope at 1.28 GHz are presented. The radio light curve spans from day 1 to 300 after discovery and is dominated by synchrotron emission produced as the expanding ejected nova envelope interacts with the dense wind from an evolved companion in the binary system.

The radio emission is detected early on day 6 and increases rapidly with the radio flux peaking after day 15. The radio luminosity increases due to a decrease in the opacity of the circumstellar material in front of the shocked material and fades as the density of the surrounding medium decreases and the velocity of the shock losses energy and decelerates. Modelling of the light curve provides an estimated mass-loss rate of $M_{\rm wind} \approx 10^{\dot{-}8}$ M$_\odot$ yr^{-1} for the red giant wind. V3890 Sgr hosts a massive white dwarf, shows presence of structured circumbinary material consistent with the surrounding environment present in some supernovae type Ia (SNe Ia) and therefore it is possible to be a SNe Ia progenitor.

Finally, radio observations of V339 Del obtained using the Karl G. Jansky Very Large Array and the Arcminute Microkelvin Imager Large Array (AMI) following the 2013 eruption are presented. The AMI data were obtained every two days resulting in the most detailed radio light curve of a classical nova known to date. The radio data are used to test the hypothesis that the observations were due to a bipolar shaped ejecta as suggested from emission line modelling at optical wavelength. Here, the morphology is utilised in predicting the ejected mass of V339 Del during the eruption. The radio light curve is modelled in the morpho-kinematical program SHAPE using a linearly expanding ionized ejecta, assuming that the nova emission is dominated by thermal free-free emission. Considering a bipolar geometry for the nova ejecta, the radio light curve fluxes can be replicated using an ejected mass of $M_{\rm ej} \approx 0.1 - 8 \times 10^{-5}$ M$_\odot$. The mass estimate of the ejecta compares well with estimates of emission line modelling in optical spectroscopy and also γ-ray emission modelling. High resolution radio images of V339 Del obtained with the VLA's A configuration initially show a spherical structure when the ejecta is optically thick and later a ring structure when the ejecta is optically thin. The change in optical depth and apparent morphology is a further indication of a non-spherical geometry. V339 Del shows evidence of shock powered emission in the first 100 days after the nova eruption.

This thesis emphasizes the role of radio data towards a better understanding of the effects of thermonuclear eruptions in novae. This work highlights the importance of obtaining well sampled radio light curves of novae which give more insight into the physical processes that follow nova explosions, which may have been overlooked before due to sparsely sampled radio light curves. Resolved radio images of novae are also crucial in determining the morphology of the ejecta hence provide clues on the approach to modelling radio emission from novae. This is particularly relevant given the new generation of sensitive radio telescope arrays such as MeerKAT, the next generation Very Large Array, and ultimately the Square Kilometre Array.

Dedication and Acknowledgements

Dedication

Thank you to my parents Nyamai and Wavinya, my siblings Malinda, Mutheu, Mumo, Muuo, for believing in me and your prayers. Your encouragements allowed me to pursue this Doctorate degree.

I would like to thank my team of supervisors, Prof Patrick Alan Woudt (UCT), Dr Valério A. R. M. Ribeiro (Instituto de Telecomunicações and Universidade de Aveiro) and Prof Laura Chomiuk (Michigan State University). You were a wonderful and inspirational team, you shared your knowledge with a lot of patience, thank you. I thank Prof Woudt for giving me the opportunity to conduct this research at the department and providing me with the resources which made the work possible. I especially recognise the very many hours dedicated by Prof Chomiuk in teaching me radio data reduction techniques via video conferencing even when you were not in a position to. I appreciate the professional assistance of Dr Ribeiro on technical and programming issues.

I gratefully appreciate Dr Chelsea Harris, Dr Kirill V. Sokolovsky and Prof Jay Strader, for the professional assistance when I was working on chapter 2. I appreciate Prof Rob Fender and Dr Gemma Anderson for providing the AMI data for V339 Del. I acknowledge the work of Dr James Allison in assisting me with the H I absorption data analysis in chapter 3. Thank you Dr Sumit K. Sarbadhicary for your professional assistance when I was doing modelling in chapter 3. I appreciate sincerely the effort of Dr Willice O. Obonyo in assisting me with programming issues.

To: William, Estelle, Ani, Kerry, Julia, Evelyn, Robyn, Sambatriniaina: **Thank you for the wonderful moments I had in Cape Town**.

Acknowledgements

This research was funded by the South African Radio Astronomy Observatory (SARAO) which is a facility of the National Research Foundation (NRF), an agency of the Department of Science and Innovation, bursary from the department of Astronomy, University of Cape Town (UCT) and by NRF SARChI Grant 111692.

I am very grateful to Prof Joanna Mikolajewska for hosting me at Nicolaus Copernicus Astronomical Center, Dr Ribeiro for hosting me at Universidade de Aveiro and Prof Chomiuk for hosting me at Michigan State University for research visits during my studies. In October 2019 I attended the European Radio Interferometry School (ERIS) in Gothenburg, Sweden. These research visits were made possible through funding from SARAO, the NRF, the financial support from the Fundação para a Ciência e a Tecnologia (FCT) in the form of an exploratory project of reference IF/00498/2015/CP1302/CT0001, FCT and the Ministério da Ciência, Tecnologia e Ensino Superior (MCTES) through national funds, the National Science Foundation (NSF) grant AST-1751874 and the Polish NCN grant DEC-2013/10/M/ST9/00086 to Prof Mikolajewska.

This research has made use of the VLA radio telescope data operated by the National Radio Astronomy Observatory (NRAO). The NRAO is a facility of the National Science Foundation operated under cooperative agreement by Associated Universities, Inc. The MeerKAT radio telescope data used in this resarch were obtained under the programmes SCI-20190418-MN-01 and DDT-20200323-MN-01. The MeerKAT is operated by SARAO, which is a facility of the NRF. MeerKAT data was processed in the Inter-university Institute for Data Intensive Astronomy (IDIA). I acknowledge with thanks the variable star observations from the AAVSO International Database contributed by observers worldwide. Some of the optical data from this database was used in this research for one of the targets studied in this thesis.

TABLE OF CONTENTS

List of Figures

Figure **Page**

List of Tables

Table **Page**

CHAPTER 1

INTRODUCTION

Novae were known historically as either 'new stars' or 'guest stars' due to their sudden appearance in the sky and fading away within a period of days to weeks (a historical perspective is presented by Duerbeck, 2008). Guest stars were observed by East Asian astronomers ≈ 2500 years ago (Stephenson, 1976). Indeed modern observations have matched some historically known guest stars to nova events (Miszalski et al., 2016; Shara et al., 2017; Hoffmann et al., 2020).

Today, novae are known as being due to a thermonuclear runaway (TNR) on the surface of an accreting white dwarf. These eruptions are a result of periods of extensive accretion of material onto a white dwarf in close orbit with a less evolved companion star in a Cataclysmic Variable (CV) system, or a closely related system (see §1.1). The mode of accretion can either be Roche lobe overflow or stellar wind from the secondary star (more details in §1.1.3).

The TNR-powered eruption results in a change in brightness (commonly referred to as outburst amplitude) between 8 to 14 magnitudes at optical wavelengths within hours to days following the eruption (see reviews by Hellier, 2001; Warner, 2008). Novae are the most common explosions in the local universe but less energetic compared to other stellar explosions such as supernovae and gamma-ray bursts. Novae are ideal systems to study accretion, nuclear burning, and explosive mass ejection processes in general. Some specific cases present possibilities to study the shaping of the nova ejecta (see §1.2.5). Novae emit at all wavelengths including at radio frequencies at some point in their evolution.

Radio light curves of novae have been used to trace the radio emitting photosphere from months to years after optical discovery (e.g., Seaquist & Palimaka, 1977; Hjellming et al., 1979; Seaquist & Bode, 2008). The light curves are modelled assuming that the nova remnant is emitting thermal free-free emission (see §1.3.2). The thermal radio models are crucial in estimating the mass of the ejected envelope and kinetic energy of the eruption. Early models assumed a spherical outflow with a uniform density distribution ejected instantaneously (e.g., Seaquist & Palimaka, 1977; Hjellming et al., 1979). However, mass ejections in novae are not simplistic and the parameters estimated from modelling radio emission depend on the assumptions made (Ribeiro et al., 2014; Nelson et al., 2014; Wendeln et al., 2017).

Detailed structures of nova remnants are often identified through optical and radio imaging and/or models of well sampled radio light curves (e.g., Heywood et al., 2005). Some novae show the presence of jets and evidence of delayed mass ejections based on radio data analysis (Sokoloski et al., 2008; Nelson et al., 2014) and resolved optical images of novae show the presence of clumps in the ejecta (Moraes & Diaz, 2011; O'Brien & Bode, 2008). Evidence exists that ejecta mass estimates from radio observations are either one order of magnitude higher than theoretical predictions or a few times more (e.g., Yaron et al., 2005; Roy et al., 2012). Since simple spherical models do not necessarily account for these features, suggestions are that non-uniformity in the nova shells and non-spherical outflows are some of the culprits for the discrepancies (e.g., Ribeiro et al., 2014; Wendeln et al., 2017). The aim of this research is, therefore, to incorporate some of these features in radio observation modelling, based on three of the best sampled radio light curves of novae to date.

1.1 Cataclysmic Variables

A Cataclysmic Variable (CV) is a binary system that consists of a white dwarf (primary) and a less evolved secondary star classified as a K–M dwarf that losses its mass to the compact object (Warner, 1995; Knigge et al., 2011). The basic structure of a CV is shown in Figure 1.1. Some variations can occur such that the secondary star can be a red giant (symbiotic stars) or another white dwarf/helium star (AM CVn), see §1.1.2 for more details. The mass accretion onto the white dwarf from the secondary star results in a broad range of outbursts including novae (see §1.2) and dwarf novae (Warner, 1995). The latter are associated with thermal viscous instabilities in the accretion discs of CVs (Hameury, 2020).

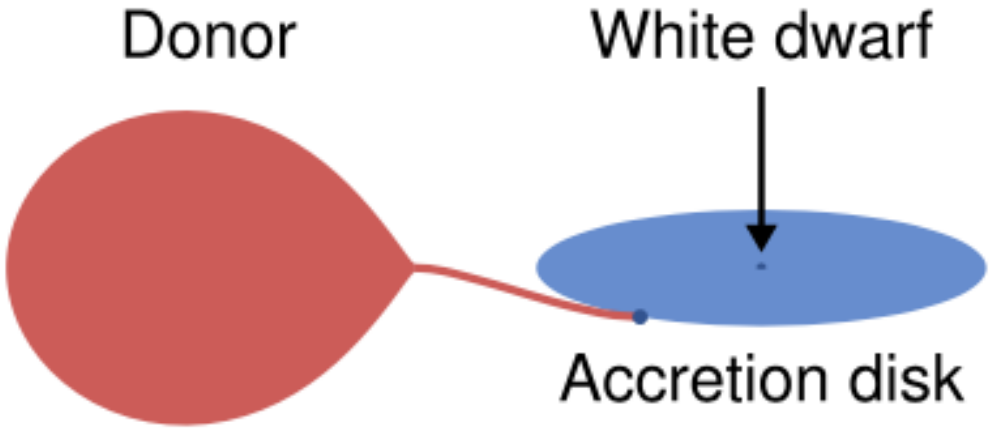

Figure 1.1: A sketch of a Cataclysmic Variable binary system. The secondary star (donor) fills its Roche lobe and transfers matter to the primary star (white dwarf) via the inner-Lagrangian point (L1) to form an accretion disc. Image credit: Philip D. Hall.

1.1.1 Overview of basic aspects of cataclysmic variables

The formation of a CV starts with a massive primary star in a wide binary system with a less massive secondary star. Before the formation of a CV, the individual stars evolve on their own first.

The primary star evolves into a red giant, filling its Roche lobe, and its envelope engulfs the whole binary in a common envelope phase (e.g., Paczynski, 1976). A fraction of original energy and momentum is retained in the emerging close binary and the envelope is ejected as the stars orbit closer to each other. The post common envelope evolution phase is therefore of a semi-detached binary with a core of a white dwarf and a low-mass main sequence star. A CV will form through further loss of angular momentum of the binary system by either gravitational radiation or magnetic braking (Paczynski & Sienkiewicz, 1981; Verbunt & Zwaan, 1981). Mass transfer to the white dwarf is initiated when the main sequence star fills its Roche lobe.

A white dwarf is a dense star supported by electron degeneracy pressure. Its formation starts with stars of masses < 10 $M_{\odot}$ on the main sequence track of the Hertzsprung-Russell (HR) Diagram, (Figure 1.2), where the stars fuse hydrogen into helium in the cores at temperatures of $\sim 10^7$ K (e.g., Irwin, 2007). During this stage the star is in hydrostatic equilibrium. As hydrogen is exhausted in the core, the

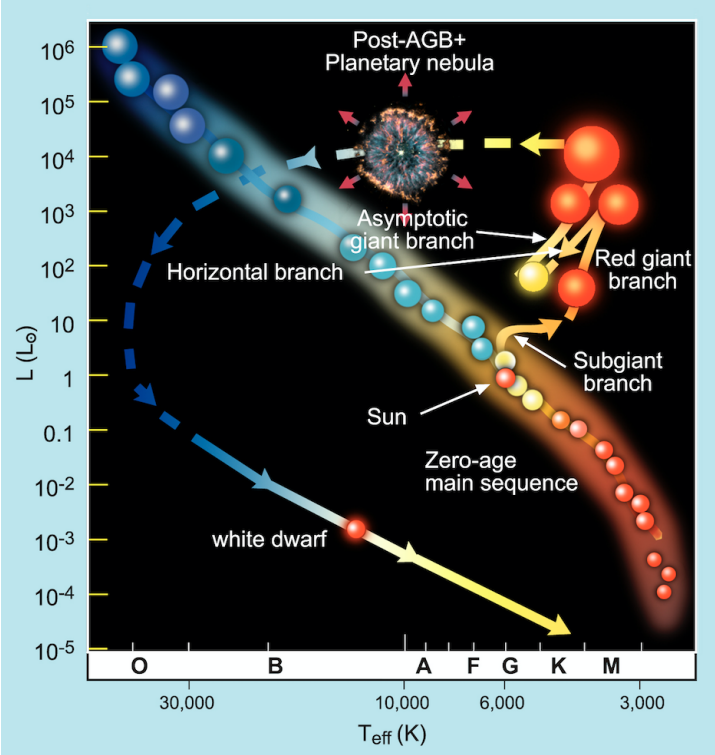

Figure 1.2: The H-R diagram, reproduced from Jose (2016). The theoretical diagram shows the evolution of a Sun-like main sequence star to the white dwarf stage by comparing the star's temperature and luminosity.

surrounding layers start hydrogen shell burning, causing the star to increase in size, becoming a red giant. The core at this stage is contracting and its temperature rises to $\sim 10^8$ K. The high temperatures together with high densities, $\sim 10^3$ g cm^{-3}, make ideal conditions for fusion of helium to heavier elements including carbon.

When the star exhausts the helium in the core, it evolves to the Asymptotic Giant Branch (AGB) phase of the HR diagram where it loses the outer layers, forming a cloud of gas surrounding the star (the so-called planetary nebulae). Once the cloud dissipates, it leaves behind a white dwarf where fusion does not take place anymore (Koester & Chanmugam, 1990). The initial mass of the main sequence star determines how many burning stages it will undergo. For example, a carbon-oxygen (CO) rich white dwarf progenitor is a $7-8$ M$_\odot$ star that undergoes hydrogen and helium burning while a ~ 10 M$_\odot$ star will undergo hydrogen, helium and carbon burning phases to form an oxygen-neon (ONe) rich white dwarf (Hernanz, 2005; Jose, 2016).

The mass of a white dwarf is compressed in a compact object the size of the Earth, hence it is very dense and is kept intact by electron degeneracy pressure (e.g., Koester & Chanmugam, 1990). In 1931, Subrahmanyan Chandrasekhar determined that for a white dwarf not to collapse against its own gravitational potential, it cannot exceed $M_{ch} \sim 1.4$ M$_\odot$, the so called the *Chandrasekhar limit* (Chandrasekhar, 1931). At and above this limit, the fate of the white dwarf depends on its chemical composition. If its core is rich in carbon and oxygen, an increase in mass due to accretion from a close companion star could increase the pressure and temperature, more nuclear reactions could eventually ignite the core, and thus it could explode as a type Ia supernova (Hoyle & Fowler, 1960). However, for an oxygen-neon rich core, the star will collapse into a neutron star, as it ignites at extreme densities exceeding that required for gravitational collapse (Gutierrez et al., 1996).

1.1.2 Related objects

Closely related to CVs are symbiotic binaries (Mikolajewska, 2010) and AM CVn stars (e.g., Solheim, 2010). The donor stars in symbiotic binaries are evolved compared to those in CVs and exhibit a different mechanism of mass transfer, namely via a stellar wind (see §1.1.3). A red giant star consists of an inert helium core surrounded by a hydrogen burning shell, and a giant envelope reaching the size of $100 - 1000$ R$_\odot$ (Jose, 2016).

A helium star is a hydrogen-deficient star that is actively burning helium (Iben & Tutukov, 1991). A helium star and white dwarf binary is formed via two common envelope phases, from two stars of mass comparable to each other born in close orbit (Iben & Tutukov, 1994). Here the primary star fills its Roche lobe when it evolves to the AGB phase, while the companion star fills its Roche lobe when it evolves to its red giant phase. During the common envelope phases, most of the energy is released to the envelope which is expelled, leaving behind a helium star and a white dwarf in close orbit (Iben & Tutukov, 1994).

1.1.3 Mass transfer in CVs and related objects

Mass transfer in CVs and related objects such as symbiotic binaries and AM CVn stars occurs via Roche lobe overflow or the stellar wind. The surface of equal gravitational potential, known as the equipotential surface, surrounds both the primary and secondary star, forming a Roche lobe around each star as shown in Figure 1.3. When the secondary star fills its Roche Lobe, matter moves through the inner Lagrangian point (L_1 in Figure 1.3), into the Roche Lobe of the primary star: a mechanism known as Roche Lobe

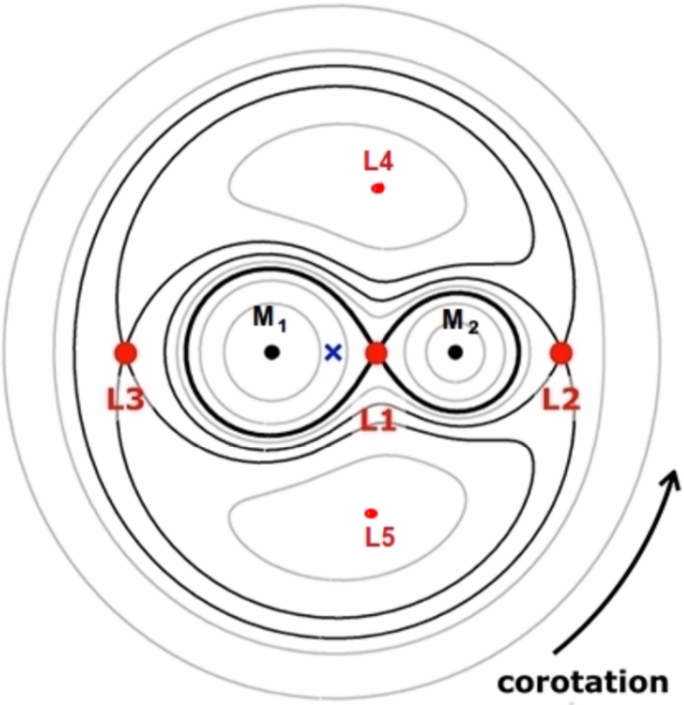

Figure 1.3: An illustration of equipotential surfaces around two stars with masses M_1 and M_2, which intersect at L_1 point. Illustration reproduced from Lamers & Levesque (2017).

overflow (Warner, 1995). Once inside the Roche lobe of the primary star, the matter does not fall directly on the primary star, but rather forms an accretion disc around it, since the material possesses high angular momentum (see Figure 1.1).

The mass transfer in symbiotics occurs via the companion's dense stellar wind. In these systems the secondary star does not necessarily fill its Roche lobe, but material is accreted onto the surface of the white dwarf via the wind emitted from the secondary (Iben, 2003). This mode of accretion produces a dense circumstellar medium surrounding the binary, and in some cases material that escapes from the L3 point concentrates in the equatorial plane of the binary system to form shells (Mohamed et al., 2013).

1.2 Novae

1.2.1 Thermonuclear runaway process

Nova eruptions powered by hydrogen burning are divided into classical novae and recurrent novae. The difference between classical and recurrent novae is related to whether one or more eruptions have been

observed.

All known novae to date have occurred as a result of hydrogen burning on the surface of the white dwarf, except for one confirmed helium nova, which is understood to be a result of helium burning on the surface of a white dwarf (e.g., Lynch et al., 2004; Woudt & Steeghs, 2005). The white dwarf outer envelope grows in mass and increases in density as the accreted H-rich material continues to accumulate. The bottom layers become hot as the material is compressed by the surface gravity of the white dwarf (e.g., José, 2012). As a result of increased temperatures and densities, nuclear burning sets in through proton-proton (pp) chain reactions and the carbon, oxygen, nitrogen (CNO) cycle, depending on the temperature levels (e.g., Starrfield, 1996; Starrfield et al., 2016). At the start of the accretion process, when temperatures are low, $\sim 10^6$ K, the pp chain reactions dominate the nuclear energy production (e.g., Starrfield et al., 2016). During this process, which also includes the *pep* reaction, hydrogen is converted to helium through fusion, producing a lot of energy at a rate of $\propto T^4$ (Adelberger et al., 2011; Jose, 2016). As the energy released continues to heat the material, it is expected that the material should expand to accommodate the energy produced via nuclear reactions.

However, the material is electron degenerate, i.e. $P \propto \rho^\gamma$, which means that pressure (P) does not depend on temperature (T), instead it depends only on density (ρ) or volume (V). The increase in temperature therefore does not increase the pressure nor the volume, but catalyses more nuclear reactions: a process known as a thermonuclear runaway (TNR; Gallagher & Starrfield, 1978; Starrfield, 1996). At high temperatures, $\sim 2 \times 10^8$ K, the CNO cycle overtakes the pp chain reactions and becomes the main source of energy (Kovetz & Prialnik, 1997). The cycle makes use of carbon, nitrogen, and oxygen as catalysts to burn hydrogen to helium. The energy production rate increases exponentially as $\propto T^{16}$ and the envelope becomes convective (Starrfield, 1996). During the TNR process, the energy generation is limited by the unstable β^+ decay nuclei produced. The convection in the envelope, therefore helps transport fresh CNO nuclei for continued nuclear burning.

The envelope now freely expands as the temperature increases. The ejected envelopes of the currently known novae consist of material of masses in the range of 10^{-8} to 10^{-3} $M_\odot$ expanding at various velocities in the range of 100 km s^{-1} $< V_{ej} \leq$ 10,000 km s^{-1} (Gallagher & Starrfield, 1978; Anupama et al., 2013; O'Brien et al., 2015). In addition to the production of unstable nuclei, the TNR processes also produce CNO isotopes ^{13}C, ^{17}O, and ^{15}N. It has been shown that novae contribute significantly to these abundances in the Milky Way (Heywood et al., 2005; Starrfield et al., 2016; Jose, 2016).

Helium novae are thermonuclear eruptions that result from helium burning on the surface of a white dwarf following accretion of He-rich material from a helium star (Kato et al., 1989). Helium burning to carbon and oxygen occurs through the triple-α reaction, which occurs at temperatures greater than 10^8 K (see §2.4.2 in Jose, 2016).

1.2.2 Mass loss during a nova eruption

Several mechanisms drive mass loss following a nova eruption. These mechanisms could either be a single impulsive event, a common envelope phase, multiple ejections or a combination of some of these processes. As illustrated in Figure 1.4, the general nova evolution process begins with the TNR and expansion of the envelope (stage [a] of Figure 1.4). Next, the expanding nova shell engulfs the whole binary in a phase resembling common envelope evolution (stage [b] of Figure 1.4). This is followed by continuous flow of material, in the form of an optically thick wind powered by radiation pressure (stage [c]; Bath & Shaviv, 1976; Hachisu & Kato, 2006). The motion of the binary system contributes to the shaping of the ejected envelope as the binary motion accelerates the less dense material to flow towards the polar regions and more dense material to align along the equatorial regions, forming a bipolar outflow (Livio et al., 1990; Lloyd et al., 1997). This concept has been supported by spectroscopic studies of nova envelopes, optical imaging and radio imaging as some of the observed nova ejecta morphologies are bipolar (McLaughlin, 1964; Woudt et al., 2009; Chomiuk et al., 2014).

Material from nova eruptions could also be lost via the multiple ejection scenario. Near infrared (NIR) images have revealed the presence of polar blobs in V445 Pup, that resulted from post eruptions event and occurred at least a year after the initial TNR process (Woudt et al., 2009). Modelling of radio light curves of T Pyx revealed a delayed mass ejection on day 76 after the initial nova eruption (Nelson et al., 2014). The correlation between optical flares and absorption features in the spectra of ASASSN-17pf indicates the presence of discrete episodes of mass ejections (Aydi et al., 2019). These are case examples that show mass ejection can occur in multiple episodes during a single eruption.

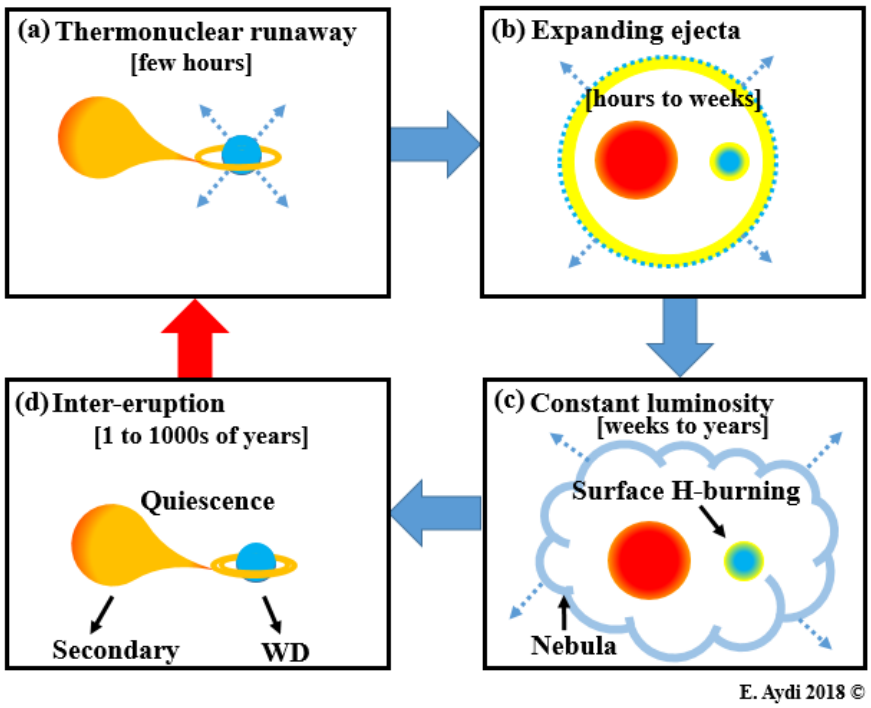

Figure 1.4: An illustration of the evolution of nova starting from the TNR process to quiescence. Reproduced from Aydi (2018) with permission from the author.

1.2.3 Observational characteristics

1.2.3.1 Optical light curves of novae

Photometric measurements of novae are normally presented as optical light curves which can be analysed for different features as the nova evolves. A typical light curve showing different stages of the nova evolution is shown in Figure 1.5 (McLaughlin, 1939). Following the initial eruption, the brightness increases rapidly to maximum on a timescale of hours. This rise is not expected to be smooth as there is usually a pause at $\leq$ 2 magnitudes before the peak brightness, referred to as the pre-maximum halt (Hounsell et al., 2010). Following the maximum peak, there is a fast initial decline followed by a slow final decline (Warner, 2008). During the initial decline phase, the brightness drops by 3 to 4 mag, and is characterised by either a smooth curve common in fast novae or variations in magnitudes that are present in slow novae (Warner, 1995).

Classification schemes used to classify novae are based on the decline time and light curve characteristics (Payne-Gaposchkin, 1964; Strope et al., 2010). The most used decline time classification scheme is that put forward by Cecilia Payne-Gaposchkin. This classification is defined in terms of t_2 and t_3 (by

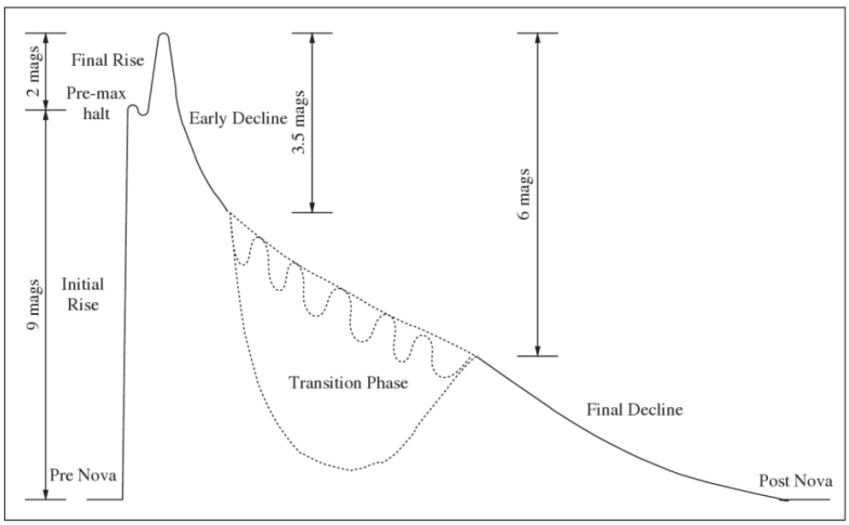

Figure 1.5: The expected shape of a nova light curve in the optical wavelengths (McLaughlin, 1939).

Table 1.1: Speed class of novae based on time taken to dim by 2 and 3 magnitude in the optical (Payne-Gaposchkin, 1964).

Class	t_2 (days)	t_3 (days)
Very fast	<10	<20
Fast	<11 - 25	20 - 49
Moderately fast	26 - 80	50 - 140
Slow	81 - 150	141 - 264
Very slow	150 - 250	265 - 440

extension), the duration in days it takes for the nova brightness to decrease by 2 and 3 magnitudes from the peak magnitude, respectively (Payne-Gaposchkin, 1964; Warner, 1995). Based on their respective t_2 and t_3 (where t_3 is also defined as $t_3 \approx 2.75\ t_2^{0.88}$ by Warner, 1995), novae are divided into five classes, listed in Table 1.1.

The decline phase of the optical light curve shows a range of behaviours. This decline behaviour can also be used to classify nova light curves as shown in Figure 1.6 (Strope et al., 2010). The result is seven classes of novae which include the flat-topped (F), cusp like secondary maximum (C), flares or jitters (J), plateau (P), oscillations (O), smooth decline (S) and dust minima (D) classes.

A smooth decline is observed in most novae and is expected for a nova ejecta that is expanding uniformly where its luminosity is powered by nuclear burning from the white dwarf. The optical emission declines because the emitting photosphere recedes towards the compact object (Gallagher & Starrfield, 1976).

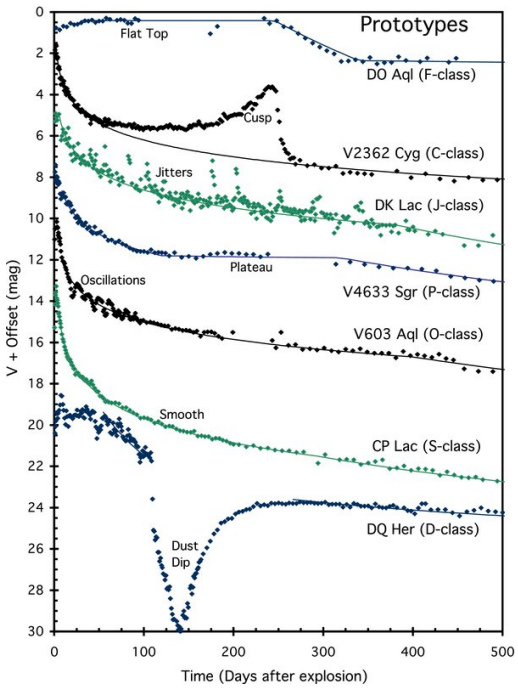

Figure 1.6: A representation of the seven groupings of nova optical light curves put forward by Strope et al. (2010) based on the behaviour of the optical light curve after the maximum. Each light curve represents a different class of novae.

Oscillations and jitters in novae light curves are observed when the emitting region expands temporarily (Tanaka et al., 2011). These features are shown to occur due to either distinct mass loss episodes from the nova, expanding clumpy ejecta following an eruption or internal shocks within the nova ejecta (Munari et al., 2015; Williams, 2016; Aydi et al., 2020). Progress is been made to explain some of the complex features observed in optical light curves in novae but there is still lack of plausible models for most of them.

The D class of novae, for example V705 Cas, show declines in their light curves of about 7 – 10 mag as a result of dust formation (Hric et al., 1998). In addition, there is evidence of dust in the form of excess emission at near infrared wavelengths. This is the result of dust grains absorbing the optical light and re-emitting the radiation at NIR wavelengths (e.g., Hyland & Neugebauer, 1970). More details on dust formation in novae are presented in §1.2.3.5. Eventually, the nova slowly emerges from the dust obscuration and continues its slow decline towards quiescence. The final fading of the nova takes years to reach the pre-nova brightness, and in some novae the emission from the surrounding nebula can be separated from that emerging from the underlying binary (see details in §1.2.5).

1.2.3.2 Optical spectra of novae

Spectroscopically, novae have been classified into two major categories based on the presence of Balmer emission lines (common to all novae except V445 Pup), in addition to abundance of either iron emission lines (Fe II class) or helium and nitrogen emission lines (He/N class) (Williams, 1992). Nova spectra can be dominated by absorption or emission lines—or profiles consisting of blue-shifted absorption and redder emission (usually known as P Cygni profiles) at different stages of the optical light curve evolution. A detailed description of the spectral behavior of novae is given in Warner (2008). A P Cygni profile is evidence of a wind or ejecta expanding away from the binary system. The width of these lines represent the outflow speeds of the ejecta. In some cases the absorption feature can show several components with different velocities, indicative of multiple distinct outflows (Jack et al., 2017; Aydi et al., 2019, 2020).

Later in the eruption, it often becomes clear that the Balmer emission lines show multiple peaks, an indicator that the emission originates from different components of the nova ejecta (possibly an equatorial torus and polar rings; Hutchings, 1972; Kolotilov, 1980). The idea of nova ejecta consisting of many components is supported by optical and near-infrared emission line modelling as discussed in §1.2.5. Often present in nova spectra are lines of C, N, O elements ejected together with the envelope during the eruption. As the nova evolves, the ejecta transition from optically thick to optically thin, as the emitting photosphere recedes towards the hot white dwarf. Consequently, many emission lines are observed due to ionization by the hot central object. At the final stage of the spectral evolution, the spectrum is entirely dominated by nebular emission lines (e.g., Warner, 2008).

1.2.3.3 X-ray emission from novae

Hard and soft X-rays present in novae result from shocked gas and nuclear burning, respectively. The nuclear burning phase (also known as the supersoft source phase [SSS] occurs when the residual H-rich envelope on the surface of the hot white dwarf burns steadily post eruptions (MacDonald et al., 1985). Soft X-rays are observed as the expanding envelope becomes optically thin allowing the X-ray emission to escape (Krautter et al., 1996; Orio, 1999). The timing of the soft X-rays turn on is crucial to estimating the mass and velocity of the ejected material (Krautter et al., 1996) while the timing of X-ray turn-off provides information on the mass of the compact object (MacDonald, 1996).

Hard X-ray emission originates from heated and shocked gas internal or external to the nova envelope

(e.g., Orio, 1999). The X-rays may arise as a radially-driven fast wind collides with the expanding ejected nova envelope (e.g., Mukai & Ishida, 2001). High absorbing columns are indicative of an emitting region that is embedded deep in the ejecta and therefore provide evidence of internal shocks. A low absorbing column is an indicator of an external emitting region and is observed in systems that contain dense pre-existing circumstellar material.

1.2.3.4 Gamma-rays in Novae

Novae were initially expected to produce γ-ray emission in the energy range of a few hundred keV to a thousand keV, considering the decay of isotopes produced during the TNR (e.g., Hernanz & José, 2004). However, γ-rays in novae were only detected in 2010, in the GeV energy range with the *Fermi Gamma Ray Space Telescope* (Abdo et al., 2010). To-date, novae that occur in systems with main sequence and evolved companion stars have both been detected to emit γ-rays (Abdo et al., 2010; Ackermann et al., 2014). An updated list of the most recent novae, including γ-ray novae, is presented by Koji Mukai[1].

In order to produce the observed energetic γ-rays, large amounts of relativistic particles need to be accelerated to high energies in shocked regions of the ejecta, unlike a decay of isotopes as hypothesised initially. The first nova to be detected in γ-rays was V407 Cyg, which is a symbiotic system constisting of a white dwarf and a Mira type giant companion star (Abdo et al., 2010). Due to the nature of the binary system, particles are accelerated to emit γ-rays as the nova ejecta collide with pre-existing surrounding dense material from the Mira type companion star (Abdo et al., 2010).

In addition, novae with main-sequence companion stars also emit γ-rays (e.g., Ackermann et al., 2014; Cheung et al., 2016). These novae have low density circumstellar material, and therefore energetic external shocks with the ejecta are unlikely. In this case, internal shocks between a slow equatorial flow and a fast polar wind provide an ideal environment for γ-ray emission (Chomiuk et al., 2014). This picture is supported by radio imaging of nova V959 Mon, the first classical nova to be detected as a γ-ray source (Chomiuk et al., 2014). Theoretically, it is possible for nova outflows to produce such high energy internal shocks (Metzger et al., 2014). γ-ray emission occurs as a result of either inverse-Compton scattering (leptonic model) or via pion decay (hadronic model) (Martin & Dubus, 2013). However, the hadronic model seems to better fit the observational features of novae (Martin et al., 2018).

[1] https://asd.gsfc.nasa.gov/Koji.Mukai/novae/novae.html

1.2.3.5 Dust formation

The most common ways to characterise dust formation in novae is through the formation of a dip in the optical light curve and/or excess emission at near-infrared wavelengths. The first evidence of dust in novae originated from infrared observations of FH Ser, where a dust minimum in the optical light curve coincided with excess emission in the infrared (Geisel et al., 1970). While some novae take days or months to emerge from the dust minimum, others such as V445 Pup take years (Woudt et al., 2009). It is not clear why this is the case, although the helium nova V445 Pup still remains a unique case. Dust grains form in relatively cooler regions (such as clumps) of the nova ejecta that are shielded from intense radiation of the white dwarf (Gehrz, 1988). Such regions can also be formed when a fast polar outflow and a slow equatorial outflow in novae interacts following a nova eruption to form a double shock structure (see figure 1 of Metzger et al., 2015). At the central shell, the gas cools and increases in density, providing an ideal environment to form dust (Derdzinski et al., 2017).

1.2.4 Nova classifications

The majority of Galactic classical novae consist of a main sequence star as the companion star and have accretion rates on the order of $\approx 10^{-10}$ to 10^{-9} $M_{\odot}$ yr^{-1} (Cassisi et al., 1998; José et al., 2006). Some time following the eruption, mass transfer resumes, and eventually the binary system will undergo another eruption. This is because during a nova eruption the binary system is not disrupted and in some cases the accretion disc is shown to survive the eruption (e.g., Worters et al., 2007; Mason et al., 2012). The time it takes for a nova to evolve from quiescence to another eruption depends on the mass and temperature of the white dwarf, and the accretion rate (Yaron et al., 2005). Since the mass of the white dwarf is inversely proportional to its radius, a massive white dwarf translates to a smaller size and deeper gravitational potential; it will therefore require a smaller amount of accreted material on its surface to trigger an eruption (e.g., Starrfield et al., 2016). The opposite is expected for a less massive white dwarf.

The accretion rate also plays a role between successive eruptions. At higher accretion rates, material will accumulate more rapidly, which results in shorter timescales for the material to reach a critical pressure for TNR. Consequently, the recurrence time for classical novae is predicted to be between a thousand to a million years, since most consist of white dwarfs with masses less than one solar mass (Truran & Livio, 1986). Recurrent novae are divided into three groups based on the observational properties and nature of the secondary star. The groups are named after their prototypes: RS Oph/T CrB, U Sco, and T

Pyx (Anupama et al., 2013). In the RS Oph/T CrB class, the white dwarfs accrete hydrogen rich matter from a red giant star, while those in the U Sco class accrete from sub-giants. The secondary stars in T Pyx-type systems are main sequence stars. The recurrence times for known recurrent novae are between one to hundred years (Schaefer, 2010; Darnley et al., 2014). The short recurrence time is attributed to high mass-accretion rates of $10^{-7} - 10^{-8}$ $M_{\odot}yr^{-1}$ and massive white dwarfs, $\gtrsim 1.3$ $M_{\odot}$ (Starrfield et al., 1985).

Similarly, a new classification of novae, based on the nature of the secondary star, has been proposed (Darnley et al., 2012). The classification combines both classical and recurrent novae such that all novae can be classified into either a main sequence class, a subgiant class or the red giant class. Binaries of the main sequence class have orbital periods in the range of hours (Diaz & Bruch, 1997; Schaefer, 2010). The subgiant class is characterized by orbital periods in the range of hours to days (e.g., Schaefer & Ringwald, 1995; Nogami et al., 2002). Objects in the red giant class have orbital periods greater than 100 days (Schaefer, 2010; Jurdana-Šepić et al., 2012).

Closely related to recurrent and classical novae are the helium novae. The accretion rates resulting in helium novae are $\approx 10^{-7}$ $M_{\odot}yr^{-1}$ (Nomoto, 1982; Livne, 1990; Piersanti et al., 2014). These rates could also drop to $\approx$ few $\times 10^{-8}$ $M_{\odot}yr^{-1}$ as shown in Figure 1.7 (Woosley & Kasen, 2011) depending on the mass of the white dwarf. The occurrence of a He-flash depends on whether a critical amount of material has accumulated on the surface of the white dwarf (e.g., Hillman et al., 2016). Only one helium nova is confirmed to date: V445 Pup (Lynch et al., 2004; Woudt & Steeghs, 2005).

1.2.5 Nova Remnants

Some nova shells become spatially resolved at optical, near-infrared and radio wavelengths days to years after an eruption depending on the distance to the nova and the resolving power of the telescope (Slavin et al., 1995; Gill & O'Brien, 1998, 2000; Woudt et al., 2009; Taylor et al., 1987; Linford et al., 2015). Resolving nova shells is crucial in determining their angular sizes. In combination with the time since eruption, the angular expansion rates can be determined.

Space and ground based telescopes with high resolution provide the resolving power to image individual Balmer lines (Hα and Hβ lines) and/or forbidden lines (e.g., [N II] and [O III]; Slavin et al., 1995; Sokoloski et al., 2017) of distinct parts of the nova shell. These images can be combined with the emission line profiles to reveal the three-dimensional ejecta geometry, where for example, all symmetric optically

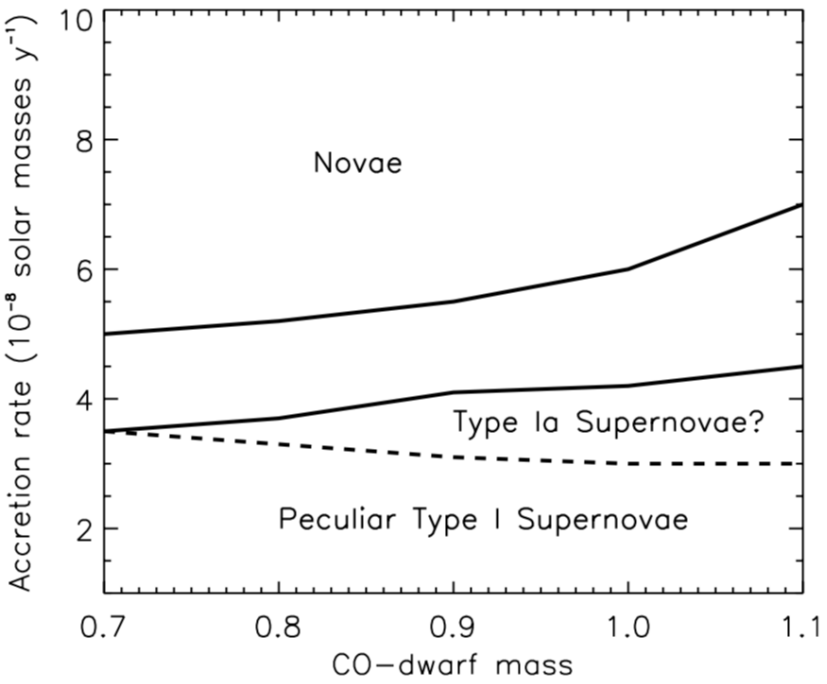

Figure 1.7: Illustration of different mass accretion rates of helium-rich matter to the surface of CO white dwarf and the respective outcomes: either helium novae or helium detonation. Diagram reproduced from Woosley & Kasen (2011).

thin gas geometries may lead to double-peaked lines (Hutchings, 1972). In addition to optical imaging, NIR imaging has also been used to resolve nova remnants (Woudt et al., 2009; Chesneau et al., 2012).

Consequently, it has been shown that nova ejecta are highly structured. Some of the noticeable structures include spherical outflows, bipolar outflows and equatorial rings accompanied by blobs of material (see Figure 1.8 reproduced from Sokoloski et al., 2017 and Figure 1.9 reproduced from Woudt et al., 2009). Shown in Figure 1.8 are *Hubble Space Telescope (HST)* images of nova V959 Mon, obtained through imaging of the Hα, [N II] and [O III] emission lines. V959 Mon was the first classical nova to be observed in γ-rays (Ackermann et al., 2014). Presented in Figure 1.9 are the images of the helium nova V445 Pup, obtained by imaging the entire nova envelope using adaptive optics on the Very Large Telescope (VLT) (Woudt et al., 2009). Both figures show bipolar outflows of the ejected material, and polar blobs aligned with the polar outflows are observed in V445 Pup. In addition to these outflows, other nova remnants appear in the form of clumps, ellipses and polar caps (Gill & O'Brien, 1998; Bode, 2004, 2010).

By utilising the angular expansion rates from imaging, the distance of the nova can be calculated

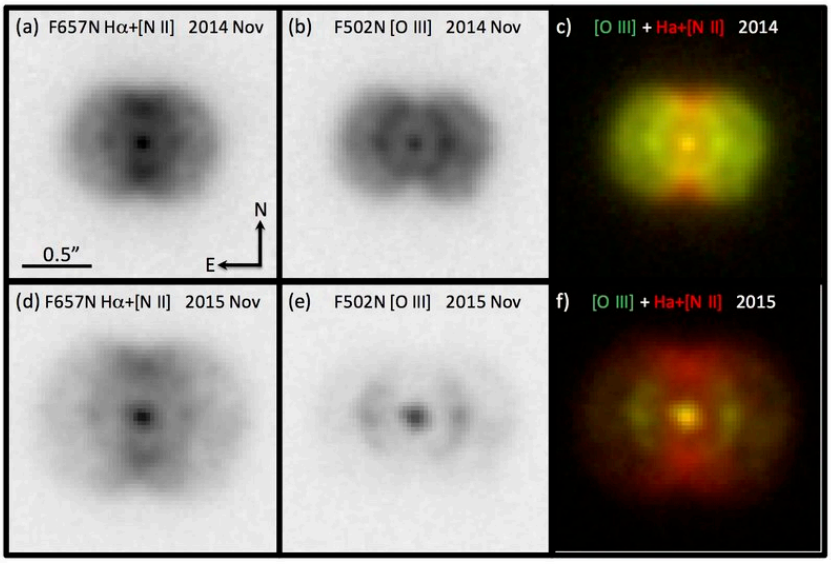

Figure 1.8: *HST* images of V959 Mon obtained by imaging [O III] and Hα+[N II] emission lines. The images were obtained more than two years after the nova eruption. Illustration reproduced from Sokoloski et al. (2017) with permission from the author.

by comparison with velocities measured from emission lines obtained via spectroscopy. This is called the expansion parallax method (Warner, 1995; Hellier, 2001). Using the expansion parallax to determine the distance to a nova is limited due to the following reasons: (i) insufficient early-time high-resolution observations to resolve the nova ejecta when optically thick, and (ii) lack of knowledge on the morphology of the ejecta, especially when the nova envelope is non-spherical (Wade et al., 2000). The true distance should thus depend on the three dimensional geometry and the inclination of the binary system (Wade et al., 2000). Distances determined with the parallax method should be treated with caution. Accurate distance determination is key to obtaining for example the ejected mass in novae. Attempts to obtain a three dimensional geometry of nova remnants have been made by combining imaging and spectral line modelling (Solf, 1983; Gill & O'Brien, 2000; Harman & O'Brien, 2003).

Where imaging is not possible, spectral line modelling can also provide information about the geometry of the nova (e.g., Hutchings, 1972; Solf, 1983). The spectra of permitted and forbidden lines show similar spatial and kinematic properties, and are thought to originate from different parts of the ejecta. This means the ejecta geometry could be similar in structure (Hutchings, 1972; Solf, 1983). Spectral line models are used to estimate the inclination of the system, the maximum expansion velocity of the envelope and

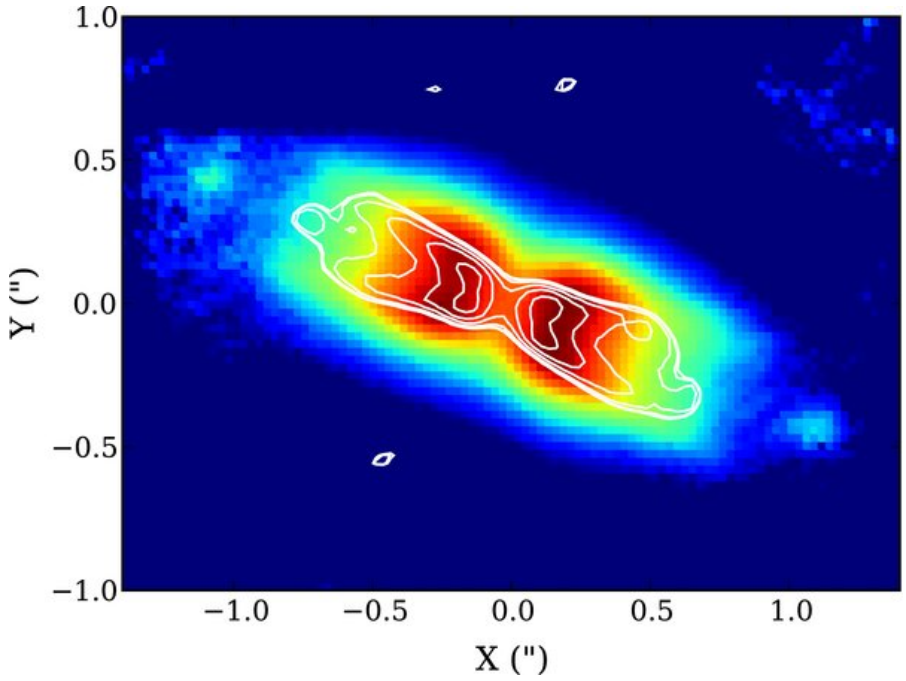

Figure 1.9: The spatially resolved expanding nova shell of the helium nova V445 Pup at near-infrared wavelengths. Reproduced from Woudt et al. (2009) with permission from the author. The contours represent near-infrared observations obtained on March 2005 and the colours are observations for March 2007, 4 – 6 years after the initial thermonuclear eruption. The images shows both equatorial and polar outflows together with polar blobs on the extreme ends of the polar outflows.

the morphology of the ejecta. Based on imaging and line modelling, it is clear that nova ejecta can be highly organized in structure. However, it is the bipolar ejecta morphology that has immediate implications for emission at high energies such as γ-rays and synchrotron emission, as discussed in §1.2.3.4 and §1.3.2.1.

1.2.6 Progenitors of type Ia supernovae

Supernovae of type Ia (SNe Ia) are destructive thermonuclear explosions that occur on a CO white dwarf (Whelan & Iben, 1973). In this case, the white dwarf is destroyed by a much more energetic explosion (compared to novae), and material is ejected at much faster velocities of $> 10^4$ km s^{-1} (e.g., Maoz et al., 2014). There are two channels which potentially lead to SNe Ia, the single-degenerate (SD) and the double-degenerate (DD).

In the SD channel, the white dwarf is expected to grow to the Chandrasekhar mass limit (~ 1.4 M$_\odot$), and eventually blows up as a thermonuclear explosion (e.g., Whelan & Iben, 1973). Mass can accumulate due to accretion of either hydrogen- or helium-rich material from a non-degenerate companion star (Warner, 1995; Kato et al., 1989). Some of the systems considered for this channel are the recurrent novae

since they host massive white dwarfs ($\gtrsim 1.2$ $M_\odot$), or classical novae that consist of massive white dwarfs. However, since these systems lose their outer envelopes after a nova eruption, it is not clear if the compact object can effectively grow in mass (MacDonald, 1984; Yaron et al., 2005). Evaluating accretion luminosity and consequently the accretion rates of mass onto the white dwarf and combining this rate with the time between successive eruptions, the accreted mass can be determined. The accreted mass can be compared to the estimated ejected mass following a nova eruption. However, the ejecta mass, accretion rates and recurrence times of novae have been shown to have large uncertainties (Yaron et al., 2005; Roy et al., 2012; Schaefer, 2010). However, recent studies by Starrfield et al. (2021) suggest that the white dwarf in novae may be able to retain mass via a layer of helium that grows over time following an eruption.

Further evidence that may constrain the SD channel arises from indications of circumstellar material in SN 2006X and PTF 11kx (Patat et al., 2007; Dilday et al., 2012). SN 2006X shows evidence of circumstellar material based on variable absorption features of Na I (Patat et al., 2007). The optical spectra of PTF 11kx show similar absorption lines (Dilday et al., 2012). The absorption lines likely result from regions of enhanced density (shells) in the circumstellar medium. Since pre-existing material could have originated from an accretion wind or previous nova eruptions, the progenitor in both cases is therefore most likely to be of SD origin.

Radio observations have been used to constrain the density distribution of material surrounding SNe Ia (Panagia et al., 2006). No known SN Ia explosion has been detected at radio frequencies. However, the upper limits on radio luminosity of observed SNe Ia systems have been used to rule out some progenitor systems. Some of the ruled out progenitors include symbiotics, due to their high mass-loss rates compared to the estimates from observed SNe Ia (Chomiuk et al., 2016; Pérez-Torres et al., 2014). Other ruled out progenitors are those that consists of white dwarfs undergoing stable nuclear burning, and blowing optically thick winds from the system, leading to insufficient mass retention required for the white dwarf to grow in mass (Chomiuk et al., 2012; Pérez-Torres et al., 2014). Some other progenitors such as recurrent novae with structured surrounding material are still considered as viable progenitors (Chomiuk et al., 2012; Pellegrino et al., 2020).

An alternative scenario considered for SNe Ia is helium detonation, where the white dwarf does not need to grow up to the Chandrasekhar mass limit (e.g., Moll & Woosley, 2013; Ruiter et al., 2014). After accumulation of a helium-rich layer from a helium star at particular mass accretion rates, as shown in Figure 1.7, a double detonation may occur on the white dwarf. Double detonation means both the CO core

and the helium layer are destroyed by an inward and outward shock wave (Nomoto, 1982).

Observational evidence for the double detonation scenario includes the discovery and study of the SN Ia SN 2016jhr (Jiang et al., 2017). Simulations show that the early flash observed in the optical light curves of SN 2016jhr is the result of accumulation of thin strips of helium-rich material that eventually led to a helium detonation (Jiang et al., 2017). Radio studies of potential progenitors are therefore important to study their environments and compare with observations of SNe Ia.

1.3 A radio view of novae

Astronomical radiation at radio wavelengths was discovered by Karl Jansky at a frequency of 2.1×10^7 Hz. He established that the radio emission originated from the centre of our Galaxy (Jansky, 1933). Radio emission from novae is observed weeks to months following an eruption and can last for years. These eruptions emit both thermal (free-free) emission and non-thermal (synchrotron) emission at radio wavelengths.

1.3.1 Emission processes

Tracing a ray of radiation with intensity I_ν to an observer on Earth is governed by the radiative transfer equation

$$\frac{dI_\nu}{ds} = -\kappa_\nu I_\nu + \epsilon_\nu \, . \tag{1.1}$$

where κ_ν and ϵ_ν are absorption and emission coefficients, respectively and ν is the frequency. The measure of the opacity of an emitting region with thickness s is quantified by the optical depth, τ_ν, which relates to the absorption coefficient as $d\tau_\nu = -\kappa_\nu \, ds$. If $\tau_\nu << 1$, the material is optically thin, and it is optically thick if $\tau_\nu >> 1$.

1.3.1.1 Free-free emission

Thermal bremsstrahlung, or free-free radiation, occurs when an electron is accelerated within a field of an ion. The emission coefficient is described numerically by Equation (6.16) of Kwok (2007) as

$$\epsilon_\nu = \frac{1}{4\pi} 6.8 \times 10^{-51} Z^2 n_e n_i T_e^{-0.5} \exp\left(\frac{-h\nu}{kT_e}\right) g_{ff}(\nu, T_e) \ \text{W m}^{-3} \ \text{Hz}^{-1}. \tag{1.2}$$

Here, n_e and n_i are the electron and ion number densities respectively. Z is the charge number, T_e is the electron temperature, h is the Planck constant and k is the Boltzmann constant. At radio frequencies below 10^{12} Hz, the Gaunt factor g_{ff}, is approximated by Equation (6.17) of Kwok (2007) as

$$g_{ff}(\nu, T_e) = 9.76 \; + \; 0.55 \ln\left(\frac{T_e^{1.5}}{\nu}\right). \tag{1.3}$$

In order to determine the specific intensity (Equation 1.1), the absorption coefficient κ_ν is first defined by relating it to the emission coefficient using the source function $S_\nu = \frac{\epsilon_\nu}{\kappa_\nu}$. This is only valid if $S_\nu = B_\nu$ where B_ν is the Planck function ($B_\nu = 2kT_e\nu^2/c^2$ at the long wavelengths considered here). The absorption coefficient is therefore defined as

$$\kappa_\nu = 1.79 \times 10^{-12} Z^2 n_e n_i T_e^{1.5} \nu^{-2} \exp\left(\frac{-h\nu}{kT_e}\right) g_{ff}(\nu, T_e) \;\; \mathrm{m}^{-1}. \tag{1.4}$$

The flux density observed to originate from a spherical source with radius r can therefore be estimated using the equation

$$F_\nu = B_\nu(T_e)\left(\frac{\pi r^2}{D^2}\right)(1 - \exp^{-\tau_\nu}) \tag{1.5}$$

(Seaquist & Bode, 2008). Here, D is the distance to the source. The optical depth at frequency ν of the thermally emitting gas can be estimated (Mezger & Henderson, 1967)

$$\tau_\nu \approx 8.235 \times 10^{-2} T_e^{-1.35} \nu^{-2.1} \int n_e^2 \, dl, \tag{1.6}$$

where ν is the observing frequency in GHz and $\int n_e^2 dl$ is the emission measure of radio emitting material in units of cm^{-6} pc.

The spectral energy distribution of radio emission can often be characterized as a simple power law, $F_\nu \propto \nu^\alpha$, where α is the spectral index. For material emitting free-free thermal radiation, $\alpha = 2$ for optically thick material (as expected for the long-wavelength behavior of the Planck function). Completely optically thin material will have $\alpha = -0.1$. In practice, α is calculated from observations as

$$\alpha = \frac{\log\left(\frac{F_{\nu_1}}{F_{\nu_2}}\right)}{\log\left(\frac{\nu_1}{\nu_2}\right)} \tag{1.7}$$

where F_{ν_1} and F_{ν_2} are the flux densities observed at two frequencies, ν_1 and ν_2, respectively.

Free-free emission in novae originates from ionized gas of the remnant expanding freely into a less dense circumstellar material. When the radio light curves of novae are modelled by assuming a certain geometry of the nova remnant, the kinetic energy of the eruptions and the mass of the ejected material

can be estimated. A spherical geometry of the ejecta has been widely used to describe radio emission from novae (Hjellming et al., 1979; Seaquist & Palimaka, 1977; Seaquist et al., 1980; Hjellming, 1996). More details on how radio emission from novae has been interpreted are given in §1.3.2.

1.3.2 Modelling of radio light curves

Radio emission from classical novae is known to persist for years and is described using the equations defined in §1.3.1.1 together with an assumed nova ejecta density profile. At the early stages of radio emission, the ejected material is optically thick, and the flux increases with time as the radio-emitting photosphere expands. The expected spectral index during the optically thick phase is $\alpha > 0$. As a result of the expansion, the nova envelope density drops and the radio photosphere (i.e., surface where $\tau_\nu \approx 1$) begins to recede towards the compact object. It takes more material to be optically thick at high frequencies (compared to lower frequencies), so the light curves will peak first at high frequencies and later at lower frequencies. Following the radio thermal peak is the final decline of the flux density. At this point, the emission is known to originate from optically thin material with $\alpha < 0$. The maximum flux density requires the ejecta to be physically large (Bode, 2002).

The standard Hubble flow model is widely used to describe radio light curves of novae. To describe the standard picture of radio observations of novae, I follow the presentation of Hjellming et al. (1979) and Seaquist & Palimaka (1977). The model predicts the evolution of a nova remnant emitting free-free emission using the following assumptions. First, the temperature of the shell is held constant at 10^4 K (e.g., Hjellming et al., 1979). Secondly, the ejected material is distributed in a finite sphere with an outer and inner radius as shown in Figure 1.10 such that

$$R_{\rm inner}(t) = V_{\rm inner}(t - t_0) + R_{\rm inner}, 0 \tag{1.8}$$

$$R_{\rm outer}(t) = V_{\rm outer}(t - t_0) + R_{\rm outer}, 0 \tag{1.9}$$

where $R_{\rm inner}, 0$ is the initial inner radius and $R_{\rm outer}, 0$ is the initial outer radius at time t_0, the time of the nova shell ejection. The shell with total mass $M_{\rm ej}$ is ejected instantaneously, but its components expand with a range of velocities such that $V \propto R$, framed by a minimum inner velocity ($V_{\rm inner}$) and a maximum outer velocity ($V_{\rm outer}$).

A density profile must also be assumed for the Hubble flow ejecta. A commonly used profile, consistent with many observations of novae, is to take $\rho \propto R^{-2}$. The resulting ejecta density is then given as

$$\rho(t, R) = \frac{M_{\rm ej}}{4\pi R^2}\left(\frac{1}{R_{\rm outer} - R_{\rm inner}}\right). \tag{1.10}$$

Models consisting of $1/R^3$ density profiles have also been considered when interpreting radio light curves of some novae (Seaquist et al., 1980). Utilising the above assumptions, the flux densities of novae depend on the distance to the nova, the temperature of the ejecta and the density profile of the ejected material.

The evolution of radio light curves of novae are presented in three phases. First, the flux rises, and its intensity is directly proportional to ν^2 and t^2 (Seaquist & Bode, 2008). At this point the nova remnant is emitting optically thick thermal emission, and the radio photosphere coincides with the boundary of the outer shell as it expands (see an illustration in Figure 1.10).

During the second phase, the radio photosphere begins to recede towards the compact object and thus lags behind the outer shell boundary. During this time, the light curve peaks and the flux density is directly proportional to $\nu^{0.6}$ and $t^{1.3}$, as the remnant turns over from emitting optically thick emission to optically thin emission (Seaquist & Bode, 2008). The third phase of the evolution is when the emitted flux is proportional to $\nu^{-0.1}t^{-3}$ as it decreases with time. The radio emission lasts for years after initial detection. The standard model has been successful in replicating some radio light curves of novae over a wide range of frequencies (see Figure 1.11, Hjellming et al., 1979). However, well sampled radio light curves and imaging at high resolution have revealed events such as delayed mass ejections and clumping which have challenged the simplistic approach, described above, of modelling nova radio light curves (Nelson et al., 2014; Wendeln et al., 2017).

1.3.2.1 Synchrotron emission

Synchrotron emission, also known as magneto-bremsstrahlung, is the result of relativistic electrons accelerated in a magnetic field. The continuum emission is characterised by $\alpha = 2.5$ for material made optically thick by synchrotron self absoprtion, and $\alpha = -(p-1)/2$ for optically thin material. Here p is the power-law index of the electrons' enegy spectrum (Lang, 1980). The emission and absorption coefficients of Equation 1.1 for synchrotron emission are given by Irwin (2007) as

$$\begin{aligned} \epsilon_\nu &= C_5 N_0 B^{\frac{p+1}{2}} \left(\frac{\nu}{2C_1}\right)^{\frac{1-p}{2}} \\ \kappa_\nu &= C_6 N_0 B^{\frac{p+2}{2}} \left(\frac{\nu}{2C_1}\right)^{\frac{-(p+4)}{2}}. \end{aligned} \tag{1.11}$$

C_1, C_5 and C_6 are normally known as the Pacholczyk's constants. B is the magnetic field strength in the synchrotron-emitting region. The emission and absorption coefficients are combined using the source

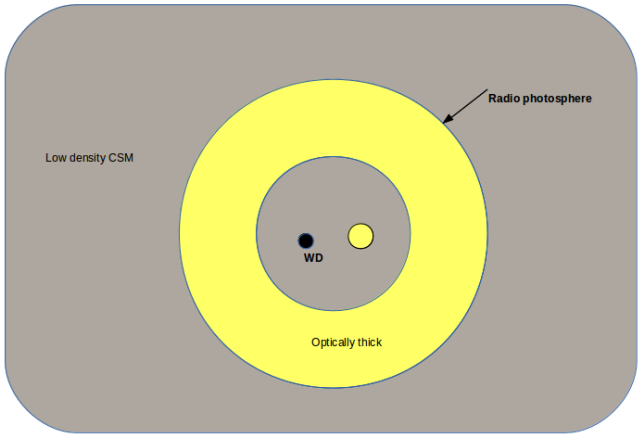

Figure 1.10: A spherically symmetric expanding nova envelope. The yellow annulus surrounding the binary system represents the radio-emitting region. The emission observed is from a freely expanding envelope with no shock interactions.

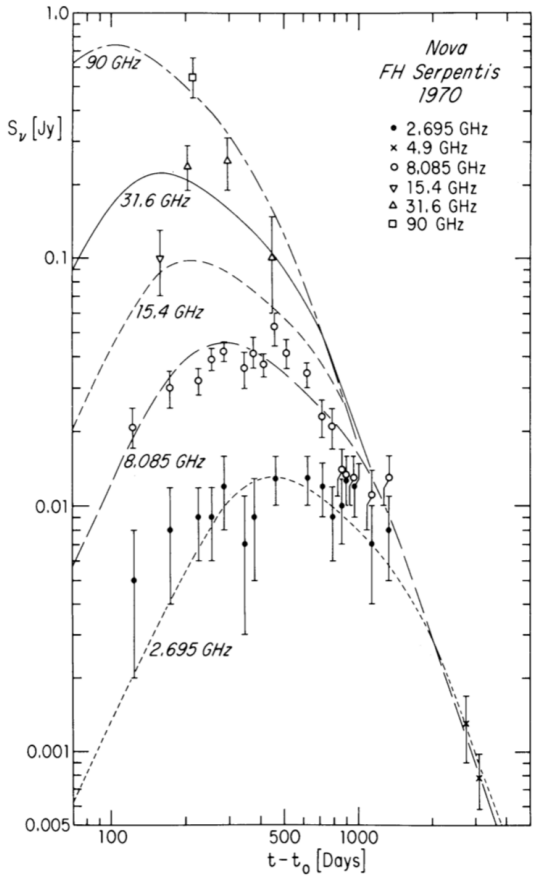

Figure 1.11: Radio light curves of FH Ser replicated using the standard radio frequency model of a freely expanding nova shell with no shock interactions as that shown in Figure 1.10 (Hjellming et al., 1979).

function $S_\nu = \frac{\epsilon_\nu}{\kappa_\nu}$ to give the specific intensity

$$I_\nu = S(\nu_1) J(\frac{\nu}{\nu_1}, p) \tag{1.12}$$

where ν_1 is the frequency when optical depth is equal to unity defined as

$$\nu_1 = 2C_1 (l C_6 N_0)^{\frac{2}{p+4}} B^{\frac{p+2}{p+4}} \tag{1.13}$$

Here, l is associated with the volume of the emitting region. The J function in Equation 1.12 is

$$J(\frac{\nu}{\nu_1}, p) = \Big(\frac{\nu}{\nu_1}\Big)^{\frac{5}{2}} \Big[1 - \exp\Big(\Big(-\frac{\nu}{\nu_1}\Big)^{\frac{P+4}{2}}\Big)\Big].$$

With the above definitions, the observed flux density is therefore given as

$$F_\nu = \Omega I_\nu$$

where $\Omega = \frac{\pi R^2}{D^2}$ is the solid angle of the emitting source. The flux densities in the optically thick and thin limits can be calculated as

$$\begin{aligned} F_{\text{thick}}(\nu) &= \frac{\pi R^2}{D^2} \frac{C_5}{C_6} B^{-0.5} \Big(\frac{\nu}{2C_1}\Big)^{2.5} \\ F_{\text{thin}}(\nu) &= \frac{4\pi R^3}{3D^2} C_5 N_0 B^{\frac{P+1}{2}} \Big(\frac{\nu}{2C_1}\Big)^{\frac{1-P}{2}} \end{aligned} \tag{1.14}$$

Here N_0 is defined in Equation 10 of Chevalier (1998). Synchrotron emission is common in thermonuclear eruptions and stellar explosions. Detection of synchrotron radiation from novae usually precedes thermal emission. Synchrotron emission in novae with a less evolved companion has been observed previously. However, the detection of gamma-rays with the Fermi-LAT telescope in 2010 (Ackermann et al., 2014) has ignited more research in shocks during nova eruptions. Synchrotron emission can help us determine shock velocities and the total energy of the eruption while probing the circumstellar surrounding medium.

The first nova discovered to emit synchrotron emission was RS Oph (Hjellming et al., 1986; Taylor et al., 1989). RS Oph is a recurrent symbiotic nova that has had several recorded nova eruptions. Radio observations from two eruptions show the presence of non-thermal emission with high brightness temperatures ($> 10^4$ K), flux densities that peak in less than a year (see Figure 1.12), and spectral indices $\alpha < -0.1$ (Hjellming et al., 1986; Sokoloski et al., 2008; Rupen et al., 2008; Eyres et al., 2009; Kantharia et al., 2016). The environment around the nova is dense due to the presence of a wind from the companion red giant star. The nova envelope in a system such as RS Oph interacts with the circumstellar medium, producing high energy external shocks (O'Brien et al., 2006) as shown in Figure 1.13. In the shocked regions, relativistic

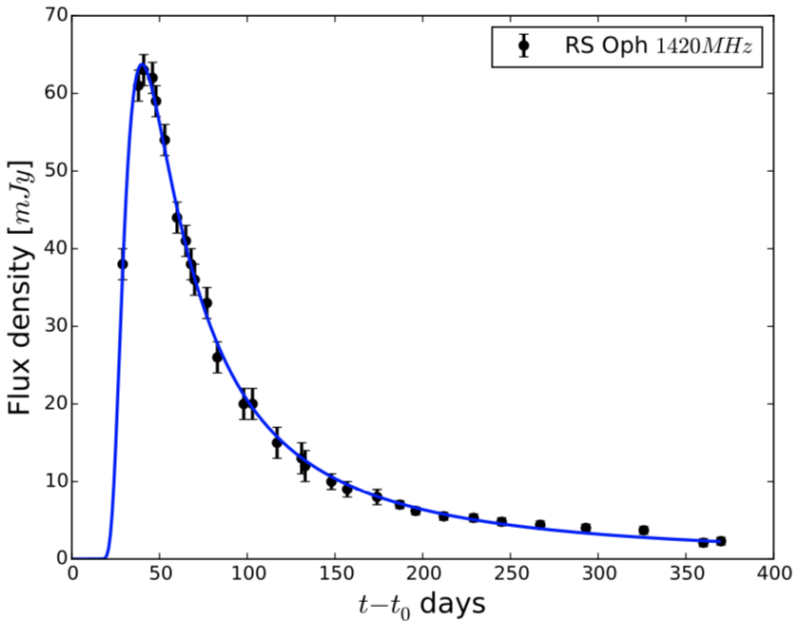

Figure 1.12: Radio light curve of recurrent nova RS Oph obtained at 1.4 GHz, reproduced from Kantharia et al. (2016). Following a thermonuclear eruption at day 0, the flux increases because of increase in absorption and decreases as the expanding shell expands with time (the solid line).

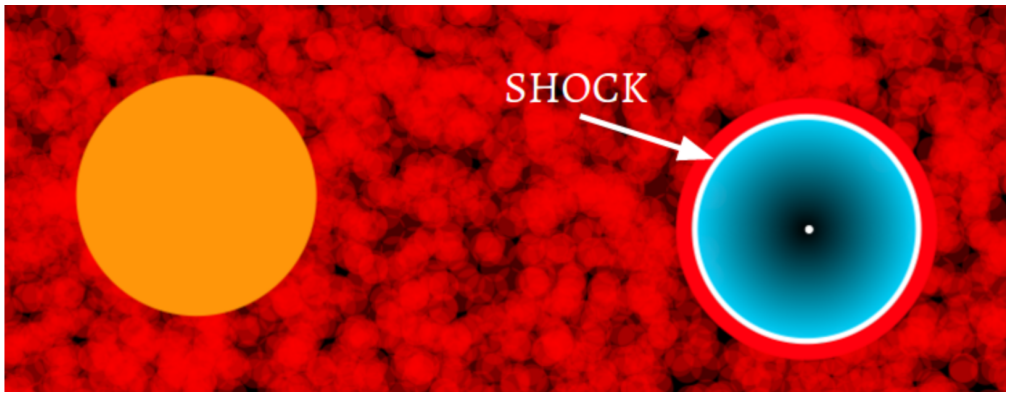

Figure 1.13: A representation of shocks external to the nova ejecta, as it interacts with a dense wind from a giant companion star, reproduced from Finzell (2017). These shocks have been shown to be the source of non-thermal emission in recurrent symbiotic novae such as RS Oph and V745 Sco.

electrons are accelerated and gyrate along amplified magnetic fields producing non-thermal emission (Reynolds, 2017).

Non-thermal emission is also present in classical novae. The first interesting case of this class of novae emitting non-thermal emission is QU Vul (Taylor et al., 1987). The radio observations revealed

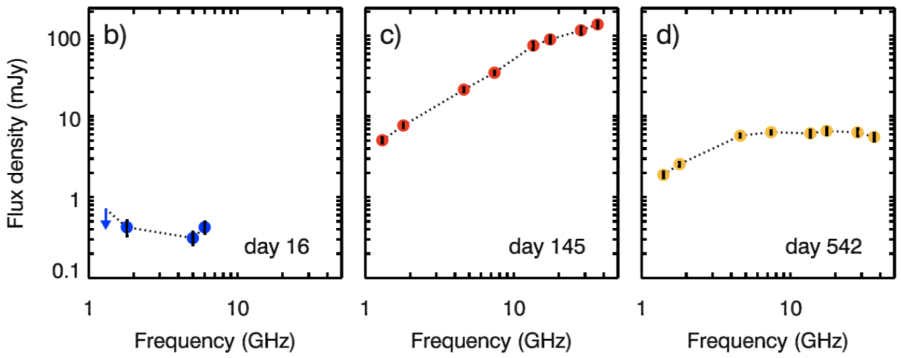

Figure 1.14: Spectra of nova V959 Mon days to years after an eruption showing at least two types of radio emission, synchrotron emission during the early times (day 16) and free-free emission at late times (day 145 and 542) of its evolution. Reproduced from Chomiuk et al. (2014) with permission from author.

a bright radio peak characterised by a spectral index of $\alpha = 2.4$ and brightness temperature of 10^5 K, ~200 days following the eruption. These were attributed to presence of either synchrotron emission or shocked thermal gas (Taylor et al., 1987). The presence of a main sequence companion implies low-density circumbinary material, and therefore an interaction similar to that of RS Oph is unlikely. The source of synchrotron emission is therefore likely a wind interacting with the inner part of a nova shell ejected during the initial thermonuclear eruption to produce shocks within the ejecta (Taylor et al., 1987). Following the radio peak, the light curves evolved consistent with an expanding thermal remnant (Taylor et al., 1987).

V959 Mon is another example showing the presence of non-thermal radio emission. The spectral index of $\alpha = -0.1$ was determined on day 16 after eruptions as shown in Figure 1.14. This is inconsistent with the canonical $\alpha = 2$, which is known to originate from an optically thick ionized medium, resulting in the conclusion that the emission is non-thermal in nature (Chomiuk et al., 2014). The emission was preceded by the detection of γ-rays from the nova (Ackermann et al., 2014). Both the radio and γ-ray radiation are used to trace relativistic particles accelerated to high energies.

High resolution radio imaging was utilised to determine the origin of non-thermal emission in V959 Mon. Initially on day 91 after eruptions, the European Very Long Baseline Interferometry Network (EVN) traced the compact knots of the nova (Chomiuk et al., 2014). The VLA resolved images on day 87 revealed an expanding component. Based on the observed flux densities, it was established that the synchrotron emission originated from the compact components while the source of the free-free emission was the bulk material (Chomiuk et al., 2014). The presence of non-thermal emission suggests an interaction between

fast and slow moving outflows.

Internal shocks in novae may result from any form of collisions of discrete mass outflows or material travelling at different velocities. At the start of an eruption, the nova envelope is lifted as degeneracy is quenched on the surface of the white dwarf. The binary system will immediately transfer momentum and energy to the ejecta, thus the material concentrates in the orbital plane of the binary, as shown as the vertical yellow region of Figure 1.15 (Chomiuk et al., 2014). Later in the evolution, an optically thick wind develops due to radiation pressure on the surface of the white dwarf, which flows in the polar directions of the binary system, presented as the blue regions of Figure 1.15. The shocked regions thus occur due to shocks as the two outflows collide, forming sites of electron acceleration to energies that give rise to $\gamma-$rays and synchrotron emission. The wind dominates the radio emission at early times and the more dense material dominates at later times.

V1723 Aql also shows an unusual radio light curve similar to that of QU Vul as shown in Figure 1.16 (Roy et al., 2012; Weston et al., 2014). The radio light curve consists of an initial radio peak ~40 days after the eruption (see also Krauss et al., 2011), where the flux increase is proportional to $t^{3.3}$, steeper than that predicted for the Hubble flow model (shown as dotted lines in Figure 1.16; the standard radio light curve predicts $F_\nu \propto t^2$). In addition, the brightness temperature of the ejecta was determined to be 10^5 K during the initial radio bump, which is too high to be easily explained as free-free emission (Weston et al., 2016a).

In V1324 Sco, a spectral index of $\alpha = -0.1$ is observed on day 25, followed by a very rapid increase in flux with brightness temperatures 10^5 K (Finzell et al., 2018). The synchrotron emission was preceded by a detection of $\gamma-$rays (see figure 3 of Finzell et al., 2018). V1324 Sco is a nova which shows a negative spectral index and an initial radio bump. However, later in the radio evolution, at ≈ 200 days after eruption, the emission is consistent with the standard model of an expanding thermal remnant.

Generally, signatures of non-thermal emission in novae include negative spectral indices early on after an eruption and a rapid rise in flux densities with time, contrary to the predicted rise of a freely expanding nova envelope. Other features include high brightness temperatures on the order of $\gtrsim 10^5$ K and in some cases excess emission at lower frequencies (Taylor et al., 1987; Chomiuk et al., 2014; Weston et al., 2016a; Finzell et al., 2018). Since most of the radio emission is internal to the ejecta, the inclination angle of the binary system could determine whether synchrotron emission is detected as it is possible to be obscured by the thermal gas if the orbital plane of the nova is viewed pole on (e.g., Weston et al., 2016b).

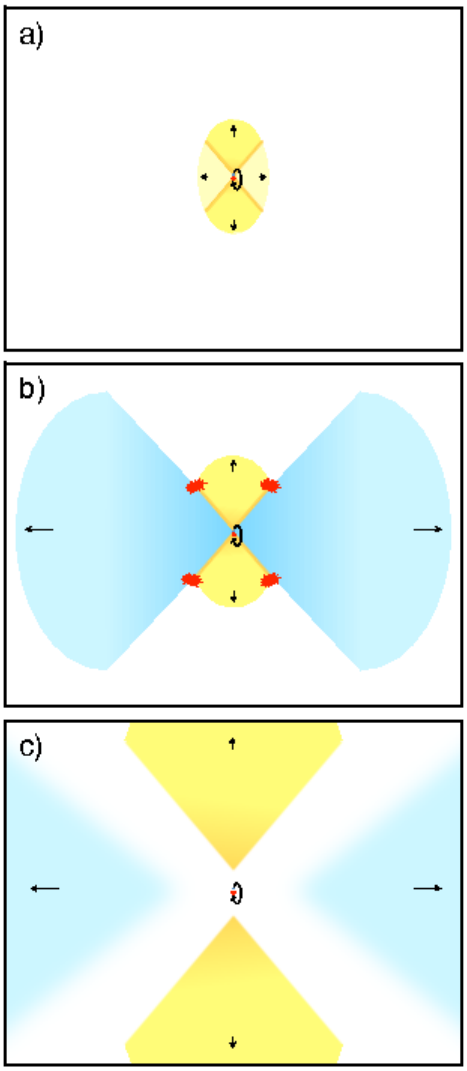

Figure 1.15: A visual representation to explain the ejecta evolution of V959 Mon. Illustration reproduced from Chomiuk et al. (2014) with permission from author. (a) Soon after the eruption, during the common envelope phase, the material will surround the binary system. As the binary interacts with the ejecta, the dense material is aligned with the equatorial plane. (b) The less dense wind (blue) from the white dwarf escapes through the polar directions. When the two distinct flows collide they form internal shocks shown in red markings. (c) As the wind expands, its density drops and the ejecta become diffuse. Radio imaging at this point of the evolution will detect the dense material concentrated at the equatorial plane.

1.3.2.2 High resolution imaging of the nova ejecta

Long baseline ($\gtrsim$ several kilometers) radio interferometers provide high resolving power, and therefore are able to resolve images of nova ejecta, revealing finer details of nova ejecta structure. The first nova to be spatially resolved at radio wavelengths was QU Vul. The radio images revealed a spherical symmetry of the nova ejecta (Taylor et al., 1987). However, resolved MERLIN images of V1974 Cyg and V723 Cas are

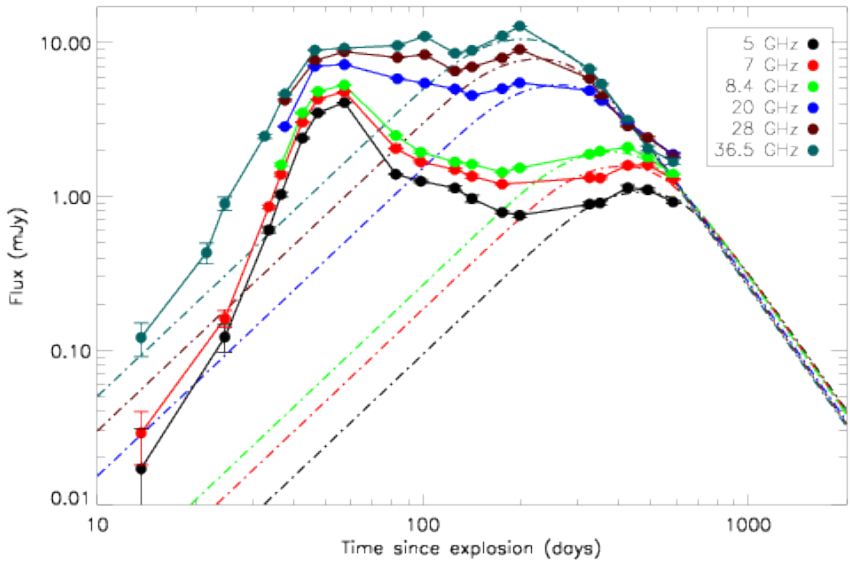

Figure 1.16: Radio light curves of V1723 Aql. The dashed and dotted lines are Hubble-flow model light curves at different radio frequencies, reproduced from Roy et al. (2012) with permission from the author.

asymmetric (Eyres et al., 1996; Hjellming, 1996; Heywood et al., 2005).

Recently, resolved VLA images of V959 Mon, Linford et al. (2015), show two bright components in the east-west direction embedded in a diffuse envelope. Similar components are observed in resolved images of V1723 Aql, days after eruption (Weston et al., 2016a). Estimating the mass of the ejected envelope and their velocities from radio observations by assuming spherical geometries is therefore a too simplistic approach.

1.3.3 Estimations of ejected mass during nova eruptions

One of the key reasons radio observations of novae are frequently sought after is because of the direct link to estimating the ejected mass following a nova eruption. However, the masses of the nova envelopes predicted using models of nova eruptions do not match with those inferred from radio light curves (Yaron et al., 2005; Seaquist & Bode, 2008; Roy et al., 2012). Observed novae presented in Seaquist & Bode (2008) have ejected masses in the range of 10^{-4} to 10^{-5} $M_{\odot}$, based on the standard radio models. The same sample is expected to expel masses only in the range of 10^{-6} to 10^{-7} $M_{\odot}$ based on theoretical predictions, which explore the relationship between the properties of the white dwarf and the observed characteristics as illustrated in Figure 1.17 (Roy et al., 2012; Wendeln et al., 2017).

Efforts have been made to understand this discrepancy. Some of the reasons identified include clumps in the ejected material (Moraes & Diaz, 2011). Consider the case of V351 Pup. Previously, the mass of the nova was determined as 10^{-3} $M_{\odot}$ using the Hubble flow model by maintaining that the density of material in the ejecta is uniformly distributed, thus assuming a filling factor $f = 1$ (the filling factor indicates the fraction of the volume that is filled by gas) (Seaquist & Bode, 2008). Later, Wendeln et al. (2017) used the same family of light curve models, but considered a filling factor of $f \sim 10^{-2}$ to replicate the effect of clumping in the ejecta—and therefore estimated a mass of 10^{-6} $M_{\odot}$.

The most recent approximation is three orders of magnitude less than what was determined before and consistent with theoretical predictions. In general, filling factors for novae are estimated to range from 10^{-5} to 10^{-1} using optical spectroscopy and imaging at optical or radio wavelengths (e.g., Andrea et al., 1994; Mason et al., 2005; Shara et al., 2012; Diaz et al., 2018). Low filling factors (values less than 1) derived from photoionization calculations imply neutral gas present in clumps of nova ejecta (e.g., Andrea et al., 1994). Clumping or non-uniformity in nova ejecta increases the radio emission and prolongs the radio evolution phases. Therefore, assuming a uniform filling factor will therefore overestimate the ejected mass if the ejecta are clumpy (Wendeln et al., 2017).

The morphology of the shell, such as a bipolar morphology also changes the estimated masses derived from radio light curves (e.g., Seaquist & Palimaka, 1977; Ribeiro et al., 2014). The assumption of a spherical nova remnant in radio models for a system with bipolar outflows results in over estimating the ejected mass by a factor of two. Exploring alternative models when estimating mass loss in nova eruptions is therefore necessary.

1.4 Overview of thesis

The purpose of this work is to study radio observations of thermonuclear eruptions including the helium nova V445 Puppis, the classical nova V339 Delphini, and the recurrent symbiotic nova V3890 Sagittarii, with the aim of understanding mechanisms that drive mass losses and shocks following an eruption. The targets have been extensively monitored at radio frequencies, resulting in well sampled radio light curves. In this thesis, we investigate the complexity of nova ejecta and the environments surrounding them and how this affects the predictions of ejected mass from standard radio models.

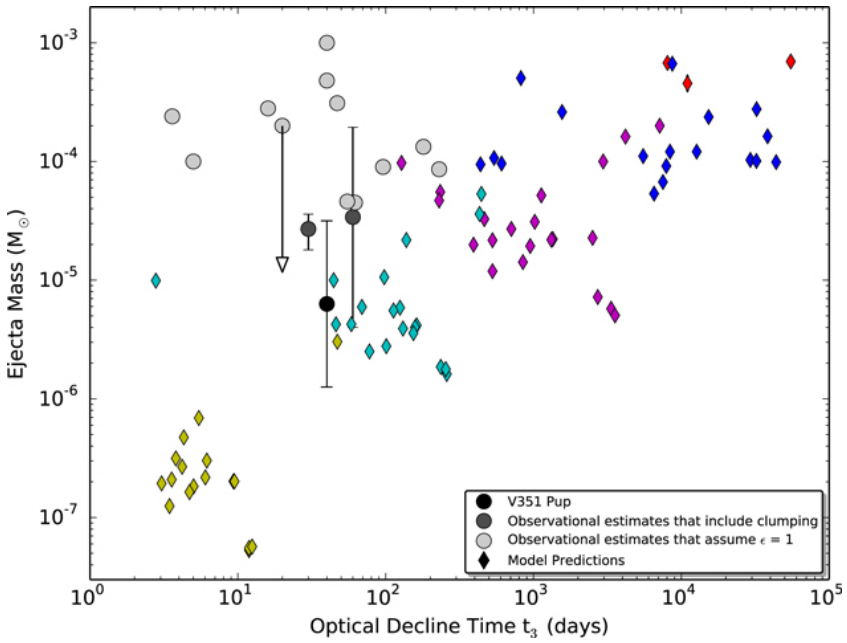

Figure 1.17: Illustration of nova ejecta mass against time taken for the optical light to dim by three magnitude, reproduced from Roy et al. (2012); Wendeln et al. (2017) with permission from the author. The diamonds represent predicted theoretical nova ejecta masses for eruptions on different white dwarf masses (Yaron et al., 2005). The grey circles show the estimated masses from radio light curves assuming a filling factor $f \sim 1$ given in Seaquist & Bode (2008) and Weston et al. (2016a). The black circles show estimated novae ejecta mass based on radio light curves, including a clumpiness factor (Nelson et al., 2014; Wendeln et al., 2017; Finzell et al., 2018).

In Chapter 2, the Very Large Array observations of V445 Pup obtained between years 2001 and 2008 are presented. This has resulted in one of the most detailed sets of radio light curves of a nova. The radio observations are used to establish whether the type of radio emission that dominates in classical novae is also present in the only spectroscopically confirmed helium nova to date.

In Chapter 3, MeerKAT observations of the recurrent nova V3890 Sgr are presented. This recurrent symbiotic nova went into its third recorded eruption on 2019 August 27. These systems are considered as viable SNe Ia candidates. Radio observations are utilised to estimate the mass loss rates from the secondary star and to probe the density profile of the surrounding medium.

In Chapter 4 of the thesis, I present multifrequency observations of the classical nova V339 Del. The nova eruption occurred in 2013 August (Waagen et al., 2013). Later, on day 4 after the optical rise, the nova was detected in $\gamma-$rays at energies greater than 100 MeV (Hays et al., 2013; Ackermann et al., 2014).

I use multi-frequency radio light curves and non-spherical models to estimate the mass ejected in V339 Del following the 2013 eruption.

Finally in Chapter 5 I present my conclusions and suggestions for future work.

CHAPTER 2

RADIO LIGHT CURVES AND IMAGING OF THE HELIUM NOVA V445 PUPPIS REVEAL SEVEN YEARS OF SYNCHROTRON EMISSION

M M Nyamai, L Chomiuk, V A R M Ribeiro, P A Woudt, J Strader, K V Sokolovsky, 2021, *MNRAS, 501, 1394*

Abstract

V445 Puppis is the only helium nova observed to date; its eruption in late 2000 showed high velocities up to 8500 km s^{-1}, and a remarkable bipolar morphology cinched by an equatorial dust disc. Here we present multi-frequency radio observations of V445 Pup obtained with the Very Large Array (VLA) spanning 1.5 – 43.3 GHz, and between 2001 January and 2008 March (~ 89 – 2700 days after eruption). The radio light curve is dominated by synchrotron emission over these seven years, and shows four distinct radio flares. Resolved radio images obtained in the VLA's A configuration show that the synchrotron emission hugs the equatorial disc, and comparisons to near-IR images of the nova clearly demonstrate that it is the densest ejecta—not the fastest ejecta—that are the sites of the synchrotron emission in V445 Pup. The data are consistent with a model where the synchrotron emission is produced by a wind from the white dwarf impacting the dense equatorial disc, resulting in shocks and particle acceleration. The individual synchrotron flares may be associated with density enhancements in the equatorial disc and/or velocity variations in the wind from the white dwarf. This overall scenario is similar to a common picture of shock production in hydrogen-rich classical novae, but V445 Pup is remarkable in that these shocks persist for almost a decade, much longer than the weeks or months for which shocks are typically observed in classical novae.

2.1 Introduction

Extensive accretion of helium-rich material onto a white dwarf (WD) from a helium companion star results in increasing density and temperature on the WD surface, eventually triggering a helium shell flash (known as a helium nova; Kato et al., 1989). Helium novae occur for mass accretion rates in the range $\sim 10^{-8}$ to 10^{-7} $M_\odot$ yr^{-1} (Woosley & Kasen, 2011; Piersanti et al., 2013). The thermonuclear runaway ejects the outer accreted layers analogous to hydrogen-rich classical novae (see e.g., Bode & Evans, 2008; Woudt & Ribeiro, 2014), although more mass is ejected in helium novae (Kato et al., 1989; Hillman et al., 2016). However, when the helium accretion rate is lower ($\leq 10^{-8}$ $M_\odot$ yr^{-1}), it is possible for a helium ignition on the surface of the WD to trigger an inward shockwave which leads to an explosion at the core of the WD hence a double detonation (Nomoto, 1982; Shen & Bildsten, 2009). If the detonation occurs on a carbon-oxygen WD, it could produce a Type Ia supernova (SN Ia; Moll & Woosley, 2013; Ruiter et al., 2014; Piersanti et al., 2014). The study of helium accretion is therefore important for validating or ruling out helium-donor and WD binary systems as progenitors of SNe Ia.

In this paper (chapter), we present radio observations of the only spectroscopically confirmed helium nova, V445 Puppis. The nova was discovered in eruption in late 2000 November at an optical maximum of $V \approx 8.6$ mag (Kato et al., 2000), substantially brighter than its $V \approx 14.5$ pre-eruption magnitude (Ashok & Banerjee, 2003). The day of eruption for V445 Pup is unknown and only constrained to be between 2000 September 26 and 2000 November 28 (Ashok & Banerjee, 2001; Kato et al., 2000; Woudt et al., 2009). We adopt a t_0 from Woudt et al. (2009) of 2000 November 02 (MJD = 51850) as the time of eruption. The nova was unusually rich in carbon and showed helium emission lines, but lacked hydrogen lines (which are prominent in the spectra of classical novae; Ashok & Banerjee, 2003; Iijima & Nakanishi, 2008; Woudt et al., 2009).

Within one month of the eruption, dust was detected from the nova using infrared spectroscopy (Lynch et al., 2004). By ~ 8 months after the nova eruption, the optical brightness had dropped below pre-eruption levels (Ashok & Banerjee, 2003; Woudt et al., 2009), attributed to a strong dust formation episode. Six years following the eruption, the optical light had still not returned to pre-eruption levels (Woudt et al., 2009), and the dust mass was determined to be $> 10^{-5}$ $M_\odot$ (Shimamoto et al., 2017).

V445 Pup was spatially resolved using near-infrared adaptive optics imaging with the Very Large Telescope (VLT), revealing an expanding bipolar shell confined by an equatorial dust disc and with polar

knots on both ends of the bipolar ejecta (Woudt et al., 2009; see their Figure 2). Woudt et al. (2009) determined a distance of 8.2 $\pm$ 0.5 kpc to the nova using expansion parallax techniques.

Presented in this paper (chapter) are multifrequency observations of the nova obtained in the years following eruption using the Very Large Array (VLA) radio telescope. The radio data reveal an unprecedented, near decade-long, synchrotron-powered radio light curve. In §2, we discuss the radio observations and our data analysis procedure. In §3, we present the multi-frequency radio light curve, radio spectral evolution, and spatially-resolved radio imaging. In §4, we present the results, and in §5 we highlight our conclusions.

2.2 Observations and data analysis

Radio observations of V445 Pup were obtained with a variety of VLA programs, most of which were led by M. Rupen. The data were retrieved from the VLA archive (see Table 2.1 for a log of the observations).

The first radio observations of V445 Pup were taken on 2001 January 18 and 30 ($t - t_0$ = 77 and 89 days). On day 77, the nova was not detected at 8.4 GHz (Rupen et al., 2001), and there was a marginal detection on day 89. After day 89, observations were paused until 2001 September 9 (day 312), when the nova was strongly detected at 8.4 GHz (Rupen et al., 2001). V445 Pup was subsequently observed with the VLA from September 2001 to March 2008 (between day 312 – 2704), resulting in a detailed radio light curve spanning almost a decade following the eruption (Figure 2.1).

Observations were obtained in continuum mode, at different frequency bands with two 50 MHz-wide frequency channels. The observations were conducted at L (1.46 GHz), C (4.86 GHz), X (8.46 GHz), U (14.94 GHz), K (22.46 GHz) and Q (43.34 GHz) bands, and are used to trace the nova emission throughout all of the VLA's configurations. The VLA A configuration provides the highest resolution (synthesized beam Full Width at Half Maximum (FWHM) of $2''$ at 1.5 GHz and $0.3''$ at 8.5 GHz), and has the potential to provide resolved images (see § 2.3.3). At each frequency, observations of the target are obtained together with observations of gain calibrators (see Table 2.2). The most common gain calibrator used was 0804 – 278, for which we took the ICRS coordinates RA = 08h04m51.451s and Dec = $-27^\circ 49' 11.32''$. We note that a slightly different RA position was used by National Radio Astronomy Observatory (NRAO) for this calibrator in 2001 – 2002 (RA = 08h04m51.440s); we, therefore, shifted the data so that all observations take RA = 08h04m51.451s (this is particularly relevant for our imaging results; §2.3.3). Flux density

Table 2.1: Log of VLA observations of V445 Pup.

Observation	t	$t-t_0$	Configuration	Observation time on target (min)					
Date	(MJD)	(Days)		1.43 GHz	4.86 GHz	8.46 GHz	14.94 GHz	22.46 GHz	43.34 GHz
2001 Jan 18	51927	77	A	...	...	3.7	...	...	...
2001 Jan 30	51939	89	A	...	...	6.4	...	...	...
2001 Sept 09	52162	312	C	...	...	6.7	...	...	...
2001 Sept 11	52164	314	C	15.6	3.7	...	5.2	4.6	4.4
2001 Sept 12	52165	315	C	10.9	3.9	3.7	5.2	4.4	...
2001 Sept 14	52167	317	C	...	4.1	...	...	...	...
2001 Sept 15	52168	318	C&D	...	1.9	3.1	...	...	...
2001 Sept 16	52169	319	C&D	5.2	6.9	6.9	4.9	...	...
2001 Sept 17	52170	320	C&D	10.4	11.2	...	11.9	...	...
2001 Sept 20	52173	323	C&D	3.7	4.2	4.2	4.2	4.2	...
2001 Sept 25	52178	328	C&D	...	11.7	12.7	14.8	...	...
2001 Sept 26	52179	329	C&D	...	3.2	4.7	6.2	6.2	...

'...' indicates no observations for this epoch at that frequency. Here, t_0 is taken as 2000 November 02 (MJD = 51850).
This table is continued in Appendix A Table A.1.

calibrators 0137+331 (3C48), 0542+498 (3C147) or 1331+305 (3C286) were observed to set the absolute flux density scale. Some observations were obtained without a flux density calibrator; in most cases, we do not include these observations in this work. For the ones included, we used a flux calibrator of an adjacent epoch to set the flux density of the secondary calibrator.

All data were processed using the Common Astronomy Software Applications (CASA; McMullin et al., 2007). The `AOflagger` algorithm (Offringa et al., 2012) was used to flag data corrupted by radio frequency interference. Standard calibration procedures were applied to each observation, and calibration solutions were applied to the target data before imaging. Starting in 2006, the VLA antennas were gradually upgraded to Jansky VLA capabilities, and we therefore found baseline-based calibration solutions using the flux calibrator. The CASA task `clean` was used for imaging, utilising Briggs weighting with a robust value of 1. Self-calibration was not performed.

To measure the flux densities of V445 Pup, the CASA task `imfit` was used to fit a Gaussian to the nova in each resulting image. In most measurements the width of the Gaussian is allowed to vary, and the integrated flux density was recorded. However, in cases of low signal-to-noise, the size of the Gaussian was fixed to the size of the synthesized beam. The uncertainty in flux density includes the error from the Gaussian fit added in quadrature with estimates of the uncertainty on the absolute flux calibration (5% of the flux for 1 – 10 GHz and 10% of the flux for frequencies greater than 10 GHz). In epochs where there is a non-detection, the task `imstat` was used to determine the noise of the image. An upper limit on the flux density is determined as three times the image rms plus the value of the pixel at the target location.

The flux densities of V445 Pup for each frequency band are given in Table 2.3; the first ten epochs are presented in this manuscript and the other epochs in Appendix A Table A.2.

2.3 Results

2.3.1 Radio light curves

Multi-frequency observations, spanning 1.5 – 43.3 GHz, reveal an unusual radio light curve for the eruption of V445 Pup between 2001 – 2008 presented in Figure 2.1. The radio light curve shows four distinct flares throughout its evolution.

Table 2.2: Log of gain calibrators used at different configurations and observing frequencies.

Observation		Gain calibrators					
Date range	Configuration	1.43 GHz	4.86 GHz	8.46 GHz	14.94 GHz	22.46 GHz	43.34 GHz
2001 Jan 18–2001 Jan 30	A	...	...	0804-278	...	...	...
2001 Sep 09–2001 Sep 14	C	0738-304	0804-278	0804-278	0804-278	0804-278	0804-278
2001 Sep 15–2001 Oct 10	C&D	0735-175	0804-278	0804-278	0804-278	0804-278	0804-278
		0806-268	0738-304				
		0706-231					
2001 Oct 12– 2002 Jan 13	D	0706-231	0738-304,	0804-278	0804-278	0804-278	0804-278
		0806-268	0804-278				
2002 Feb 07– 2002 Jun 07	A, A&B	0804-278	0804-278	0804-278	0804-278	0804-278	...
2002 Jun 17– 2002 Oct 31	B	0804-278	0804-278	0804-278	...	...	0804-278
2002 Dec 09– 2003 Jan 29	C, C&D	...	0804-278	0804-278	...	...	...
2003 Feb 06– 2003 Apr 18	D	...	0804-278	0804-278	...	...	...
2003 May 30– 2003 Oct 08	A, A&B	0735-175	0804-278	0804-278	...	...	...
		0804-278					
2003 Oct 21– 2004 Mar 02	B, B&C	0804-278	0804-278	0804-278	0804-278	0804-278	0804-278
2003 Mar 10– 2004 June 12	C, C&D	0738-304	0804-278	0804-278	...	0804-278	...
		0706-231					
2004 Jun 25– 2004 Aug 21	D	...	0804-278	0804-278	0804-278	...	...
2004 Sep 09– 2005 Feb 03	A, A&B	...	0804-278	0804-278	0804-278	...	...
2005 Feb 26– 2005 Jul 02	B, B&C	0804-278	0804-278	0804-278	...	...	...
2005 Jul 09– 2005 Oct 31	C, C&D	...	0804-278	0804-278	...	0804-278	...
2005 Nov 08– 2006 Jan 22	D	...	0738-304	0804-278	...	...	...
2006 Mar 15– 2006 May 10	A	...	...	0804-278	...	...	...
2006 Jun 25– 2006 Sep 11	B	...	0804-278	0804-278	...	...	...
2007 Sep 30–2008 Jan 17	A&B, B	...	...	0804-278	...	...	...
2007 Jan 23, 2008 Mar 28	C&D, D	...	...	0804-278	...	...	...

'...' indicates no observations at that date range and frequency.

In the earliest radio observation following the eruption of V445 Pup, around day 77, no radio emission was detected, with a 3σ upper limit of 0.34 mJy at 8.4 GHz. However, on day 89, a 4σ detection of 0.35 mJy was obtained at 8.4 GHz. Unfortunately, following the day 89 detection there were no radio observations of the nova until 312 days after eruption. As a result of very limited coverage during the first 300 days after eruption, these early points are not shown in Figure 2.1. On day 312, it became clear that V445 Pup had brightened at radio frequencies since day 89 by a factor of ~ 26 to 9.4 mJy at 8.4 GHz. Over the next ~ 3 months (see Figure 2.2), the light curve shows flux densities declining from a radio maximum, which presumably occurred before day 312.

Other flares are superimposed on the decline, like the steep peak on day 337 (at 4.9/8.5/14.9 GHz; Figure 2.2). Another flare peaked between days 450 to 460 (at 4.86/8.46/14.94 GHz bands). We note that, for the lowest frequency (1.43 GHz) light curve, these peaks occur later, at days 341 and 493 (Figure 2.2). The radio peaks observed between day $300-700$, indicated by vertical dashed lines in Figure 2.2, have sharp, rapid rises and falls in flux density, compared to the last broad peak which occurs between days 700 and 3000 (Figure 2.1). Furthermore, the flux density at the peak of the last flare is a factor of five fainter than the early-time peaks.

The last recorded flux density of the nova with the VLA was 0.19 mJy at 8.46 GHz on 2008 March 29 (day 2704). On 2009 October 29 and December 29 (days 3283 and 3325 respectively), V445 Pup was observed using the Giant Metrewave Radio Telescope (GMRT) at 1.28 GHz and 1.40 GHz (Kantharia, 2012). Radio emission was present in the first GMRT observation, with a flux density $\sim 0.3 \pm 0.08$ mJy. The second epoch yields a non-detection with a 3σ upper limit of 60 µJy (Kantharia, 2012).

2.3.2 Radio spectral evolution

We determine the spectral index for each observation (α, defined as $S_\nu \propto \nu^\alpha$, where S_ν is the flux density and ν is the observing frequency), from the slope of the line fit to the data in log-log scale. The python function `curve-fit` in the `scipy` package is used to perform the least-squares fit. Detections separated by less than a day are combined into one spectral index fit. Selected spectra are plotted in Figure 2.3, while the lower panel of Figure 2.1 shows how the spectral index varies with time.

During the first decay of the radio flux density (days $\sim 312-400$), the spectrum has a form that rises steeply toward low frequencies and is well fit with a single power law. For example, on day 314, $\alpha = -0.6$

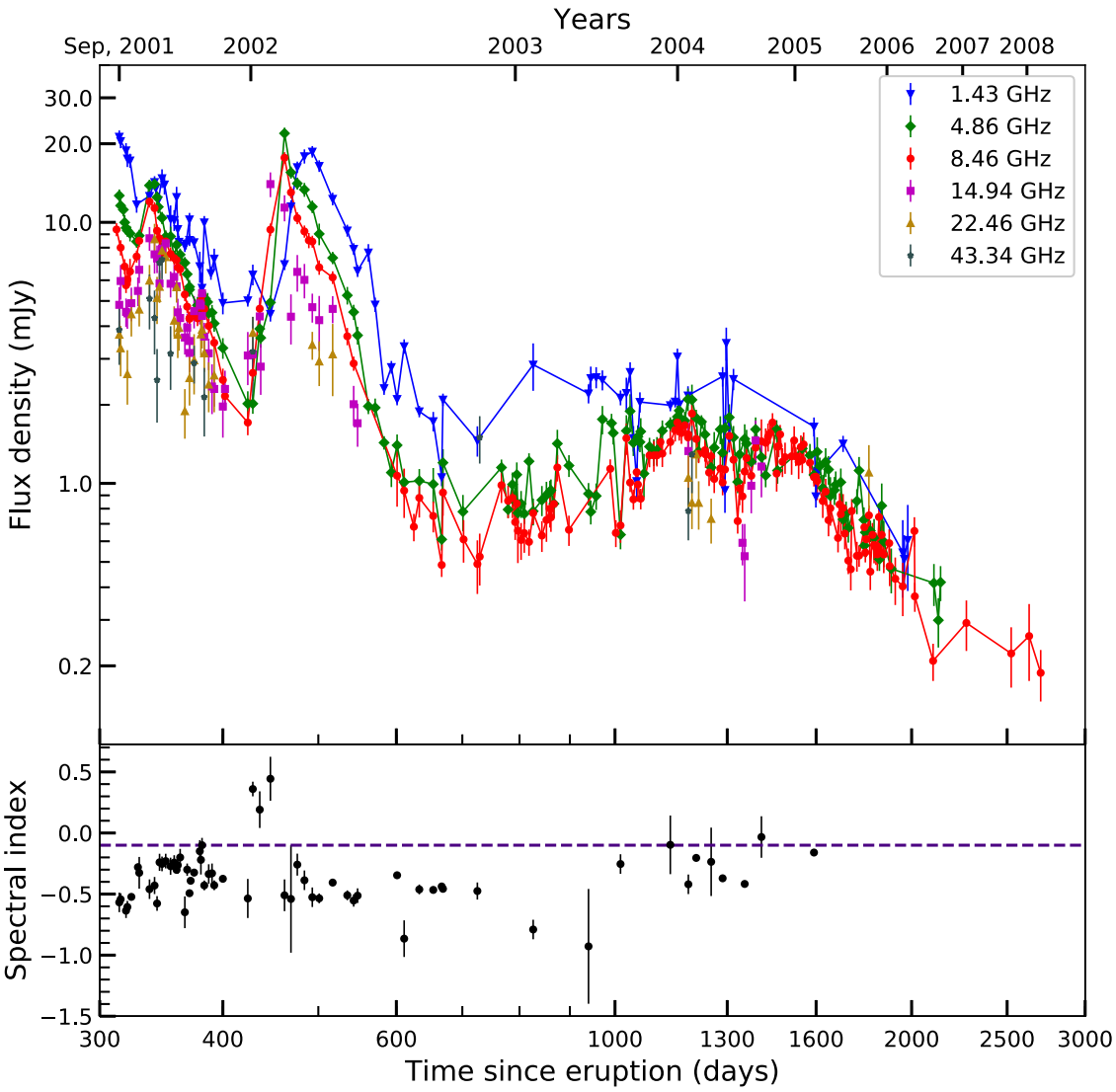

Figure 2.1: Top: Observed flux densities of V445 Pup spanning from day 300 to day 2700 after the nova eruption. We take 2000 November 02 as the date of the eruption (t_0). Bottom: spectral indices obtained by fitting a single power-law to the data. The dashed line in the lower panel represents $\alpha = -0.1$, the theoretically expected index of optically thin free-free emission.

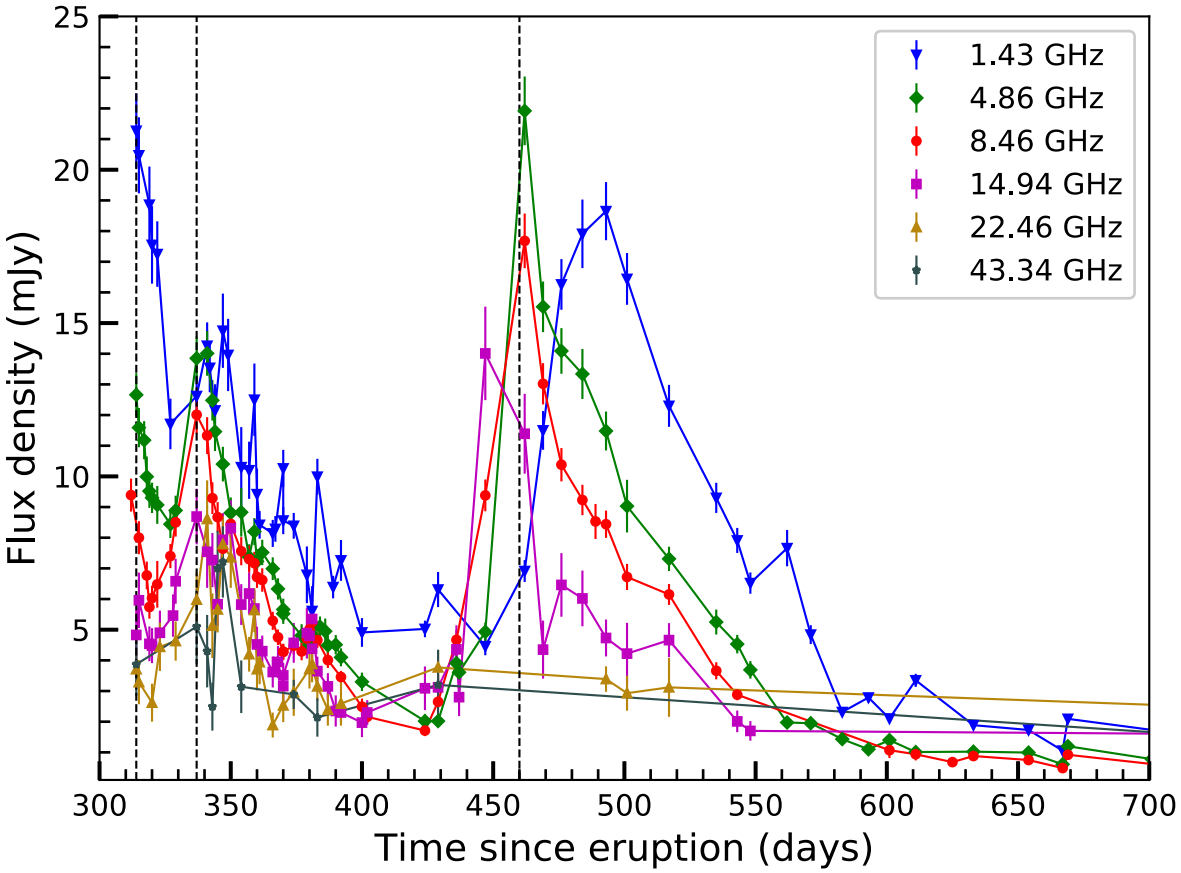

Figure 2.2: Observed flux densities of V445 Pup spanning from day 300 to day 700 after the nova eruption. Data are the same as those plotted in Figure 2.1, but zoomed in to show detail of the radio flares indicated with vertical dashed lines.

Table 2.3: Flux densities and spectral indices of V445 Pup

t	$t-t_0$	Radio flux densities (mJy)						α
(MJD)	(Days)	1.43 GHz	4.86 GHz	8.46 GHz	14.94 GHz	22.46 GHz	43.34 GHz	
51927	77	...	...	< 0.34	...	...	...	...
51939	89	...	...	0.354 ± 0.064	...	...	...	...
52162	312	...	...	9.39 ± 0.54	...	...	...	...
52164	314	21.27 ± 1.22	12.66 ± 0.71	...	4.83 ± 0.82	3.71 ± 0.50	3.87 ± 1.03	-0.57 ± 0.08
52165	315	20.47 ± 1.24	11.59 ± 0.64	8.00 ± 0.54	5.96 ± 0.90	3.29 ± 0.72	...	-0.54 ± 0.05
52167	317	...	11.18 ± 0.62	...	...	...	...	...
52168	318	...	9.99 ± 0.66	6.77 ± 0.45	...	...	...	...
52169	319	18.86 ± 1.24	9.52 ± 0.55	5.74 ± 0.38	4.54 ± 0.57	...	...	-0.64 ± 0.06
52170	320	17.55 ± 1.26	9.30 ± 0.50	6.03 ± 0.41	4.48 ± 0.57	2.62 ± 0.62	...	-0.61 ± 0.05
52173	323	17.25 ± 1.07	9.07 ± 0.62	6.48 ± 0.76	4.90 ± 0.72	4.44 ± 0.79	...	-0.52 ± 0.02
52178	328	11.71 ± 0.82	8.44 ± 0.45	7.40 ± 0.39	5.46 ± 0.69	...	...	-0.28 ± 0.03
52179	329	...	8.89 ± 0.48	8.50 ± 0.46	6.58 ± 0.73	4.63 ± 0.64	...	-0.33 ± 0.13

'...' indicates no measurements for flux density for the epoch at that frequency. This table is continued in Appendix A Table A.2.

(top left panel of Figure 2.3), an indication of optically-thin synchrotron emission (see §2.4.1 for more discussion). Sometimes the spectrum appears to flatten toward low frequency (such as on day 337) and afterwards the spectrum switches back to being well fit with a single power law (e.g., day 383.)

On days 429 and 447, the spectrum becomes inverted and rises towards higher frequencies, with $\alpha \approx 0.4$ (Figure 2.3), an indication of optically-thick emission. On days 462 and 469, the radio spectrum is transitioning back to an optically-thin state, exhibiting a combination of inverted/flat spectral index at lower frequencies and steep spectral index at higher frequencies. By day 493, the radio spectrum has returned to optically thin, hovering around $\alpha \approx -0.5$. We discuss likely causes of these changes in the radio spectrum in §2.6.1.

2.3.3 Radio Images

In its most extended A configuration, the VLA achieves angular resolution sufficient to constrain the morphology of radio emission from V445 Pup. The dates of these high-resolution observations are listed in Table 2.4, along with a brief description of the resulting images and the central position of the emission region (more details below). We fit the morphology of V445 Pup in the uv-plane, using the `UVFIT` task in `AIPS` (Greisen, 2003) and `Difmap` (Shepherd et al., 1994; Shepherd, 1997).

The VLA was in A configuration during the first observations of V445 Pup in 2001 Jan. They yielded a non-detection (Jan 17, $t - t_0 = 77$ days) and a marginal detection (Jan 30, $t - t_0 = 89$ days). The S/N was not sufficient to constrain the morphology of V445 Pup at this time.

During the 2002 A configuration ($462 - 559$ days after eruption), V445 Pup was radio bright. At 8.4 GHz, it is unresolved; model fitting with an elliptical Gaussian in the uv plane implies FWHM $< 0.1''$.

During the 2003 A configuration ($926 - 1051$ days after eruption), V445 Pup is marginally resolved. We model the 8.4 GHz data in the uv plane with an elliptical Gaussian with a major axis of $0.25'' \pm 0.04''$, unresolved minor axis ($< 0.1''$), and position angle of $92^\circ \pm 14^\circ$ (degrees east from north). Subtracting this Gaussian in the uv plane and imaging the residuals, there is some structure remaining which implies that the source is not fully described as a single Gaussian. The central position of the 2003 emission is near the 2002 position, although not consistent within the formal errors (Table 2.4). Inspection of the images

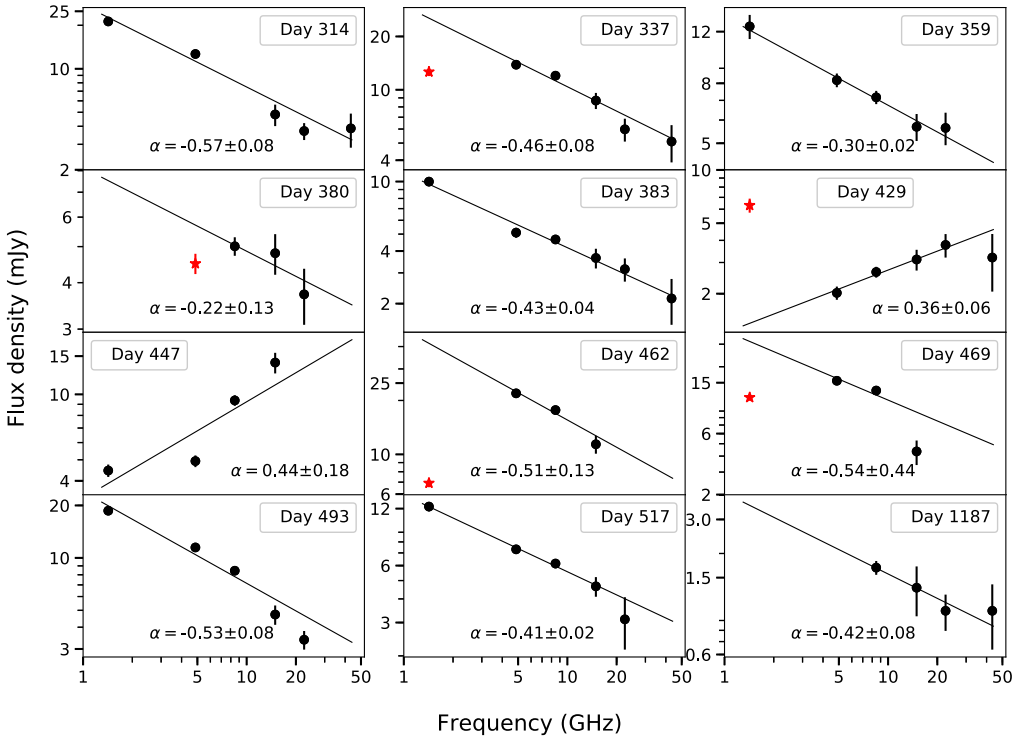

Figure 2.3: Selected VLA radio spectra of of V445 Pup, with linear fits overplotted. The time after eruption (since 2000 November 2) and the value of the spectral index is given for each spectrum. The data points marked with red stars represent flux densities in L-band (1.4 GHz) or C-band (4.9 GHz) which are relatively flat and thus not included in the fit.

Table 2.4: High-Resolution A-configuration observations of V445 Pup.

Observation Date Range	$t - t_0$ (Days)	Description	RA (J2000.0) (07h37m56.XXXs)	Dec (J2000.0) ($-25°56'58''$.XX)
2001 Jan 18–Jan 30	77–89	Marginally detected	–	–
2002 Feb 7–May 15	462–559	Unresolved, FWHM $< 0.1''$	$.885 \pm .001$	$.86 \pm .01$
2003 May 17–Sep 19	926–1051	Marginally resolved, $0.3'' \times < 0.1''$	$.880 \pm .001$	$.85 \pm .02$
2004 Sep 09–2005 Jan 6	1408–1526	Two components separated by $0.2''$	NE: $.890 \pm .002$	$.80 \pm .03$
			SW: $.875 \pm .002$	$.88 \pm .03$
2006 Feb 9–May 10	1925–2015	One component, $0.3'' \times < 0.2''$	$.883 \pm .002$	$.85 \pm .04$
2007 Jul 15–Jul 28	2446–2459	Marginally detected	–	–

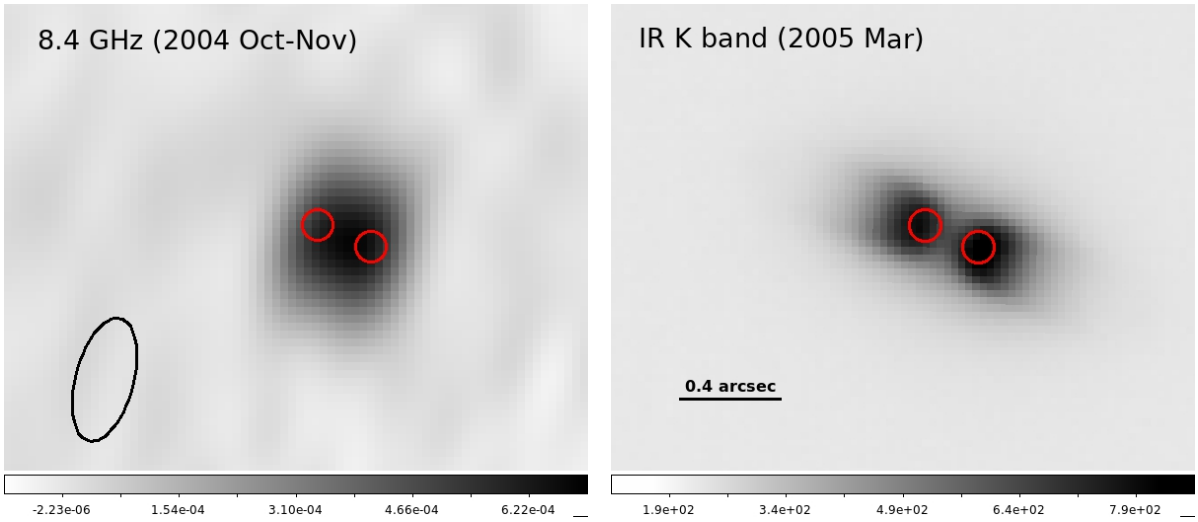

Figure 2.4: High-resolution images of V445 Pup observed at radio (left) and near-infrared (right) wavelengths. The red circles are the positions of the two Gaussian components fit to the 2004 Oct–Nov A configuration data in the *uv* plane, and have diameters of 0.12″. The left panel shows our 8.4 GHz image representing the average of data obtained between 2004 Sep 09 and 2004 Nov 29 (days 1402 – 1488). The ellipse in the bottom left corner shows the FWHM extent of the synthesized beam (0.48″ × 0.23″, PA= 165°). The right panel shows a near-IR K-band image obtained on 2005 Mar 26 (day 1605), with the same positions of the radio counterparts marked as red circles. In these images, north is up and east is to the left; and the fields-of-view are matched to be 2.4″ × 1.7″. The grey scale is linear in both cases.

implies that they likely share a common position, but the more complex morphology of the 2003 image leads to a slight apparent offset.

During the first months of the 2004 A configuration (1408 – 1488 days after eruption), V445 Pup is resolved into two distinct regions of emission that are roughly aligned with the major axis of the 2003 elliptical Gaussian fit. In the 8.4 GHz observations, the structure of V445 Pup can be fit with two circular Gaussian components separated by $0.22'' \pm 0.02''$. No significant motion of the components could be seen over ~4 months of observations. The north-eastern (NE) component's ICRS coordinates are RA = 7h37m56.890s, Dec = $-25°56'58.80''$, and the coordinates of the south-western (SW) component are RA = 7h37m56.875s, Dec = $-25°56'58.88''$. The components themselves are marginally resolved, with the NE component's FWHM = $0.16'' \pm 0.05''$ and the SW component measured to have a FWHM = $0.12'' \pm 0.03''$. The 2004 components are located on either side of the radio emission imaged in 2002/2003, consistent with them moving away from this origin position. The two 2004 components are similar in brightness, with flux densities of 0.7 ± 0.1 mJy (NE) and 0.5 ± 0.1 mJy (SW). The NE component gradually fades while the SW component gradually brightens and remains the only visible component by the end of 2004.

Figure 2.4 compares a VLA image produced by stacking the 8.4 GHz observations obtained during the 2004 A configuration with the near-IR high-resolution image, obtained by Woudt et al. (2009) on 2005 Mar 26 using the NAOS/CONICA adaptive optics system of the VLT. To make the near-IR K-band image, we downloaded several K-band exposures from the European Southern Observatory (ESO) Science Archive Facility (request #543179), stacked them to remove cosmic rays and artifacts, and applied a world coordinate system (WCS) using six stars in the image with *Gaia* Data Release 2 (DR2) positions (estimated error on our WCS is 0.02″). The near-IR K-band emission is a composite of emission lines from warm gas (e.g., He I) and warm dust continuum emission (Woudt et al., 2009).

From Figure 2.4, it is clear that the radio emission is emanating from the same bipolar regions of the V445 Pup ejecta that are dominating the near-IR emission. The two images were obtained around the same time (day ~ 1445 at 8.4 GHz, and day 1605 at near-IR K-band), and to first order, the two radio components are aligned with the peaks of the near-IR emission. Woudt et al. (2009) show that the thermal ejecta expand with a range of velocities in the polar (NE–SW) direction, while expansion in the equatorial plane is confined by a dense dust disc. It is the ejecta nearest to the dust disc that is densest and brightest in the near-IR—and also in radio emission.

We estimate the velocity at which the radio components are traveling apart from one another, assuming they were expelled on $t_0 = 51850$ MJD and V445 Pup is at a distance of 8.2 kpc. In convenient units, where V is the expansion velocity in km s^{-1} (assumed to be symmetric from a central location), d is in kpc, t is in units of 100 days, and θ is the angular separation in arcsec:

$$V = 8{,}660 \text{ km s}^{-1} \left(\frac{d}{\text{kpc}}\right) \left(\frac{\theta}{\text{arcsec}}\right) \left(\frac{100 \text{ days}}{t}\right) \tag{2.1}$$

The component separation of 0.22″ on day 1445 implies that the blobs were expanding at 1080 km s^{-1}. If we estimate that both components have FWHM of 0.12″, then the outer portions of the blobs would be separated by 0.34″, implying expansion velocities of 1670 km s^{-1}. Given these expansion velocities, it is not surprising that we do not observe significant motion during the 2004 A configuration; between 1408 and 1526 days after eruption, we would only expect the two components to move by 0.02 – 0.03″—substantially less than our observational errors (Table 2.4). The velocities of 1000 – 2000 km s^{-1} implied by the radio imaging are faster than the velocities of the P Cygni absorption troughs observed in optical spectroscopy a

few months after eruption (Iijima & Nakanishi, 2008), but are slower than the fastest expanding ejecta imaged in the near-IR by Woudt et al. (2009).

We note that the high-velocity infrared "knots" pointed out at the extremities of the bipolar V445 Pup nebula by Woudt et al. (2009)[1], seen to expand at a remarkable 8,450 km s^{-1}, would have been easily resolved in our radio images if they were radio bright. The high-velocity knots are not detected in our 2004 A configuration radio image—a clear demonstration that they are not the source of the bulk of the radio emission ~ 1500 days after eruption. Woudt et al. (2009) estimate that the high-velocity knots were ejected 345 days after t_0 (a few months before the 2002 A configuration imaging campaign). If the high-velocity knots had been radio-emitting during our 2003 A configuration campaign, they would have been separated by $\sim 0.7-0.8''$, easily resolvable with our high-resolution radio images. We therefore conclude that it is not the fastest-expanding material in V445 Pup that is dominating the radio emission at any time. Instead, our radio images imply that it is the densest material that is the site of the radio synchrotron emission.

In the 2006 A configuration (day $1925-2015$), V445 Pup has substantially faded, and its morphology has reverted to a similar structure as in 2003 (as best we can tell, given the relatively low S/N). We averaged in the uv-plane all 8.4 GHz data obtained in this A configuration, and found the data can be well-described by a single elliptical Gaussian with a major axis of $0.32'' \pm 0.08''$, unresolved minor axis ($\lesssim 0.2''$), and position angle of $68^\circ \pm 42^\circ$ (degrees east from north). The center of this emission region is consistent with the position of the 2003 emission; it is located between the 2004 components.

By the time of the 2007 A configuration, V445 Pup had faded too much for its morphology to be constrained by our VLA images.

2.4 Discussion

2.4.1 Radio Emission from V445 Pup is Synchrotron-Dominated

Historically, radio emission from hydrogen-rich classical novae was thought to be dominated by thermal free-free radiation from expanding ionized ejecta (Seaquist & Palimaka, 1977; Hjellming et al., 1979;

[1]They are not visible in the K-band image presented in Figure 2.4; this may be because we did not stack all the exposures from 2005 Mar 26, and so our image is shallower than the one published by (Woudt et al., 2009). We also did not deconvolve the K-band image as done by Woudt et al.

Seaquist & Bode, 2008). At early times, while the radio luminosity is increasing, the radio-emitting region is optically thick. As the ejecta expand and drop in density, the radio light curve peaks and turns over, as the radio photosphere recedes through the ejecta and the radio emission transitions to an optically thin state. During the optically thick phase of a thermal-dominated radio light curve, the spectral index α is expected to be equal to 2, as for blackbody emission in the Rayleigh-Jeans long-wavelength limit. When the emitting region is optically thin, the spectral index is flat ($\alpha = -0.1$), as expected for bremsstrahlung emission (e.g. § 6.2 in Pacholczyk, 1970). The radio light curve rise, peak, and decay occur on timescales of months to years—much slower than the evolution of optical light curves of novae.

The other possible source of nova radio emission is synchrotron radiation. The spectral index for optically thin synchrotron emission is set by the energy spectrum of relativistic electrons; if the number of relativistic electrons per unit energy is $N(E) \propto E^{-p}$, then the spectral index is $\alpha = (1-p)/2$. For classic diffusive shock acceleration of relativistic particles, $p = 2-2.5$, and so $\alpha = -0.5$ to -0.75 (Bell, 1978; Blandford & Ostriker, 1978). Indeed, $\alpha \approx -0.7$ is commonly observed in synchrotron-emitting SNe and SN remnants. (Chevalier, 1982b; Weiler et al., 2002). However, several novae that are strong candidates for synchrotron emitters have unusually shallow spectral indices of $\alpha \approx -0.1$ to -0.5 (Taylor et al., 1987; Eyres et al., 2009; Weston et al., 2016a; Finzell et al., 2018). This could imply shallower energy spectra for relativistic electrons in novae (compared to e.g., SNe), or that the synchrotron emitting region is inhomogeneous in terms of particle density and magnetic field strength (Vlasov et al., 2016). Optical depth effects could also flatten the spectrum; in the jets of active galactic nuclei, partially self-absorbed synchrotron emission routinely produces flat or inverted spectra of the "radio core", while the more extended transparent regions of the jet display the usual steep spectrum with $\alpha = -0.7$ (Eckart et al., 1986; Blandford et al., 2019).

The radio spectra of V445 Pup from $\sim 1-4.5$ years after optical discovery generally show higher flux densities at lower frequencies (Figure 2.3; with the exception of a few epochs which appear optically thick because of their inverted spectra). Spectral indices of V445 Pup are in the range $\alpha \approx 0$ to -1 (Figure 2.1). In the first three years of V445 Pup's evolution, its radio spectral index hovers around $\alpha = -0.5$: slightly shallower than that observed for SNe, but well within expectations of synchrotron emission (especially when taking into account the relatively shallow spectral indices observed for other synchrotron-emitting novae). After day ~ 1000, the spectral index flattens to $\alpha \approx -0.2$.

To further constrain the radio emission mechanism, we determine the brightness temperature (T_b; a parameterization of surface brightness). Nova ejecta typically have temperatures $\sim 10^4$ K, as a direct

result of the photoionization of the ejecta by the central hot white dwarf (Cunningham et al., 2015). We therefore expect the brightness temperature to be $\sim 10^4$ K for a nova in the optically-thick thermal phase of its radio evolution. As thermal radio emission transitions to optically thin, the brightness temperature is expected to drop well below 10^4 K (Weston et al., 2016a; Finzell et al., 2018). Synchrotron emission, on the other hand, can reach much higher brightness temperatures, up to $\sim 10^{11}$ K (Readhead, 1994). Therefore, if the nova's radio brightness temperature is substantially in excess of 10^4 K, this is a promising indication that it is emitting non-thermal radiation.

To estimate the brightness temperature, we must constrain the angular diameter of the object (θ) and measure its flux density (S_ν). We can then calculate the brightness temperature using the formula:

$$\frac{T_b}{\mathrm{K}} = 1.36 \times \left(\frac{\lambda}{\mathrm{cm}}\right)^2 \times \left(\frac{S_\nu}{\mathrm{mJy}}\right) \times \left(\frac{\theta_a \theta_b}{\mathrm{arcsec}^2}\right)^{-1} \tag{2.2}$$

where λ is the observing wavelength, θ_a is the major axis diameter, and θ_b is the minor axis diameter. We can estimate θ if we know the speed at which the nova ejecta are expanding (V; equation 2.1) as a function of time (t; Seaquist & Bode, 2008). We take t as the time since t_0 and estimate the expansion velocity $V = 1600$ km s^{-1} along the major axis and $V < 800$ km s^{-1} along the minor axis (inferred from radio imaging; §2.3.3). We use the observed flux densities at 1.43 GHz (21 cm), which place the strongest constraints on the brightness temperature (compared to higher frequencies).

As seen in Figure 2.5, the brightness temperature of V445 Pup starts high, $\sim 10^7$ K on day ~ 300, implying that it is undeniably synchrotron emission. The brightness temperature declines with time, to $\sim 10^5$ K by day ~ 600, and finally to $\sim 10^4$ K by day $\sim 2{,}000$. Despite a relatively low (for synchrotron emission) brightness temperature of few $\times 10^4$ K after ~ 1000 days, we conclude that this emission is non-thermal, since the spectral index implies that the emission is optically-thin. If the emission were optically-thin thermal, its brightness temperature should be substantially lower than the $\sim 10^4$ K electron temperature. Therefore, we conclude that the radio light curve of V445 Pup is dominated by synchrotron emission over ~7 years of its evolution.

2.4.2 What powers the synchrotron-emitting shocks in V445 Pup?

The general consensus is that the source of synchrotron emission in novae is due to acceleration of particles to relativistic speeds in shocks. Depending on the nature of the companion star, these shocks can be either

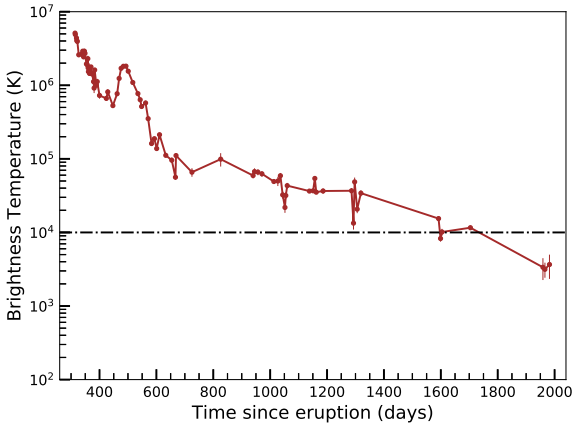

Figure 2.5: Surface brightness temperature for V445 Pup between 2001 September and 2006 April.

external with pre-existing circumbinary material or internal within the ejecta. Which is it for V445 Pup?

The clearest examples of synchrotron emission in hydrogen-rich novae come from embedded novae with red giant companions, where external shocks are produced in the interaction of the nova ejecta and the red giant wind. Examples of this type of synchrotron-emitting shocks are RS Oph (O'Brien et al., 2006; Rupen et al., 2008; Sokoloski et al., 2008; Eyres et al., 2009), V745 Sco (Kantharia et al., 2016), and V1535 Sco (Linford et al., 2017). In these cases, the radio light curve evolves relatively quickly (over ~weeks), and can be used to trace the radial density profile of the circumbinary material. A late-time thermal radio component is not observed in most cases, indicating that the ejecta are low mass (as expected for the relatively high accretion rates driven by red giant companions; e.g., Yaron et al., 2005).

Another way to produce synchrotron emission could be internal shocks within the ejecta. This type of shock likely dominates in a white dwarf system whose companion is a main sequence star, and hence the binary system is surrounded by less dense circumbinary material. Such shocks form at the interface of two outflows moving at different speeds, following a nova eruption. For decades there has been evidence of internal shocks in hydrogen-rich classical novae, based on hard X-ray emission (O'Brien et al., 1994; Mukai & Ishida, 2001; Mukai et al., 2008), and more recently, GeV γ-ray emission (Ackermann et al., 2014; Franckowiak et al., 2018; Martin et al., 2018). It has also recently been recognized that a significant fraction of these novae show evidence of non-thermal radio emission, manifesting as early bright radio flares. Novae showing evidence of synchrotron emission from internal shocks include QU Vul (Taylor et al., 1987), V959 Mon (Chomiuk et al., 2014), V1723 Aql (Weston et al., 2016a), V5589 Sgr (Weston et al., 2016b), and V1324 Sco (Finzell et al., 2018). These flares rise rapidly with time (~days–weeks), in contrast

to expectations for expanding thermal ejecta (rise time $\approx$ months), and have brightness temperatures $\gtrsim 10^5 - 10^6$ K. In most cases, a second radio maximum becomes visible at late times which is well-described as expanding thermally emitting ejecta.

Is V445 Pup's radio synchrotron emission driven by external or internal shocks? We know little about the companion star due to dust obscuration (Ashok & Banerjee, 2003; Woudt et al., 2009), so it is difficult to predict the properties of the circumbinary material surrounding V445 Pup. We can rule out external shocks with relatively spherically-distributed circumbinary material, based on our radio imaging (§2.3.3). If the pre-existing material was isotropically distributed, we would expect the synchrotron emission to be brightest at the fastest shocks (see Equation 2.3), and so to be easily resolvable (as, e.g., the near-IR high-velocity knots; Woudt et al., 2009). Instead, the radio emission is confined to much nearer the binary.

Based on radio imaging of V959 Mon, Chomiuk et al. (2014) hypothesize that at the beginning of a nova eruption, a slow outflow concentrated in the equatorial plane of the binary system is generated. A more isotropic fast wind then follows, primarily escaping in the polar directions. The collision between the two distinct flows results in shocks and particle acceleration. Based on near-infrared and radio imaging in the years following the 2000 eruption, V445 Pup exhibits a similar bipolar outflow and an equatorial disc (Woudt et al., 2009). Our radio imaging reveals that the synchrotron emission is concentrated near the equatorial plane, even $3-5$ years after explosion (§2.3.3, Figure 2.4). We also know that the equatorial disc maintains its structure for years following the eruption (Woudt et al., 2009). Therefore, interactions between a polar flow and equatorial disc, as proposed for V959 Mon, are the most likely source of the synchrotron emission.

The origin of the equatorial disc, however, is unclear. It may have pre-dated the nova eruption, as mass lost in a previous nova eruption, or from the binary during quiescence (perhaps from the outer Lagrange points during mass transfer; e.g., Pejcha et al., 2016a). Indeed, from pre-eruption photometry, Woudt et al. (2009) deduced substantial circumbinary dust around V445 Pup in quiescence. The very strong IR signatures of dust early in the eruption led Lynch et al. (2001) to surmise that the dust may have pre-dated the eruption, a conclusion also reached by Shimamoto et al. (2017) when they measured very large dust masses ($\sim 5 \times 10^{-4}$ $M_\odot$) around V445 Pup in 2006. On the other hand, in at least the case of V959 Mon, an equatorial disc-like structure was ejected during the nova eruption itself (Chomiuk et al., 2014; Linford et al., 2015). It is hypothesized that the equatorial structure was produced by the puffed-up nova envelope, marginally bound to the binary shortly after thermonuclear runaway (Chomiuk

et al., 2014). As the binary orbited inside the envelope, it transferred energy to help the envelope expand, preferentially in the equatorial direction (i.e., Pejcha et al., 2016b). It is worth noting that, unlike in V959 Mon, the equatorial disc is not observed to expand or diffuse during the eruption of V445 Pup; it remains present in imaging until at least 2015, and significant dust obscuration persists around the binary up until the present day (Woudt et al. 2021, in prep). This relative constancy of the equatorial disc over ~ two decades may suggest a pre-eruption origin.

2.5 Simple Model for Synchrotron Emission from Novae

Chevalier (1982b) developed a simple formalism for interpreting synchrotron emission from stellar explosions. The model was developed for application to SNe, where the ejecta blast wave crashes into pre-existing circumstellar material. The shock between the ejecta and the circumstellar material accelerates particles to relativistic speeds (through diffusive shock acceleration; e.g., Blandford & Ostriker, 1978; Bell, 1978) and amplifies the magnetic field (through the streaming instability; e.g., Bell, 2004). The relativistic electrons gyrate along the magnetic field lines to give rise to synchrotron emission. Here we give a few more details of how this model might be applied to V445 Pup.

The magnetic field strength in the synchrotron-emitting region is simply $B = \sqrt{8\pi U_B}$, where U_B is the magnetic energy density. The energy density of relativistic electrons is spread between electrons with a power-law distribution of energies, $dN(E) = N_0 E^{-p} dE$ where N_0 is a constant, and we assume a minimum energy of relativistic electrons equivalent to the rest mass energy of the electron (Chevalier, 1998). We take $p = 2.1$, as measured from the spectrum of V445 Pup (§2.4.1), noting that some of the equations in Chevalier (1998) are not defined for $p = 2.0$.

To convert from a magnetic field strength to physical parameters of the system, we assume a fraction of the post-shock energy density ($\rho_{\rm disc} v_{\rm w}^2$) is converted into amplified magnetic fields and relativistic electrons (as described in §2.6.1). In supernova synchrotron models, conversion factors of $\epsilon_e = \epsilon_B = 0.1$ are often assumed (e.g. Chevalier & Fransson, 2006; Chomiuk et al., 2012; Cendes et al., 2020). However, recent considerations imply that ϵ_B could be much lower ($\lesssim 0.01$, Kundu et al., 2017; Lundqvist et al., 2020), and ϵ_e may also be lower at slower shock velocities (e.g., Sarbadhicary et al., 2017). To roughly estimate the density of material surrounding V445 Pup, we take $\epsilon_e = \epsilon_B = 0.01$.

We estimate the emitting volume $V_{\rm synch} \approx 10^{47}$ cm^{-3}, as for a shell that has been expanding for 460 days at 1600 km s^{-1}, with a thickness of 10%. If we take a relatively modest flux density for V445 Pup around this time of 3 mJy at an intermediate frequency of 8.4 GHz (consistent with measurements both before and after the day 460 radio flare), this implies that the shock is interacting with material of density, ~ 3000 cm^{-3}. Given that this interaction is probably with the equatorial disc, our estimate of a spherical $V_{\rm synch}$ is over-simplistic. The implied density will increase as the volume filling factor of the synchrotron-emitting material decreases.

2.6 Synchrotron Self Absorption in V445 Pup?

Could synchrotron self-absorption be the cause of the opacity on the rise to the radio peaks? We can use the flux density at radio peak on day ~ 460, combined with a few other rough estimates of system parameters, to estimate the opacity due to synchrotron self-absorption ($\tau_{\rm SSA}$). If synchrotron self-absorption is the dominant source of opacity, we would expect $\tau_{\rm SSA} \approx 1$ at radio peak.

Using the same assumptions described in §2.5, but instead taking a flux of 12 mJy, we estimate $B = 0.01$ G. We can then plug these quantities into the equation for synchrotron self-absorption optical depth (Equation 1 of Chevalier, 1998), and find that $\tau_{\rm SSA} \approx 10^{-8}$ at the peak of the day 460 radio flare. As $\tau_{\rm SSA}$ is eight orders of magnitude smaller than unity, we conclude synchrotron self-absorption is not the dominant source of opacity. We note that for $\tau_{\rm SSA} \approx 1$, the emitting volume would need to be $V_{\rm synch} \approx 10^{38}$ cm^{-3}, a factor of a billion smaller than our estimate in §2.5—but the emitting region is directly constrained by our radio imaging (§2.3.3), and exclude this possibility.

2.6.1 Understanding the synchrotron-dominated light curve of V445 Pup

The radio synchrotron emission from V445 Pup persists for an unprecedentedly long time (~ 7 years; Figure 2.1). Synchrotron emission in other novae lasts for just a few weeks–months (Eyres et al., 2009; Weston et al., 2016a,b; Kantharia et al., 2016; Linford et al., 2017). One relatively simple way to explain the long synchrotron duration of V445 Pup would be if a wind was launched from the binary and continued blowing for years after eruption, while the equatorial disc retained its structure over this time. Then ongoing interactions between the wind and the disc would continue to power synchrotron luminosity. The standard mechanism for driving prolonged winds in novae is radiation pressure from an ~Eddington

luminosity white dwarf, powered by nuclear burning on the white dwarf's surface (Kato & Hachisu, 1994).

While ~ 7 years is relatively long for this sustained burning phase, it is not unprecedented amongst hydrogen-rich classical novae (Henze et al., 2014). The larger envelope masses in helium novae lead to expectations of longer durations for the sustained burning phase in systems like V445 Pup (~few yr – 10,000 yr; Kato & Hachisu, 2004). Therefore, a wind prolonged over ~7 years seems reasonable. Unfortunately, we are not able to directly test if a wind in V445 Pup was powered by the nuclear-burning white dwarf, as no X-ray observations of the eruption are available, and the dusty equatorial disc would likely have absorbed the white dwarf supersoft X-ray emission.

To explain the synchrotron emission from V445 Pup, we consider a cartoon model where the white dwarf wind impacts upon the equatorial disc (we assume the disc is not expanding, as it has appeared largely unchanged in imaging over ~15 years post eruption; Woudt et al., 2009, Woudt et al. 2021, in prep). We approximate that the wind expands at 1600 km s^{-1}, based on our radio imaging (§2.3.3), noting that this is the measured velocity in the polar (NE-SW) direction. We take a scenario where a wind of this velocity emanates from the white dwarf isotropically, but is decelerated in the equatorial direction by the disc, creating shocks, accelerating particles, and producing the observed synchrotron emission. We use a simple prescription for synchrotron luminosity, as described in §2.5 and largely taken from Chevalier (1982b, 1998).

We assume a fraction of the post-shock energy density is transferred to energy density of the amplified magnetic field ($U_B = \epsilon_B \rho_{\rm disc} v_{\rm w}^2$) and of relativistic electrons ($U_e = \epsilon_e \rho_{\rm disc} v_{\rm w}^2$). Here $\rho_{\rm disc}$ is the density of the pre-shock material and $v_{\rm w}$ is the velocity of the wind, ϵ_B and ϵ_e represent the fraction of the post-shock energy due to amplified magnetic fields and the relativistic electrons, respectively. We note that this is likely an oversimplification if the wind significantly decelerates in the equatorial direction, implying that a reverse shock contributes to the shock luminosity (Metzger et al., 2014). A thorough treatment of V445 Pup's shocks and resultant synchrotron luminosity requires a multi-dimensional hydrodynamics simulation, so our goal here is only to draw a simple cartoon. When the synchrotron emission is optically thin, its luminosity (L_ν) is proportional to the synchrotron-emitting volume $V_{\rm synch} \times U_e \times U_B^{(p+1)/4}$. For V445 Pup, the index of the relativistic electron energy spectrum is measured to be $p \approx 2$ (§2.4.1); therefore

$$L_\nu \propto V_{\rm synch}\, \epsilon_e\, \epsilon_B^{3/4}\, \rho_{\rm disc}^{7/4}\, v_{\rm w}^{7/2} \tag{2.3}$$

As described in §2.5, the synchrotron luminosity of V445 Pup can be explained if $\rho_{\rm disc} \approx 10^4$ cm^{-3}.

Higher synchrotron luminosities imply faster shocks and/or higher densities for interaction. Therefore, the variations in synchrotron luminosity observed in V445 Pup's light curve imply variations in the wind velocity or density of the equatorial disc—or in the optical depth. Synchrotron-dominated light curves of radio transients often show an optically-thick rise, where the flux increases as τ drops, and an optically-thin decline, usually interpreted as a decline in the density of material being shocked and/or a decline in the shock velocity (e.g., Weiler et al., 2002). V445 Pup is unusual in showing multiple peaks in its light curve (although see the embedded nova V1535 Sco for a similar albeit less dramatic case; Linford et al., 2017).

These flares are accompanied by changes in the optical depth. While most of the time the synchrotron emission appears optically thin (flux density monotonically rising toward lower frequency or $\alpha < 0$), on the rise to radio peaks, the radio spectrum flips to be brighter at higher frequencies (Figures 2.1 and 2.3). Between days 429 and 447 (on the rise to the brightest flare observed, peaking on day ~ 460), the flux density increases with frequency all the way up to 22.5 GHz, implying $\alpha = 0.2$ to 0.4. On days $337 - 341$ (rising to a slightly fainter peak on day ~ 340), the 1.4 GHz point falls substantially below the power law fit to higher-frequencies, implying that absorption is present but milder than on day 429. In both cases, the radio spectrum returns to optically thin at the peak of the radio flare, and thereafter.

The observed cyclic change in the radio spectrum of V445 Pup—starting with optically thin emission, then becoming optically-thick, then thin, and then thick and thin again—is unusual and challenging to explain (although again, similar sudden, cyclic changes of α are seen in V1535 Sco; Linford et al., 2017). With a few rough calculations, we can exclude the possibility that the optical depth is due to synchrotron self-absorption (§2.6). The optical depth is therefore due to free-free absorption, and changes in opacity mean that the ionization state of the absorbing material must be changing. The spectrum never reaches the canonical $\alpha = 2$ for free-free absorption, implying that the emission is only partially optically thick—perhaps because the $\tau \approx 1$ photospheres shrink with frequency as expected in a stellar wind (Panagia & Felli, 1975; Wright & Barlow, 1975) or because the covering factor of the absorbing screen is substantially smaller than unity (e.g., Diaz et al., 2018).

So, what might explain the observed radio flares, and attending changes in free-free opacity? One possibility is that the white dwarf wind is sweeping through the inner parts of the equatorial disc, and encountering density enhancements within it. This would imply that there are at least four regions of

enhanced density in the disc, to explain the flares on day < 300 (we only captured its decline), day 340, day 460, and day ~ 1300 (Figure 2.1). Simulations of equatorial discs produced by mass loss from the outer Lagrangian points of a mass-transferring binary often find structured discs with spiral-like density enhancements (Pejcha et al., 2016a,b). Also, based on photoionization simulations to replicate narrow emission lines of some novae spectra, its concluded that mass loss from L3 can contribute to the equatorial disc (Takeda & Diaz, 2015). The flux of V445 Pup rose by a factor of ~ 10 (from 2 mJy to 22 mJy at 4.9 GHz) between day 430 and 460. According to Equation 2.3, this would imply an increase in density of a factor of ~ 4 to explain this flare.

This interpretation is supported by the rapid declines of the radio flares, which we parameterize as $S_\nu \propto t^\beta$; the value of β can give hints on the source of the synchrotron emission. Harris et al. (2016) performed hydrodynamic simulations of a shock interacting with “shells" of enhanced density. During impact with a shell, the energy densities in relativistic electrons and magnetic fields increase dramatically, and therefore the radio light curve will peak. However, as the shock propagates to the outer side of the shell, there is no more material to sweep up, particle acceleration ceases, and the energy densities in relativistic electrons and magnetic fields rapidly drop as expected for adiabatic expansion. At this point the radio light curves decline rapidly as $L_\nu \propto t^{-11.5 \text{ to } -9}$ based on their simulations and analytical relations. Considering the declines from the radio flares on days 337 and 462 (see Figure 2.2), β is in the range $-10 \lessapprox \beta \lessapprox -9$, consistent with the shell-interaction simulations.

The other possibility is that the velocity of the wind is variable with time, and synchrotron flares are produced when it is faster. To produce a factor of ten increase in synchrotron luminosity requires a factor of ~ 2 increase in the wind velocity, according to Equation 2.3. Other nova eruptions have been observed to host multiple outflows with a range of velocities, seen in optical spectra as new absorption features and broadening emission lines (e.g., Jack et al., 2017; Aydi et al., 2019). Aydi et al. (2020) observed rapid changes in γ-ray flux and shock luminosity over the first ~ 40 days of V906 Car’s 2018 nova eruption, and attributed this to changes in outflow velocity with support from optical spectroscopy. However, the flares observed in V906 Car, and indeed most hydrogen-rich novae, occur over substantially shorter periods than the ~few years covered by our V445 Pup radio light curve. Perhaps helium nova eruptions evolve more slowly due to their likely larger envelope masses. However, this is difficult to test, as there was essentially no spectroscopic monitoring of V445 Pup during the time window 1 – 3 years after explosion, due to very heavy dust obscuration (Ashok & Banerjee, 2003; Lynch et al., 2004; Iijima & Nakanishi, 2008), and so it is difficult to constrain if or how the wind velocity changed during this time.

In either case—whether it is variations in density or velocity that produce the radio flares—the likely cause of the changes in optical depth is changes in shock luminosity. If much of this shock luminosity is radiated in the ultraviolet band, it can ionize portions of the equatorial disc ahead of it. The higher the shock luminosity, the more ionized material there will be, and the stronger the free-free absorption. The free-free absorption later dissipates, either because this material recombines or because it is swept up by the shock. We prefer the latter explanation, because if the disc material has a density $\sim 10^4$ cm^{-3} (§2.5), the recombination time should be of order a century (Ferland, 2003): much longer than the $\sim$ 200 day duration of the radio flare.

2.6.2 Is V445 Pup a SN Ia progenitor system?

As the only helium nova known, V445 Pup is often singled out as an intriguing candidate for a progenitor system to SNe Ia (e.g., Li et al., 2011; McCully et al., 2014; Kelly et al., 2014). The progenitors of SNe Ia have been constrained with radio continuum observations, where the synchrotron-emitting blast wave formalism of Chevalier and collaborators (i.e., §2.5) is used to place limits on the density and distribution of circumstellar material near the SN site (e.g., Panagia et al., 2006; Chomiuk et al., 2016; Lundqvist et al., 2020). Tested configurations of circumstellar material are usually over-simplistic, with smooth density profiles and spherical symmetry. Therefore interpretations of radio limits for SNe Ia have substantial associated uncertainty.

The fact that V445 Pup's radio light curve is synchrotron dominated and powered by interaction with an equatorial disc that likely pre-dated the nova eruption presents a unique opportunity to predict what a radio light curve of a realistic SN Ia might look like. We had originally hoped that we could simply "scale up" from nova ejecta energetics to SN ejecta energetics to predict how a SN exploding in a V445 Pup-like progenitor system would appear at radio wavelengths. However, there are two problems with this strategy. First, the synchrotron emission in V445 Pup was likely produced by a prolonged wind that continued to blow and interact with the disc for years—very different from the impulsive yet homologous explosions of SNe. Second, while the equatorial disc apparently withstood the nova eruption of V445 Pup, it is not clear if it would be destroyed by SN Ia ejecta—and on what timescale.

In the future, hydrodynamic simulations should model the V445 Pup wind/disc system and work to

constrain the mass loss rate of the white dwarf wind and the density profile of the equatorial disc, using our radio light curve as a critical constraint on the dynamics. This would inform the ejecta mass and energetics of the only helium nova known, and also recreate the circumstellar environment of one of the most promising SN Ia progenitor systems. Once the mass, extent, and morphology of the equatorial disc are better constrained, another hydrodynamic simulation could model the interaction of a SN Ia-like explosion with the disc, and make real predictions for observable signatures at radio, optical, and X-ray wavelengths that might indicate a V445 Pup-like progenitor (see Booth et al., 2016 for a similar strategy implemented on another SN Ia progenitor candidate, RS Oph).

2.7 Conclusions

The helium nova V445 Pup is observed at radio frequencies for years following its eruption in late 2000 (Figure 2.1). Steep spectral indices and high brightness temperatures imply that the radio light curve is powered by synchrotron emission through 2008; we see no evidence of thermal emission from an expanding ionized nova remnant, as seen in many other novae at radio wavelengths. The radio light curve is characterised by at least four re-brightening events, which sometimes are subject to free-free absorption on the rise but revert back to optically-thin synchrotron emission as they fade. Spatially-resolved radio images show that the synchrotron emission is more compact than the thermal ejecta and is confined near the equatorial disc imaged at near IR wavelengths (Figure 2.4).

We hypothesise that a wind from the white dwarf interacts with the equatorial disc, giving rise to shocks, particle acceleration, and synchrotron emission. This model is very similar to the scenario proposed to explain radio synchrotron and GeV γ-ray emission in hydrogen-rich classical nova V959 Mon, also based on radio imaging (Chomiuk et al., 2014). However, the data presented here on V445 Pup present the clearest case to date of synchrotron emission being associated with a dense equatorial disc in a nova. We note that, based on its high synchrotron luminosity and detection of γ-rays in other novae (Ackermann et al., 2014; Franckowiak et al., 2018), V445 Pup was likely a source of substantial GeV γ-rays, but unfortunately its eruption occurred between the *Compton Gamma-Ray Observatory* and *Fermi Gamma-Ray Space Telescope* missions.

The duration of bright synchrotron emission from V445 Pup ($\sim$ 7 years) is unprecedented amongst novae. In our model, this implies that the equatorial disc must have maintained its structure throughout

these years (a hypothesis directly supported by near IR imaging of V445 Pup; Woudt et al., 2009). In addition, the wind from the white dwarf must have persisted over these years, which is not surprising if the wind is powered by radiation pressure from sustained burning of helium on the white dwarf's surface (Kato & Hachisu, 2004). The re-brightening events in the radio light curve could be produced by changes in wind velocity or density enhancements encountered in the disc, as it is swept up by the wind. Similar fluctuations in shock luminosity have been seen in GeV γ-rays—albeit over shorter timescales—in the 2018 nova V906 Car (Aydi et al., 2020).

CHAPTER 3

RADIO OBSERVATIONS OF THE 2019 ERUPTION OF V3890 SGR

Abstract

The radio observations following the 2019 August eruption of V3890 Sagitarii obtained with the MeerKAT radio telescope at 1.28 GHz are presented. The radio light curve spans from day 1 to 300 after discovery and are dominated by synchrotron emission produced as the expanding ejected nova envelope interacts with the dense wind from an evolved companion in the binary system. The radio emission is detected early on day 6 and increases rapidly with the radio flux peaking after day 15. The radio luminosity increases due to a decrease in the opacity of the circumstellar material in front of the shocked material and fades as the density of the surrounding medium decreases and the velocity of the shock decelerates. Modelling of the light curve provides an estimated mass-loss rate of $M_{\rm wind} \approx 10^{-8}$ $\dot{\rm M}_{\odot}$ yr^{-1} for the red giant wind. V3890 Sgr hosts a massive white dwarf, shows presence of structured circumbinary material consistent with the surrounding environment present in some supernovae type Ia (SNe Ia) and therefore it is a potential SNe Ia progenitor.

3.1 Discovery and multiwavelength observations

V3890 Sgr belongs to a class of cataclysmic variables known as symbiotic recurrent novae because the accreting white dwarf has a giant companion (see §1.2.4). It is a recurrent nova because more than one thermonuclear eruption has been observed from this system; the most recent eruption occurred on 2019 August 27.9 UT as reported by A. Pereira (Strader et al., 2019). Previous eruptions of the nova were observed in 1962 June (Wenzel, 1990; Miller, 1991) and 1990 April 27.7 (e.g., Buckley et al., 1990; Anupama & Sethi, 1994). Using optical observations, Schaefer (2009) estimated an orbital period for the binary

system of 519.7 days for V3890 Sgr, and thus the nova is classified in the same class as other long period recurrent novae such as RS Oph, V745 Sco, T CrB and V2487 Oph (Anupama & Mikołajewska, 1999; Schaefer, 2009, 2010). Since some of the symbiotic recurrent novae have been extensively studied, their known parameters are listed in Table 3.1 in comparison with V3890 Sgr.

The optical light curves of these systems evolve quickly following an eruption due to the low mass of material accreted onto the surface of the white dwarf since the last nova eruption, as these systems are known to host massive white dwarfs. The ejecta outflows following an eruption are also fast, with velocities $\gtrsim 4000$ km s^{-1} measured from emission lines (see Table 3.1). The emission lines, however, narrow with time during the early phase of the ejecta evolution, as the nova ejecta are decelerated by the wind from the secondary star (e.g., Gonzalez-Riestra, 1992; Mondal et al., 2018). Shown in Figure 3.1 is direct evidence of deceleration of the nova envelope of RS Oph (Mondal et al., 2018). Based on the widths of the hydrogen Balmer emission lines measured by Mondal et al. (2018), the nova envelope first undergoes a phase of free expansion for at least four days followed by a phase of deceleration lasting up to day 80 after eruption. A similar phenomenon is observed in V745 Sco, where the velocity implied from the FWHM of Paβ emission lines decreases by a factor of ~ 3 in ~ 15 days following the 2014 eruption (Banerjee et al., 2014).

Recurrent novae have short recurrence times of less than a century (see Table 3.1), which is attributed to high accretion rates, $\dot{M} \approx 10^{-8}$ M$_\odot$ yr^{-1}, based on nova models (Yaron et al., 2005). The high rates rapidly supply enough material to power the subsequent thermonuclear runaway. Theoretically, most recurrent novae also consist of massive white dwarfs, and therefore require less mass to accumulate for hydrogen ignition (e.g., Prialnik & Kovetz, 1995; Yaron et al., 2005; Wolf et al., 2013). In symbiotic systems, the high $\dot{M}$ is acquired through mass loss from the companion red giant, which is accreted either as a wind or through a disc via the inner Lagrangian point (Luna, 2019). The mass loss via the giant's wind also contributes to a dense circumstellar environment, which is impacted by the expanding nova envelope to give rise to shocks observed at high energies such as X-rays (e.g., Bode & Kahn, 1985) and $\gamma-$rays (Abdo et al., 2010). The first $\gamma-$ray detected nova was V407 Cyg, where the binary system is embedded in a wind of a Mira-type red giant companion star (Abdo et al., 2010).

A combination of high-mass white dwarfs and high mass accretion rates make the eruptions of these systems relatively gentle, and consequently not all of the accreted material is ejected during eruption (Yaron et al., 2005). The white dwarf may therefore grow in mass towards the Chandrasekhar limit. Indeed, the white dwarfs in recurrent novae have been shown to be massive (Osborne et al., 2011; Page

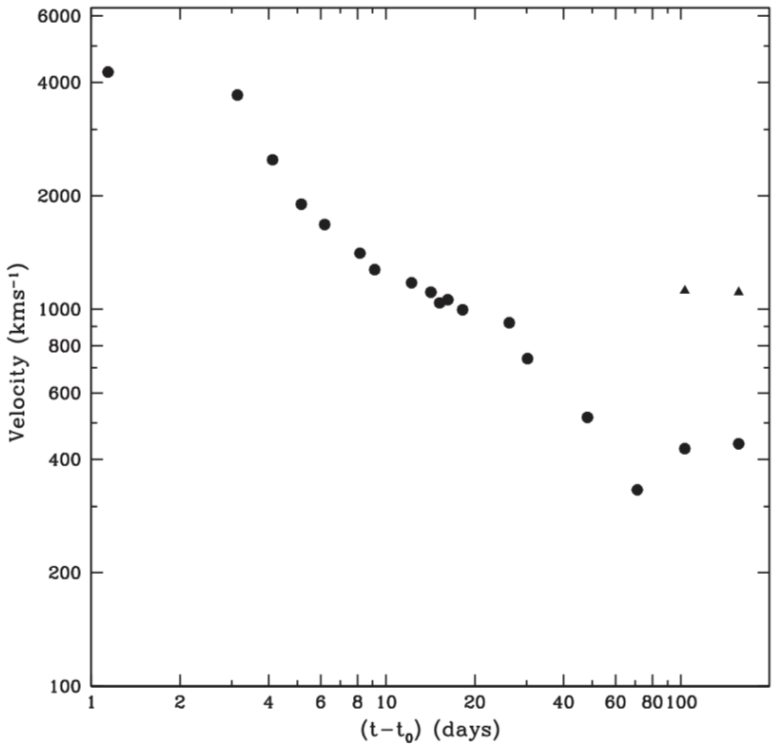

Figure 3.1: Velocity values of the ejecta expelled in the 2006 eruption of recurrent nova RS Oph obtained via width measurements of hydrogen Balmer emission lines, reproduced from Mondal et al. (2018). From day 1 to day 4, the ejecta are undergoing free expansion. Afterwards, the expanding material decelerates until day 80 when velocity starts increasing again.

Table 3.1: Estimated parameters of known symbiotic recurrent novae

Name	$M_{\rm white\ dwarf}$ $M_\odot$	$M_{\rm giant}$ $M_\odot$	Spectral type	$P_{\rm orbit}$ (days)	years of eruption	$t_{\rm rec}$ (yrs)	$V_{\rm ej}$ (km s^{-1})	t_3 (days)	d (kpc)
T CrB	1.37 (1)	1.12 (1)	M4 III (2)	228 (3)	1866, 1946	80		6 (8)	0.81 (4)
RS Oph	1.2 – 1.4 (5)	0.7– 0.8 (5)	M0–2 III (6)	453.6 (5)	1898, 1907, 1933, 1945 1958, 1967, 1985, 2006	$\gtrsim$ 10	4200 (7)	14 (8)	1.6 (9)
V745 Sco			M4 III (10)	510 (8)	1937, 1963, 1989, 2014	25	> 4000 (11)	9 (8)	7.8 (8)
V3890 Sgr			M5 III (10)	519.7 (12)	1962, 1990, 2019	28	$\gtrsim$ 4200 (13)	14 (8)	$\gtrsim$4.5 (14)

Notes: Estimated parameters of the symbiotic recurrent novae based on multiwavelength studies of individual systems. Listed parameters include masses of the binary components, the spectral classification of the companion stars, their orbital periods, years of recorded eruptions, the nova recurrence time, velocity of the ejected material, the time it takes for the nova to fade from optical maximum by 3 magnitudes, and the distance to the nova.

References: (1) Stanishev et al., 2004; (2) Mürset & Schmid, 1999; (3) Kenyon & Garcia, 1986; (4) Bailer-Jones et al., 2018; (5) Brandi et al., 2009; (6) Anupama & Mikołajewska, 1999; (7) Mondal et al., 2018; (8) Schaefer, 2010; (9) Hjellming et al., 1986; (10) Harrison et al., 1993; (11) Banerjee et al., 2014; (12) Schaefer, 2009; (13) Strader et al., 2019; (14) Munari & Walter, 2019b

et al., 2015), and these systems have therefore been proposed as progenitors of SNe Ia (Maoz et al., 2014). However, it is not clear whether the underlying white dwarfs in recurrent symbiotic novae are composed of CO or ONe. A CO white dwarf is required for a SN Ia; the fate of an ONe white dwarf that has grown in mass towards the Chandrasekhar limit is instead an accretion-induced collapse into a neutron star (Gutierrez et al., 1996).

Based on previous eruptions, the optical evolution of an eruption of V3890 Sgr is fast, taking less than a day to rise to maximum magnitude ($V \approx 8$ mag) and 14 days for the brightness to drop by 3 mag; it is therefore classified as a fast nova (Payne-Gaposchkin, 1964; Schaefer, 2010). The optical light curve from the eruption of 1962 shows similar evolution to that of the 1990 eruption (Schaefer, 2010).

The spectral evolution of V3890 Sgr at ultraviolet wavelengths shows the presence of both broad and narrow emission lines (Gonzalez-Riestra, 1992). The broad lines originate from the expanding nova ejecta, while the narrow lines represent the speed of the red giant wind (e.g., Munari, 2019). The FWHMs of the hydrogen Balmer lines decrease with time, from 2140 km s^{-1} to 210 km s^{-1} within a period of 13 days following the eruption in 1990 (Gonzalez-Riestra, 1992). This is evidence of the high velocity nova envelope being decelerated as it sweeps up its giant companion's wind.

3.1.1 The 2019 eruption of V3890 Sgr

The rise, peak and decay of the optical light curve of V3890 Sgr following the 2019 August eruption is well observed (Strader et al., 2019; Sokolovsky et al., 2019). The optical evolution of the nova shown in Figure 3.2 is similar to previous outbursts (Schaefer, 2010).

The eruption has been observed at $\gamma-$ray, X-ray, infrared, UV, optical, and radio wavelengths (Buson et al., 2019; Orio et al., 2020; Evans et al., 2019; Kuin et al., 2019; Strader et al., 2019; Nyamai et al., 2019; Munari & Walter, 2019a). V3890 Sgr was detected in γ-rays and hard X-rays very soon, (~ 2 days) following the eruption (Buson et al., 2019; Sokolovsky et al., 2019), consistent with expectations for a nova erupting in a dense environment. More details on $\gamma-$ray novae are presented in §1.2.3.4.

Presented in this chapter are radio observations of V3890 Sgr with MeerKAT at 1.28 GHz. The observations are used to study the transient phenomena of the system at radio frequencies. In §3.2, radio

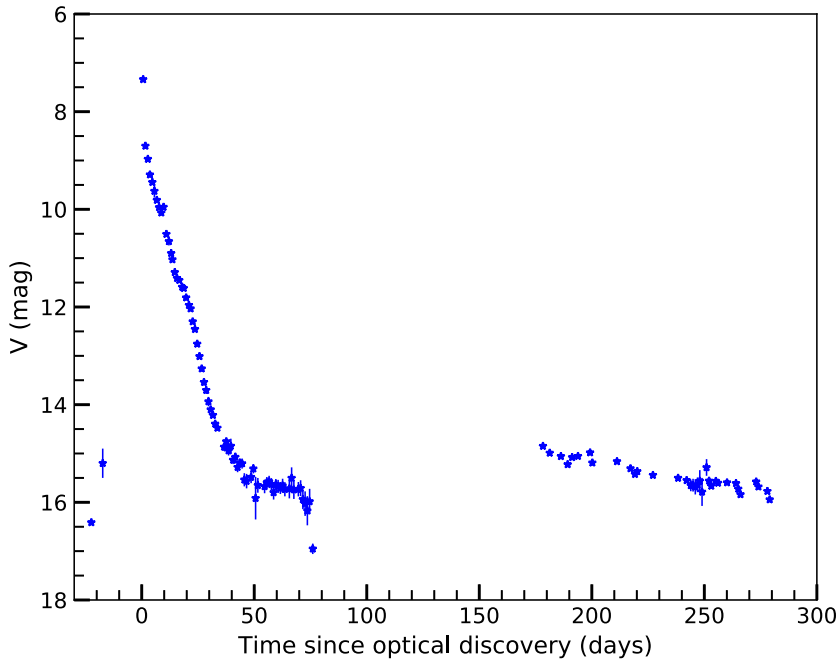

Figure 3.2: The V-band optical light curve of the 2019 eruption of V3890 Sgr from AAVSO data (Kafka, 2020). Here t_0 is assumed as MJD 58722.9.

observations and measurements including the radio light curve, radio spectral evolution and H I absorption analysis are presented. The emission from the nova, modelled as synchrotron radiation emanating from the interaction of the ejecta with the red giant wind, is presented in §3.3. The conclusions are highlighted in §3.4.

3.2 Radio observations

3.2.1 Data reduction

Monitoring of V3890 Sgr with the MeerKAT telescope started on $(t - t_0) \approx 2$ days, where t_0 is taken as 2019 August 27.9 (MJD 58722.9). The MeerKAT is a radio telescope located in South Africa and consists of 64 dishes each with a diameter of 13.5 m (Jonas & MeerKAT Team, 2016). Combined, they form a maximum baseline of 8 km. The observations were taken using the MeerKAT L-band receiver. The receiver has a total bandwidth of 856 MHz split into 4096 channels each with a width of 209 kHz. The frequency range

covered is 0.9 to 1.67 GHz centred at 1.284 GHz. In each observation, the time on target was between 15 and 30 minutes (see Table 3.2). For the first 15 days after optical discovery, V3890 Sgr was observed daily and then every two days afterwards up to day 25. Later, the observations were done once every week and finally the cadence was slowed down further to twice every month upto the end of the observations. For all the epochs, the flux and bandpass calibrator J1939-6342 was observed for ~ 5 mins. The complex gain (secondary) calibrator J1911-2006 was observed for 2 minutes per visit before and after observing the target.

Data reduction was undertaken using `CASA` (McMullin et al., 2007). To remove radio frequency interference, the data were flagged using the `AOflagger` algorithm (Offringa et al., 2012). In order to find the bandpass corrections, first, the phase-only and antenna-based delay corrections on the primary calibrator were determined. The primary calibrator bandpass corrections were then applied. This was followed by solving for complex gains for both the primary and secondary calibrators. The absolute flux of the secondary calibrator was estimated by scaling the corrections from the primary to the secondary calibrator. Calibrations and absolute flux scale were consequently transferred to V3890 Sgr (the target).

Imaging was perfomed using `WSCLEAN` (Offringa et al., 2014) using a Briggs weighting with a robust value of -0.7. The flux densities of V3890 Sgr were estimated with the `CASA IMFIT` task by fitting a Gaussian to the image of the target. Since the nova was very bright hence high signal to noise ratio, the width of the Gaussian was allowed to vary when obtaining the flux density measurements. For non-detections, the upper limit was calculated as the pixel value at the location of the nova added to $3\times$ rms value of a region in the image away from the target location. The observations and results are presented in Table 3.2 and plotted in Figure 3.3. The quoted errors of the flux densities include Gaussian fit errors ($\sigma_{\rm Fit}$) and 10% calibration errors ($\sigma_{\rm cal} = 0.1 S_\nu$), (e.g., Hewitt et al., 2020) such that

$$\sigma_{S_\nu} = \sqrt{\sigma^2_{\rm Fit} + (0.1 \times S_\nu)^2}. \tag{3.1}$$

3.2.2 Radio light curve

V3890 Sgr is the first recurrent nova to be studied with MeerKAT. The 1.28 GHz light curve is plotted in Figure 3.3. Initially, during day 2 to day 5 after eruption, the nova was not detected, with 3σ upper limits < 0.2 mJy. V3890 Sgr then shows a rapid increase in flux density, which peaked first on day 19 and again on day 60, forming a double peaked radio light curve. After the secondary peak, the nova faded to flux densities below 1 mJy.

Table 3.2: MeerKAT observations and observed flux densities of V3890 Sgr at 1.28 GHz.

Observation Date	MJD	$t - t_0$ (days)	Observation time on target (mins)	Intergrated Flux (mJy)
2019 Aug 29	58724.8	1.9	30	< 0.15
2019 Aug 30	58725.7	2.8	30	< 0.18
2019 Aug 31	58726.8	3.9	30	< 0.19
2019 Sep 01	58727.8	4.9	30	< 0.18
2019 Sep 02	58728.8	5.9	30	0.59 ± 0.07
2019 Sep 03	58729.8	6.9	30	3.10 ± 0.31
2019 Sep 04	58730.9	8.0	30	7.68 ± 0.77
2019 Sep 05	58731.9	9.0	30	11.75 ± 1.18
2019 Sep 06	58732.9	10.0	30	17.25 ± 1.73
2019 Sep 07	58733.6	10.7	30	22.29 ± 2.24
2019 Sep 08	58734.6	11.7	30	29.22 ± 2.93
2019 Sep 09	58735.8	12.9	15	36.04 ± 3.61
2019 Sep 11	58737.8	14.9	15	39.26 ± 3.93
2019 Sep 13	58739.9	17.0	15	37.95 ± 3.80
2019 Sep 15	58741.8	18.9	15	38.88 ± 3.89
2019 Sep 17	58743.9	21.0	15	38.07 ± 3.83
2019 Sep 19	58745.8	22.9	15	38.00 ± 3.81
2019 Sep 21	58747.6	24.7	15	35.14 ± 3.52
2019 Sep 26	58752.7	29.8	15	28.85 ± 2.89
2019 Sep 29	58755.7	32.8	15	27.44 ± 2.77
2019 Oct 06	58762.7	39.8	15	26.64 ± 2.67
2019 Oct 26	58782.6	59.7	20	22.95 ± 2.32
2019 Nov 18	58805.7	82.8	20	13.57 ± 1.37
2019 Nov 30	58817.6	94.7	20	9.84 ± 0.99
2019 Dec 13	58830.6	107.7	20	6.90 ± 0.71
2020 Mar 24	58932.1	209.2	15	0.91 ± 0.10
2020 Apr 14	58953.0	230.1	15	0.71 ± 0.10
2019 May 18	58988.0	265.1	15	0.44 ± 0.06
2019 May 26	58995.2	272.3	15	0.42 ± 0.06

3.2.3 Radio spectral evolution

To determine the spectral evolution of V3890 Sgr, the data were split into three sub-bands centered at 0.999 GHz, 1.285 GHz, and 1.570 GHz. Imaging was done separately for each sub-band and the flux density was determined for each image. The data are fitted by assuming a simple power law using the method of least-squares. Measurements of the spectral index (α where $S_\nu \propto \nu^\alpha$) are presented in Table 3.3 and Figure 3.3. During the early times, e.g., on day 11 the flux density rises towards higher frequency, giving $\alpha = 1.5$, an indicator of optically thick emission. Around radio light curve maximum, e.g., on day 19 the spectrum switches to rising towards lower frequency, and is well described by a power law with slope $\alpha = -0.3$. Similar values of the spectral index, $\alpha = -0.3$ are estimated between 1.26 – 7.0 GHz using the Karl G.Jansky Very Large Array and VLA Low-band Ionosphere and Transient Experiment (VLITE) (Polisensky et al., 2019). The spectrum continues to steepen (α becomes more negative) with time. By day

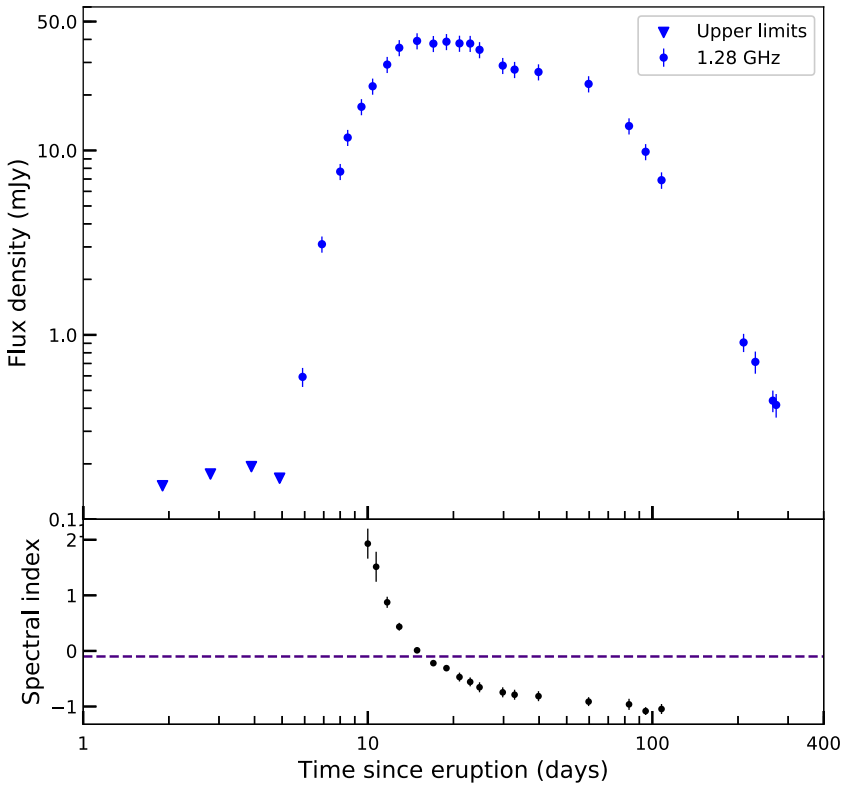

Figure 3.3: Top: Radio light curve of V3890 Sgr following the 2019 eruption, observed at 1.28 GHz with MeerKAT. Here and throughout the chapter, t_0 = MJD 58722.9. Bottom: Spectral indices obtained by fitting measured MeerKAT sub-band fluxes. The dashed line in the bottom panel represents $\alpha = -0.1$, the theoretical value of free-free emission in the optically thin limit.

108, the spectrum rises steeply towards lower frequencies and can be fit with a single power-law such that $\alpha = -1.1$, an indication of optically thin synchrotron emission.

3.2.4 H I 21-cm absorption measurements towards V3890 Sgr

The distance to V3890 Sgr is not well constrained, with estimates ranging from 4.4 kpc to 7.0 kpc using different methods (Schaefer, 2010; Munari & Walter, 2019a; Orio et al., 2020). The distance estimated using *Gaia* Data Release 2 (DR2; Orio et al., 2020) ranges between 3.1 and 7 kpc, a huge uncertainty. As pointed out by Schaefer (2018), the long orbital period of V3890 Sgr makes it difficult to obtain an accurate parallax measurement. Consequently, the distance to the nova determined via *Gaia* parallax is unreliable.

Table 3.3: Flux densities and spectral indices of V3890 Sgr

Observation date (MJD)	$t - t_0$ (days)	Integrated flux (mJy) 0.99 GHz	1.29 GHz	1.57 GHz	Spectral index α
58732.9	10.0	8.97 ± 0.90	16.12 ± 1.61	21.30 ± 2.13	1.93 ± 0.27
58733.6	10.7	13.34 ± 1.34	21.63 ± 2.17	26.24 ± 2.63	1.51 ± 0.27
58734.6	11.7	21.91 ± 2.20	28.40 ± 2.85	32.45 ± 3.25	0.88 ± 0.10
58735.8	12.9	31.13 ± 3.12	35.65 ± 3.57	37.81 ± 3.78	0.44 ± 0.07
58737.8	14.9	38.87 ± 3.90	39.21 ± 3.93	39.04 ± 3.91	0.01 ± 0.02
58739.9	17.0	40.33 ± 4.04	37.95 ± 3.80	36.53 ± 3.66	−0.22 ± 0.01
58741.8	18.9	42.36 ± 4.24	38.65 ± 3.87	36.86 ± 3.69	−0.31 ± 0.04
58743.9	21.0	43.78 ± 4.38	37.70 ± 3.77	35.48 ± 3.55	−0.47 ± 0.08
58745.8	22.9	44.20 ± 4.43	37.24 ± 3.73	34.44 ± 3.45	−0.56 ± 0.08
58747.6	24.7	41.85 ± 4.19	34.37 ± 3.44	31.22 ± 3.13	−0.65 ± 0.09
58752.7	29.8	35.19 ± 3.53	28.21 ± 2.82	25.19 ± 2.52	−0.75 ± 0.09
58755.7	32.8	33.83 ± 3.41	26.79 ± 2.70	23.75 ± 2.39	−0.79 ± 0.09
58762.7	39.8	33.17 ± 3.32	26.14 ± 2.62	23.02 ± 2.31	−0.81 ± 0.09
58782.6	59.7	29.26 ± 2.95	22.57 ± 2.27	19.42 ± 1.95	−0.91 ± 0.08
58805.7	82.8	17.92 ± 1.80	13.55 ± 1.37	11.64 ± 1.17	−0.96 ± 0.10
58817.6	94.7	13.55 ± 1.36	10.04 ± 1.01	8.32 ± 0.84	−1.08 ± 0.07
58830.6	107.7	9.23 ± 0.95	6.87 ± 0.71	5.77 ± 0.60	−1.04 ± 0.09

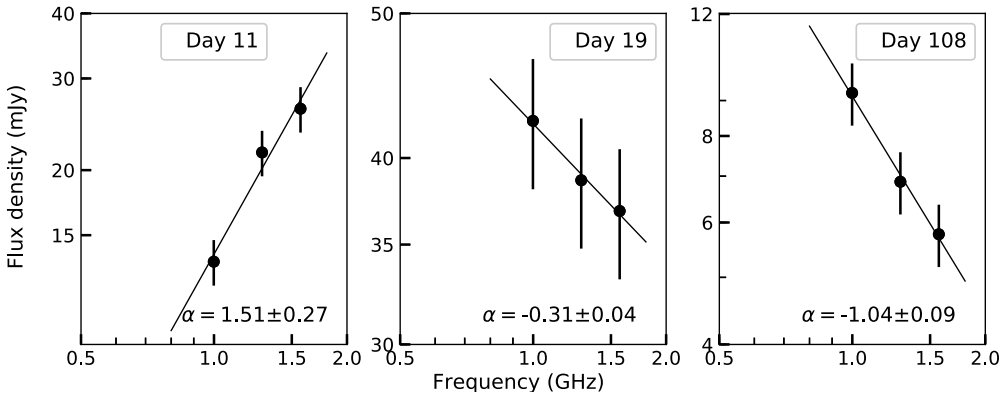

Figure 3.4: The radio spectral evolution of V3890 Sgr with linear fits overplotted, in three selected epochs observed by MeerKAT. The time after t_0 and value of the spectral index is given for each spectrum.

Following the latest eruption, Munari & Walter (2019a) determined a reddening of $E(B-V) = 0.56$ mag using absorption features of optical spectral lines. Comparing this value with the interstellar reddening maps of Green et al. (2019) and Lallement et al. (2014), they estimate a distance of > 4.5 kpc. Using the surface temperature and the size of the companion star, a black body distance of 7 kpc is derived to the nova (Schaefer, 2010). This method relies on a well established orbital period of the system and assumes that the companion star fills its Roche lobe.

Since estimates of the distance to V3890 Sgr vary based on different observations, an attempt is made

here to further constrain the distance using H I absorption along the line-of-sight to the nova (e.g., see Chauhan et al., 2021) for more details about H I absorption with MeerKAT. Figure 3.5 shows a schematic view of the velocity field of the Milky Way and the location of V3890 Sgr at Galactic coordinates $l = 9.20°$, $b = -06.44°$. The schematic shows the line-of-sight through the Galactic radial velocity field, which has a tangent point (distance of greatest velocity) close to the Galactic centre.

The epochs used to obtain the spectrum towards V3890 Sgr include radio detections of the nova when it was at its brightest (> 30 mJy). Figure 3.6 shows the average MeerKAT H I spectrum towards V3890 Sgr, compared with the average of seven reference sources (indicated by the blue spectrum in Figure 3.6) which have been offset for clarity. These reference sources are presumably background extragalactic sources, and their spectra were averaged together to yield optimal S/N. These spectra were constructed by taking an inverse-variance weighted average over spectra from seven epochs observed with MeerKAT. Line-of-sight absorption through Galactic H I clouds is detected towards V3890 Sgr. By identifying distinct kinematic components in the H I spectrum, and comparing with the spectrum of reference sources, an attempt is made to determine the distance to V3980 Sgr.

H I absorption at the level of 12% is clearly detected in both the spectra of V3890 Sgr and the reference sources. In both cases, the absorption is at a velocity of 14 ± 22 km s^{-1}, but is unfortunately unresolved by the data obtained in the MeerKAT 4k correlator mode. At the time of the observations, the 32k correlator mode was not yet available. No absorption is detected at velocities greater than 36 km s^{-1}, corresponding to kinematic distances greater than $4.44^{+0.34}_{-0.31}$ kpc (using a Monte Carlo technique in Wenger et al., 2018). This estimate is similar to the distance value obtained using *Gaia* DR2 and interstellar reddening as discussed earlier. A distance of 7 kpc is thus adopted for calculations in this work.

3.3 Discussion

3.3.1 Radio emission from V3890 Sgr is synchrotron dominated

The radio emission of novae embedded in the winds of giant stars is dominated by synchrotron emission, as observed in systems such as RS Oph (Taylor et al., 1989; O'Brien et al., 2006; Rupen et al., 2008; Sokoloski et al., 2008; Eyres et al., 2009), V745 Sco (Kantharia et al., 2016) and V1535 Sco (Linford et al., 2017). The non-thermal radio emission is the result of the ejecta interacting with the pre-existing circumstellar

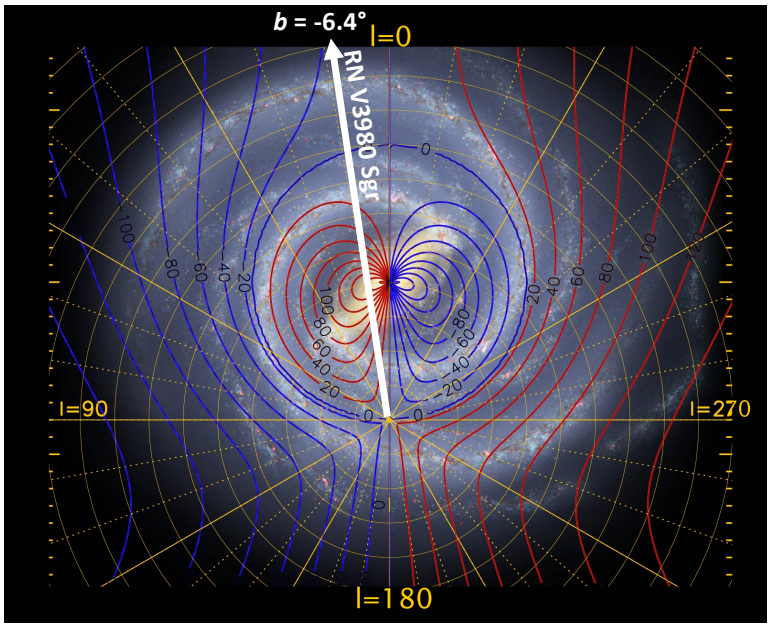

Figure 3.5: A schematic view of V3890 Sgr sight-line through the Galactic radial velocity field plotted by Robert Hurt (Spitzer Science Center/IPAC/JPL), obtained from http://www.astro.wisc.edu/ stantzos/index.html. The blue and red contours represent radial velocity values moving towards and away from the observer respectively.

medium. A nova shock wave moving outwards populates a thin region of shocked circumstellar material with accelerated particles required for non-thermal emission. The evolution of the shock wave in symbiotic novae is similar to that of SNe following an eruption (e.g., Chevalier, 1981; O'Brien et al., 2006). The flux increases as an optically thick emitting region expands. As the emitting region expands, the optical depth from the ionized red giant wind ahead of the shock decreases and the emission becomes optically thin. The fast increase in radio flux is attributed to a decrease in the optical depth of the surrounding ionized gas as the shock wave moves outward. The flux peaks when $\tau = 1$, and then decays due to the velocity of the shock wave decreasing and the decrease in the density of the surrounding medium (Chevalier, 1982b).

The radio light curve of V3890 Sgr evolves through the three phases of rise, peak and decay, within months following the nova eruption, and is similar to that of other systems with a red giant secondary star (e.g., Kantharia et al., 2016). The radio spectra of V3890 Sgr during the rise phase of the light curve yield a spectral index of $\alpha \approx 1.5$, consistent with optically thick emission. After the radio peak, the spectral index

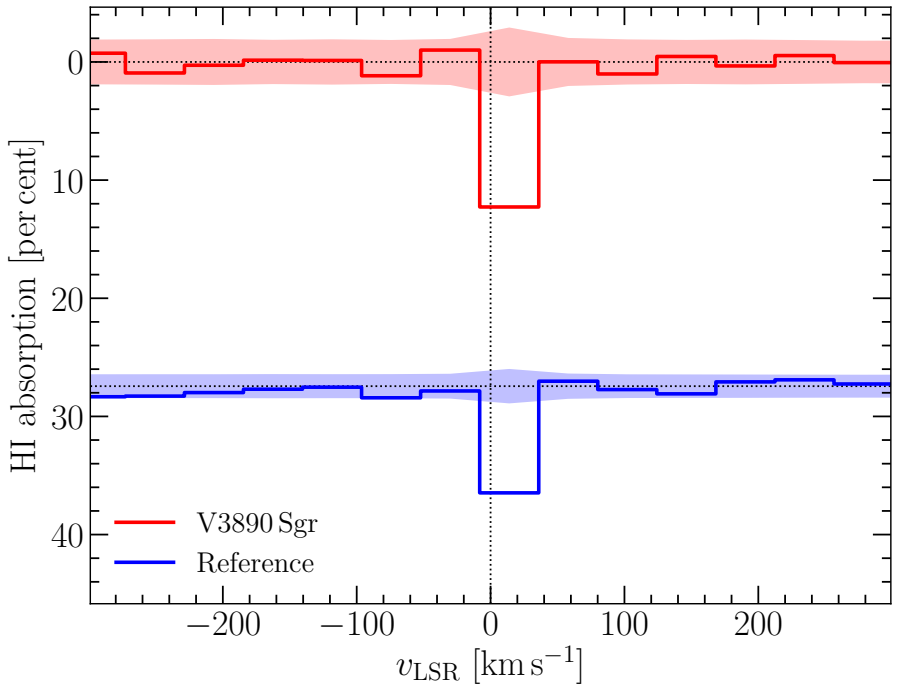

Figure 3.6: H I absorption spectrum showing an absorption between 0 and 36 km s^{-1} with respect to the local standard of rest. The spectrum of V3890 Sgr is plotted in red colour, and compared to an averaged spectrum of reference sources in blue colour. The shaded regions denote the noise level at 3σ.

is steep and converges to $\alpha = -1.0$ at late times of light curve evolution (see Figure 3.3 and Table 3.3), an indication of optically thin synchrotron emission. Similar values of α are observed in sources that are strong synchrotron emission emitters such as SNe and SN remnants (Weiler et al., 2002; Green et al., 2019).

To further constrain the type of emission from V3890 Sgr, the brightness temperature is estimated using Equation 2.2. To determine the angular size of the emitting region, a spherically symmetric shock wave expanding at ≈ 4200 km s^{-1} since t_0 is assumed (Strader et al., 2019). Using flux densities observed at 1.28 GHz (23 cm), the estimated brightness temperatures on the first 200 days are $\gg 10^5$ K as shown in Figure 3.7, a strong indicator of non-thermal emission. The brightness temperature after day 200 declines to $\approx 10^4$ K. However, during this time, the angular size of the emitting region is substantially smaller than the expected size of the emitting region, since the shock wave decelerates significantly as it interacts with the red giant wind. Therefore, $\approx$few $\times\ 10^4$ K, is a lower limit of the brightness temperature. The spectral evolution and brightness temperatures, indicate that the radio emission from V3890 Sgr is synchrotron dominated. The radio light curve of V3890 Sgr is consistent with synchrotron emission produced in a manner similar to that in SNe, where the radio light curve also evolves on timescales of weeks to months.

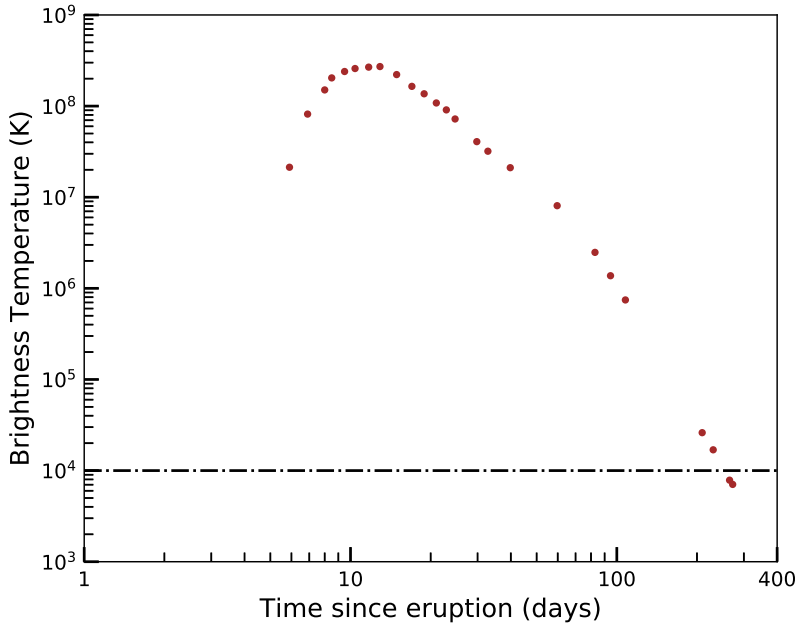

Figure 3.7: Brightness temperature of V3890 Sgr following the 2019 eruption, estimated assuming a constant shock velocity of 4200 km s^{-1}.

3.3.2 A model for synchrotron emission from blast waves

In an environment where the nova ejecta interacts with a dense surrounding medium, radio emission can be used to probe the external surrounding medium and determine its density profile as is commonly done in radio SNe (e.g., Weiler et al., 2002). The radial profile depends on the mass loss from the companion star and its shaping by binary interaction (Mohamed et al., 2013, 2015). An interaction of the nova ejecta with the companion's wind will accelerate particles to high energies through diffusive shock acceleration (Blandford & Ostriker, 1978; Bell, 1978) and amplify the shock magnetic field (Bell, 2004), producing synchrotron radiation. The interaction produces a forward shock which drives into the pre-existing circumstellar material and a reverse shock driving into the ejecta as illustrated in Figure 3.8 (Chevalier, 1982a; Reynolds, 2017). The radius of discontinuity R_s separates the forward- and reverse-shocked regions. This evolution of the shock fronts depends on the density structure of the nova ejecta, $\rho_{\rm ej}$ and that of the surrounding medium, $\rho_{\rm CSM}$ (Chevalier, 1982a).

To interpret the radio luminosity from V3890 Sgr, this double shock system is considered. Shock wave dynamics have been observed in X-rays for recurrent novae where the most notable characteristics of the shocked ejecta are high temperatures, $\gtrsim 10^7$ K and hard X-ray emission (e.g., Sokoloski et al., 2006; Bode

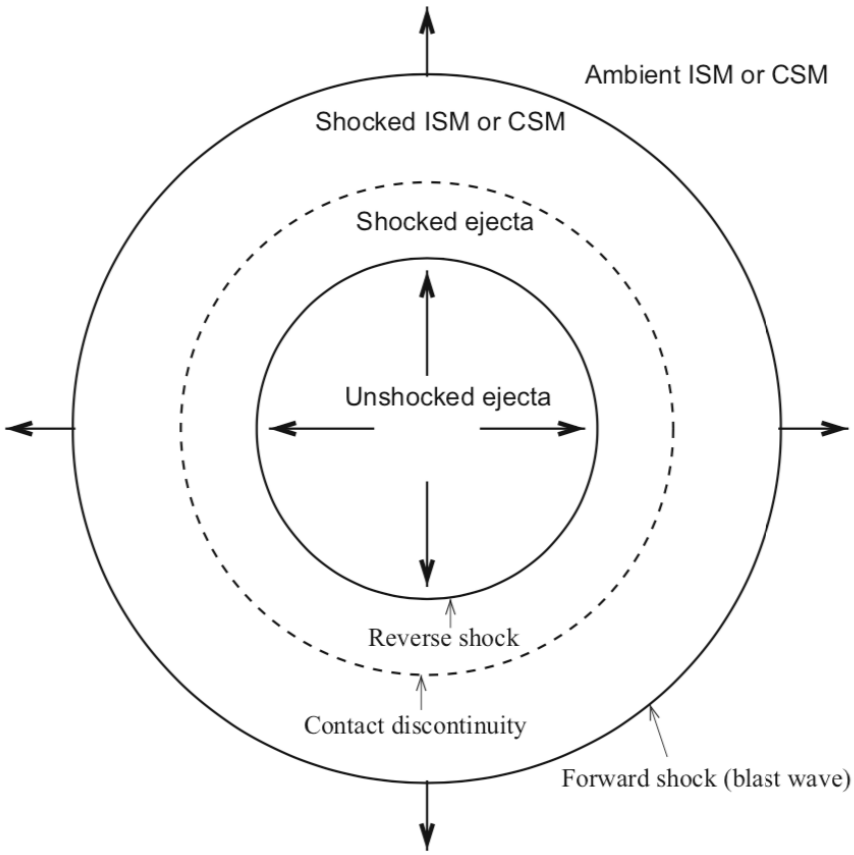

Figure 3.8: An idealized spherically symmetric remnant illustrating the formation of a forward and a reverse shock, reproduced from Reynolds (2017).

et al., 2006). Following the 2019 eruption, V3890 Sgr was shown to produce hard X-rays immediately after eruption which were attributed to the nova outflow impacting the red-giant wind (Sokolovsky et al., 2019; Orio et al., 2020). More evidence of shocks comes from the presence of high-ionization emission lines in optical spectra (Munari & Walter, 2019b).

A formalism for predicting synchrotron emission from shocks is put forward by Chevalier (1982b). The energy spectrum of relativistic electrons can be described by a power law distribution, $N(E) = N_0\ E^{-p}$ where N_0 is a constant, $N(E)$ is the number of particles with energy E, and p is the power law index of the energy spectrum. The energy of a relativistic electron is $E = \gamma mc^2$, where γ and m are the Lorentz factor and mass of an electron, respectively. The optically thin synchrotron spectrum produced by a power law distribution of electrons is also a power law, $L_\nu \propto \nu^{-(p-1)/2}$, so that the spectral index $\alpha = -(p-1)/2$. For V3890 Sgr, an average value of $\alpha \approx -0.7$ is measured in the optically thin limit of the radio light curve. This translates to $p = 2.4$. For the non-relativistic shocks in novae, the minimum energy is taken to be the

rest mass energy of the electron (Chevalier, 1998).

The post-shock energy density is described as $U_{\rm shock} = \rho_{\rm CSM}\, v_s^2$, where $\rho_{\rm CSM}$ is the density of the material being shocked and $v_{\rm shock}$ is the velocity of the forward shock. In Chevalier's model, it is assumed that a fraction of the post-shock energy density is transferred to the accelerated electrons and the amplified magnetic field. Therefore, the energy density in accelerated electrons is $U_e = \epsilon_e\, \rho_{\rm CSM}\, v_{\rm shock}^2$, and the energy density in the magnetic field is $U_B = \epsilon_B\, \rho_{\rm CSM}\, v_{\rm shock}^2$. The efficiency factors ϵ_e and ϵ_B are used to describe the fraction of the post-shock energy in the form of relativistic electrons and amplified magnetic fields, respectively.

Chevalier expresses the flux density of synchrotron emission as

$$S_\nu = 1.8 \times 10^{-22} \times \left(\frac{\pi R^2}{D^2}\right) \frac{C_5}{C_6}\, B^{-0.5}\, \nu^{2.5} \times \left(1 - \exp\left[-\frac{\nu}{\nu_1}^{\frac{-p-4}{2}}\right]\right) \text{mJy}. \tag{3.2}$$

Constants C_5 and C_6 are determined as a function of p (Pacholczyk, 1970). For V3890 Sgr, $p = 2.4$ as measured from the optically thin spectral index and D is the distance to the nova. Therefore, the values $C_5 = 9.68 \times 10^{-24}$ and $C_6 = 8.10 \times 10^{-41}$ for $p = 2.5$ are used here. ν_1 is the frequency at which the optical depth to synchrotron self-absorption (SSA) is equal to unity, given as

$$\nu_1 = 1.3 \times 10^{19} \times \left(\frac{4}{3} f\, R\, C_6\, N_0\right)^{\frac{2}{p+4}} \times B^{\left(\frac{p+2}{p+4}\right)} \text{Hz}. \tag{3.3}$$

The synchrotron emitting region is assumed to be between the forward shock and the contact discontinuity, quantified as f (see Figure 3.8). We estimate the value of $f = 0.88$ using the approximations of the forward shock radius and the contact discontinuity radius given in Tang & Chevalier (2017). The strength of the magnetic field is given by $B = \sqrt{8\pi U_B}$. The normalization factor yielding the number density of electrons emitting non-thermal radiation is given as

$$N_0 = \frac{\frac{\epsilon_e}{\epsilon_B} B^2 (p-2) E^{p-2}}{8\pi} \tag{3.4}$$

where the definition is valid for $p > 2$.

Radio synchrotron luminosity may increase at early times due to SSA or free-free absorption by the ionized gas ahead of the forward shock, depending on the amplified magnetic field, the density of the external medium and the shock wave velocity (Chevalier, 1998; Weiler et al., 1986). It has been shown that free-free absorption is dominant for slow shock wave velocities ($\lesssim 10^4$ km s^{-1}) while SSA is the dominant source of opacity for faster blast waves (Chevalier, 1998; Panagia et al., 2006). In cases where the optical depth is dominated by an ionized wind-like medium (as described in §3.3.3.2) ahead of the shock, the free-free optical depth is defined by Chevalier (1981) as

$$\tau_{\rm ff} = 0.005 \left(\frac{\dot{M}}{10^{-6}\ {\rm M}_\odot\ {\rm yr}^{-1}} \right)^2 \times \left(\frac{v_{\rm wind}}{10\ {\rm km\ s}^{-1}} \right)^{-2} \times \left(\frac{\nu}{1.4\ {\rm GHz}} \right)^{-2} \times \left(\frac{R_s}{2 \times 10^{16}\ {\rm cm}} \right)^{-3}$$

3.3.3 The dynamics of the blast wave

To predict the radio luminosity of a nova interacting with circumbinary material, we must know the radius and velocity of the blast wave. These depend on the density and velocity structure of the nova ejecta, along with the density profile of the circumbinary material.

3.3.3.1 The density structure of the nova ejecta

The unshocked material of the nova envelope is simply and commonly described as expanding freely and homologously, such that $V(r) \propto r$ where V is the expansion velocity and r is radial distance from the white dwarf. In this case, the ejecta would show a range of velocities with the inner ejecta characterised by low velocities and the outer ejecta expanding fastest. Based on the modelling of nova remnants, the density profiles of the ejecta can be described by a power law distribution, $\rho_{\rm ej} \propto r^{-n}$ with inner ejecta having $n = 2$ or 3 and outer ejecta having n between 10 and 20 (e.g., Hauschildt et al., 1997). Only a tiny fraction of the ejecta mass is found in the outer parts characterised by a steep power law (and this mass will be swept up very quickly, in just a few hours), so a shallow power law is adopted to describe the ejecta density profile of V3890 Sgr, such that $n = 2$.

Observationally, the ejected masses of symbiotic recurrent novae are in the range of 10^{-7}–10^{-6} $M_\odot$ (O'Brien et al., 1992; Anupama & Sethi, 1994; Sokoloski et al., 2006; Orlando et al., 2017). After the 1990 eruption of V3890 Sgr, the optical light curve at V band declined by three magnitude in 14 days (Figure 3.2). Such a fast decline is expected for nova envelopes with mass of $< 10^{-6}$ $M_\odot$ (Yaron et al., 2005). Furthermore, the same rapid decay of the optical light curve is observed in RS Oph, where its ejected nova envelope is estimated to be ($10^{-7} \leq M_{\rm ej} \leq 10^{-6}$) $M_\odot$ (e.g., O'Brien et al., 1992; Sokoloski et al., 2006). More evidence of a low-mass ejected envelope in V3890 Sgr is based on the fast nova evolution where high-ionization lines appear in the spectra ≈ 18 day following the 1990 eruption (Anupama & Sethi, 1994). Anupama & Sethi use Balmer emission line fluxes to estimate the mass of the nova envelope as $\approx 10^{-7}$ $M_\odot$.

3.3.3.2 The density structure of the circumstellar medium

The simplest model for the circumstellar material is to assume the companion star is expelling a spherically symmetric wind with constant velocity and mass-loss rate. The density distribution of the medium is then

described as

$$\rho_{\rm CSM} = \frac{\dot{M}}{4\pi v_{\rm wind}} r^{-2} \tag{3.5}$$

where $\dot{M}$ is the mass loss rate, $v_{\rm wind}$ is the velocity of the red giant wind, and r is the distance from the companion binary.

Without prior knowledge of the distribution of circumstellar material, this spherical distribution of the red giant wind is assumed for V3890 Sgr. It is however noted that non-spherical distribution of material is common in symbiotic recurrent systems. Furthermore, the two components observed in the emission line profiles of V3890 Sgr following the 1990 eruption indicate that the nova remnant is non-spherical (Anupama & Sethi, 1994). A spherical assumption considered here is therefore a simplistic approach.

3.3.3.3 Radius and velocity of the shock front

The time evolution of a shock wave propagating through the red giant wind is divided into two phases. During the first phase, when the mass of the nova envelope ($M_{\rm ej}$) is much larger than that of the swept-up surrounding medium ($M_{\rm sw}$), the shock is in free expansion. As the mass of the swept up material increases such that $M_{\rm sw} > M_{\rm ej}$, the nova envelope enters a second phase of evolution referred to as the Sedov-Taylor phase. For spherical nova ejecta with a power-law density profile ($\rho_{\rm ej} \propto r^{-2}$) interacting with circumstellar medium of density, $\rho_{\rm CSM} \propto r^{-2}$, self-similar solutions are determined for the evolution from a free expansion phase to the adiabatic expansion phase, as shown in Table 1 of Tang & Chevalier (2017). The approximation of radial distance considered in this model to determine the mass-loss rate of the red giant is that from the white dwarf since shocked ejecta expands and extends outside the binary system at least within a day (see Figure 3.9). The density distribution profile is thus conserved.

Tang & Chevalier (2017) present expressions for the radius and velocity of the forward shock with time, given as $R_s = R_{ch} \times R_b^*$, $v_s = v_{ch} \times v_b^*$, and $t = t_{ch} \times t^*$. Here R_{ch}, v_{ch}, and t_{ch} are the characteristic radius, velocity and time respectively:

$$\begin{aligned} R_{ch} &= 12.9 \times \left(\frac{M_{\rm ej}}{\rm M_\odot}\right) \times \left(\frac{\dot{M}}{10^{-5}\ \rm M_\odot yr^{-1}}\right)^{-1} \times \left(\frac{v_{\rm wind}}{10\ \rm km\ s^{-1}}\right) \rm pc \\ t_{ch} &= 1770 \times \left(\frac{E}{10^{51}\ \rm erg}\right)^{-0.5} \times \left(\frac{M_{\rm ej}}{\rm M_\odot}\right)^{1.5} \times \left(\frac{\dot{M}}{10^{-5}\ \rm M_\odot yr^{-1}}\right)^{-1} \left(\frac{v_{\rm wind}}{10\ \rm km\ s^{-1}}\right) \rm yr \\ v_{ch} &= 7126.28 \times \left(\frac{E}{10^{51}\ \rm erg}\right)^{0.5} \left(\frac{M_{\rm ej}}{\rm M_\odot}\right)^{-0.5} \rm km\ s^{-1} \end{aligned} \tag{3.6}$$

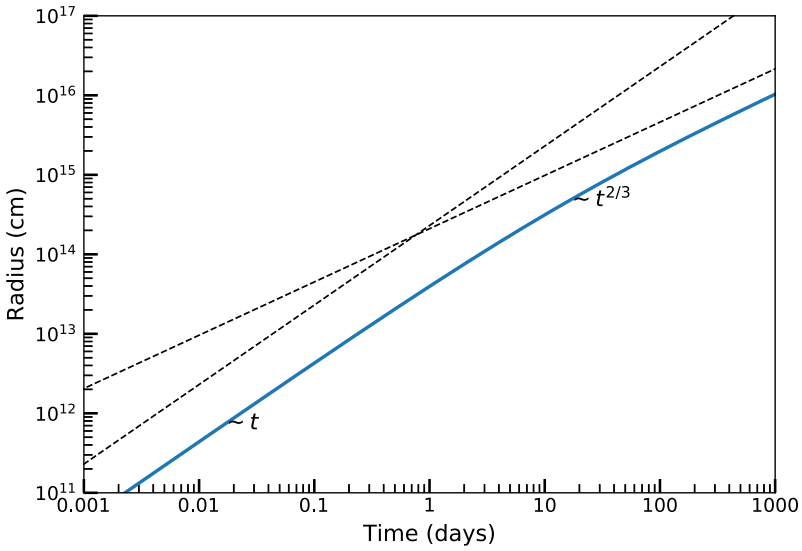

Figure 3.9: Radial evolution with time of nova ejecta interacting with a circumstellar material. This represents the free expansion and the Sedov-Taylor phase of the evolution.

E is the kinetic energy of the nova ejecta. R_b^*, v_b^* are the analytical dimensionless quantities defined by Tang & Chevalier (2017), and can be written as

$$R_b^* = 2.91489 \times t^* (1 + 9.36843 t^{*0.567})^{-0.5882}$$
$$V_b^* = \frac{dR^*}{dt^*} = (2.91489 \; + \; 18.2 t^{*0.567})(1 \; + \; 9.36843 t^{*0.567})^{-1.5882} \tag{3.7}$$

The predicted radius (R_s) and velocity (v_s) of the blast wave are shown in Figure 3.9 and Figure 3.10. The radius and velocity of the shock depend on the ejecta mass ($\approx 10^{-5} - 10^{-7}$ $M_\odot$) and kinetic energy of the nova ejecta, along with the density of the circumbinary material (i.e., $\dot{M}/v_{\rm wind}$). The shock radius first grows linearly with t and later as $t^{0.67}$. Similarly, the shock wave velocity first remains at a near-constant value but decreases as $t^{-0.33}$ at later times. The flux densities depend on these quantities, but also on the distance to the nova, ϵ_e, and ϵ_B.

3.3.4 Modelling the radio light curve of V3890 Sgr

The radio light curve of V3890 Sgr is compared to the model used to explain non-thermal emission in supernova explosions (§3.3.2; Chevalier, 1998). The model depends on various input parameters, including: $p = 2.4$, $v_{\rm wind} = 10$ km s^{-1}, and distance to the nova of 7 kpc. The velocity and radial profile of the expanding material are as discussed in §3.3.3.3, but we tweaked $M_{\rm ej}/E$ to yield maximum expansion velocities at

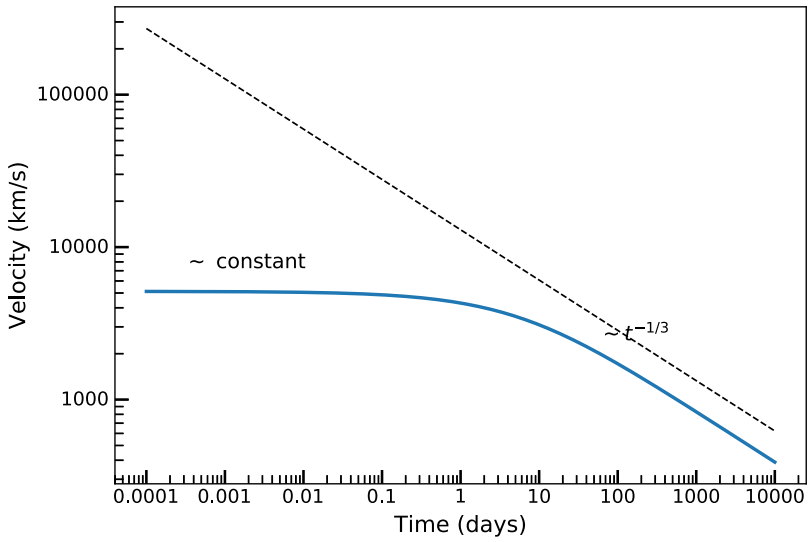

Figure 3.10: Velocity evolution with time of nova ejecta as it interacts with the surrounding medium. At the beginning of the evolution during the free expansion phase, the velocity is constant and begins to decrease at the Sedov-Taylor phase of the evolution.

early times (i.e., during free expansion; Figure 3.10) consistent with observations. For V3890 Sgr, we use a maximum ejecta velocity of ≈ 4200 km s^{-1}, as estimated from optical spectroscopy (Strader et al., 2019).

First, we consider a range of $M_{\rm ej}$ between $M_{\rm ej} = 10^{-5}$ M$_\odot$ and 10^{-7} M$_\odot$. The synchrotron model shown in Figure 3.11 shows model radio light curves for three different ejecta masses: $M_{\rm ej} = 10^{-5}$ M$_\odot$, 10^{-6} M$_\odot$, and 10^{-7} M$_\odot$. In all three cases, we assume $\dot{M} = 10^{-8}$ M$_\odot$ yr^{-1} for $v_{\rm wind} = 10$ km s^{-1} and $\epsilon_e = \epsilon_B = 0.004$. This is consistent with estimates of particle acceleration implied through modelling of γ-ray emission from a symbiotic nova (e.g Abdo et al., 2010). We also hold $M_{\rm ej}/E$ constant as described above. A higher ejecta mass, and consequently a higher kinetic energy, causes the light curve to become brighter and the radio emission to last longer. With the above assumptions, the model with $M_{\rm ej} = 10^{-6}$ M$_\odot$ agrees well with the data during the rise and peak of the radio emission. None of the models predict the decay phase of the radio light curve accurately. A discussion of why this is the case is included in the next section.

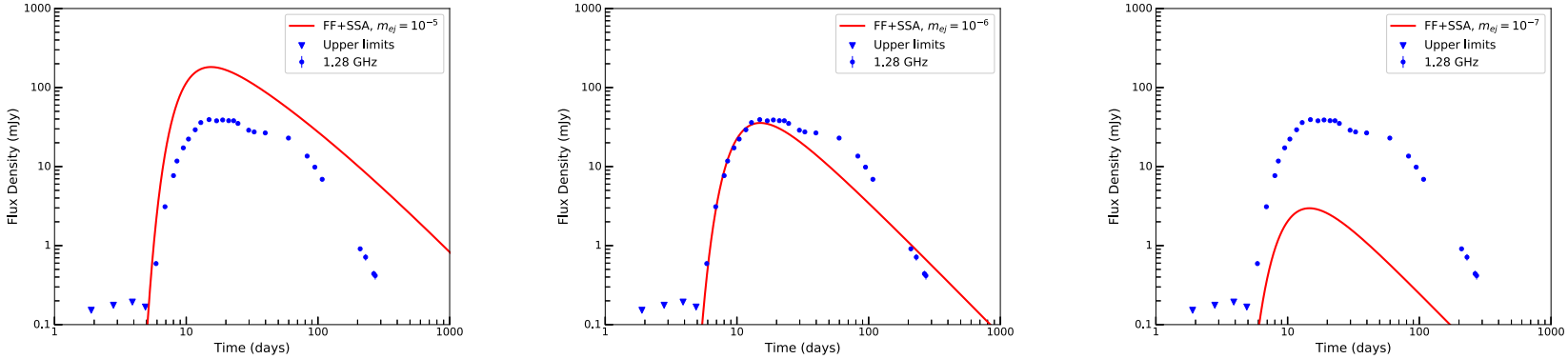

Figure 3.11: Models of radio emission produced by synchrotron emission undergoing free-free absorption represented as red solid lines superimposed on the MeerKAT light curve. The left plot shows a model for massive ejection of $M_{\rm ej} = 10^{-5}$ M$_\odot$ which does not match the data well. The middle plot shows a model for $M_{\rm ej} = 10^{-6}$ M$_\odot$ that shows a good match during the rise and peak of the radio emission. The right plot represents a model for $M_{\rm ej} = 10^{-7}$ M$_\odot$ which does not match the measured flux densities. All the models were produced with $\dot{M} = 1.8 - 3.9 \times 10^{-8}$ M$_\odot$ yr^{-1} for $v_{\rm wind} = 10$ km s^{-1} and $\epsilon_e = \epsilon_B = 0.004$.

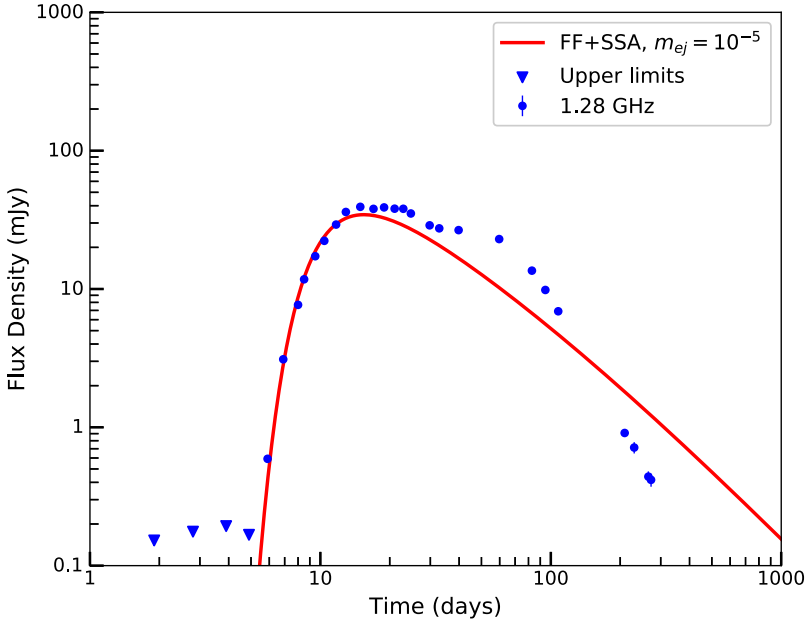

Figure 3.12: Model of radio emission produced by synchrotron emission undergoing free-free absorption represented as red solid lines superimposed on the MeerKAT light curve for a massive ejection $M_{\rm ej} = 10^{-5}$ $M_\odot$, equipartition of energy such that $\epsilon_e = \epsilon_B < 0.004$ and $\dot{M} = 4.0 \times 10^{-8}$ $M_\odot$ yr^{-1} for $v_{\rm wind} = 10$ km s^{-1}.

For the more massive ejection ($M_{\rm ej} = 10^{-5}$ $M_\odot$) to not overpredict the radio flux densities, the model would require less energy in accelerated particles and amplified magnetic fields, such that $\epsilon_e = \epsilon_B < 0.004$. Adopting these values and keeping all other assumptions the same as earlier models, produces a model with $\dot{M} = 4.0 \times 10^{-8}$ $M_\odot$ yr^{-1} for $v_{\rm wind} = 10$ km s^{-1}, shown in Figure 3.12. A decrease in $\dot{M}$ predicts an early detection of the radio emission while an increase in $\dot{M}$ predicts a late detection of the radio emission, which is inconsistent with the rise part of the radio light curve but matches with the peak of the radio light curve.

For the less massive ejection ($M_{\rm ej} = 10^{-7}$ $M_\odot$) to not underpredict the radio flux densities, the model requires high energy in accelerated particles and amplified magnetic fields such that $\epsilon_e = \epsilon_B = 0.01$. These conversion factors are often used in supernovae synchrotron emission models, while recent observations of some supernovae imply $\epsilon_B < 0.01$ (Lundqvist et al., 2020). Adopting these values and keeping all other assumptions the same as earlier models, produces Figure 3.13 with $\dot{M} = 2.0 \times 10^{-8}$ $M_\odot$ yr^{-1} for $v_{\rm wind} = 10$ km s^{-1}. A decrease in $\dot{M}$ predicts an early detection of the radio emission while an increase in

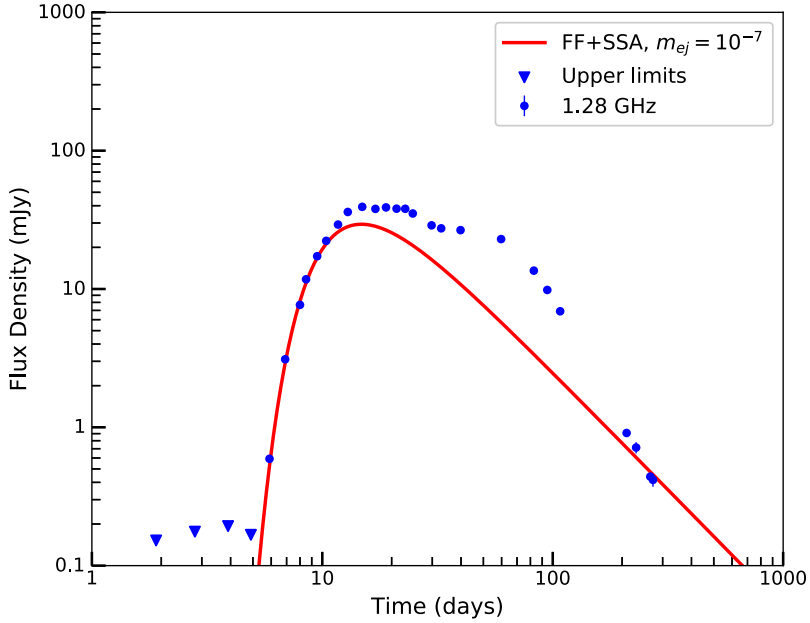

Figure 3.13: Model of radio emission produced by synchrotron emission undergoing free-free absorption represented as red solid lines superimposed on the MeerKAT light curve for a less massive ejection $M_{\rm ej} = 10^{-7}$ M$_\odot$, energy such that $\epsilon_e = 0.1$ and $\epsilon_B = 0.01$ with $\dot{M} = 2.0 \times 10^{-8}$ M$_\odot$ yr^{-1} for $v_{\rm wind} = 10$ km s^{-1}.

$\dot{M}$ predicts a late detection of the radio emission, which is inconsistent with the radio light curve. However, the less massive ejection model should be considered with caution since ϵ_e has been shown to be lower than 0.01 in non-relativistic shocks (Sarbadhicary et al., 2017).

Since the more massive ejecta of $M_{\rm ej} = 10^{-5}$ M$_\odot$ is inconsistent with the fast decay of the optical light curve and theoretical models as explained in §3.3.3.1, the ejecta mass of V3890 Sgr following the 2019 eruption is likely to be $M_{\rm ej} = 10^{-6}$ M$_\odot$.

Even though the prediction of synchrotron luminosity is sensitive to the assumptions made, in all the cases presented above, the radio light curve provides an estimate of the mass-loss rate of the red-giant companion in the range of $1.8 - 4.0 \times 10^{-8}$ M$_\odot$ yr^{-1}. Using radio observations and assuming a spherically symmetrically distributed ionized gas in symbiotic systems, Seaquist & Taylor (1990) determined $\dot{M} = 10^{-7}$ M$_\odot$ yr^{-1} for most red giant stars assuming $v_{\rm wind}$= 10 km s^{-1}. However, recent studies of the most studied recurrent nova RS Oph imply a mass loss rate of 10^{-8} M$_\odot$ yr^{-1} (Vaytet et al., 2007; Van Loon, 2008). The mass-loss rate of V3890 Sgr estimated from its radio light curve is in the range of those found

for red giants in symbiotic systems and RS Oph.

3.3.4.1 Explaining the second radio light curve peak

The synchrotron luminosity produced when a nova remnant interacts with the circumstellar medium is expected to rise, peak and decay in a span of few months (Kantharia, 2012). The radio luminosity in this framework decays during the optically thin phase of the radio light curve due to a decrease in circumbinary density and/or shock wave velocity (Weiler et al., 2002). The luminosity of V3890 Sgr stays brighter than expected compared to the model, interpreted as a second peak of the radio non-thermal light curve. This peak cannot therefore be explained by a single interaction with a spherically distributed wind-like circumstellar medium.

Double peaked radio light curves have been observed previously in novae with giant companions, but on different timescales. For example the radio light curve of the 2006 eruption of nova RS Oph showed a first peak around day 8, which was followed by a second peak on day 40 (Eyres et al., 2009). Based on its spectral evolution, the authors concluded that the radio emission from the nova is mixed thermal and non-thermal radiation. V1535 Sco is another symbiotic nova where the radio light curve shows several radio peaks with the first one recorded on day 25 (Linford et al., 2017). The spectral evolution of V1535 Sco is also consistent with a mixture of thermal and non-thermal emission (Linford et al., 2017).

V3890 Sgr is the first symbiotic recurrent nova where the second radio bump is clearly dominated by non-thermal emission (see §3.3.1). During the decay phase of the radio light curve of V3890 Sgr, the flux densities can be described by a power law relationship with time such that $S_\nu \propto t^\beta$. Around day 17, the radio emission steepens such that $\beta = -0.5$ which changes to $\beta = -2.8$ from day 60, a steeper decay compared to that observed in SNe (Chevalier & Fransson, 2006).

So what might explain the second radio peak and the fast decay of V3890 Sgr? The luminosity remaining brighter compared to the model translates to either an increase in the velocity of the shock wave or an increase in the density of material being shocked, as established in the helium nova V445 Pup for example (see chapter 2). In estimating the radio luminosity of V3890 Sgr, the density distribution is assumed to decrease as r^{-2}. However, it has been shown that the surrounding medium in systems such as V3890 Sgr is not uniformly distributed. Simulations of interacting components in a binary system show the structure

of circumstellar material. Evidence shows that material from the companion star is concentrated in the equatorial plane during the mass transfer process (Walder et al., 2008).

Chandra High Energy Transmission Grating observations of V3890 Sgr on day 7 showed X-ray emission lines that are asymmetric, blue-shifted and indicating different plasma temperatures (Orio et al., 2020). Orio et al. suggest that a non-uniform distribution of the circumbinary medium could be the source of the different emission region temperatures. An interaction of a nova shock with dense, non-uniformly distributed material will increase the radio luminosity, and less dense material will decrease the radio emission observed. A faster decay seen in the radio light curve of V3890 Sgr on day 59.7 is estimated to occur at a radius of $1-2 \times 10^{15}$ cm considering the radius profile explained in §3.3.3.3.

This could imply a steeper fall in the density of the circumstellar material with radius (see Equation 2.3) as compared to the assumed r^{-2} in the model used to predict radio fluxes of V3890 Sgr. Similar low density material at $\approx 10^{15}$ cm is implied in another symbiotic nova V407 Cyg (Chomiuk et al., 2012). A non-uniform distribution of material may arise due to changes in the mass-loss rate from the companion star or the velocity in which the material is travelling in. Another possibility could be that the pre-existing material is swept up by ejected nova envelope from the previous eruption to created regions of less dense material. This concept has been investigated in the nova M31N 2008-12a by Darnley et al. (2019).

3.3.5 V3890 Sgr as a progenitor of SNe Ia

The estimated low ejecta mass for the nova envelope in the range of 10^{-7}–10^{-6} $M_\odot$ and the short recurrence time of 28 years, implies that the binary hosts a massive white dwarf ($\gtrsim 1.2$ $M_\odot$, Yaron et al., 2005). Non-detections of radio emission from SNe Ia have provided an opportunity to rule out some progenitor systems (see §1.2.6) through direct comparison of radio models and radio luminosity upper limits. Some progenitors in the single degenerate channel have been ruled out as candidates of SNe Ia while others remain valid candidates. This is due to the fact that these studies are primarily based on observations of individually classified SNe Ia even though the progenitors may be quite diverse (Foley et al., 2012; Chomiuk et al., 2016; Lundqvist et al., 2020; Cendes et al., 2020).

For example, a symbiotic progenitor with accretion rates $> 10^{-7}$ $M_\odot$ yr^{-1} has conclusively been ruled out for SN Ia 2019ein (Pellegrino et al., 2020). However, the upper limits placed on the mass-loss rate of the progenitor are not sufficient to rule out novae that undergo recurrent thermonuclear eruptions

(Pellegrino et al., 2020). In general, the current favoured systems for SNe Ia have a narrow mass-loss rate of $(10^{-9} \leq \dot{M} \leq 10^{-7})$ $M_{\odot}$ yr^{-1} depending on the velocity of the wind near the white dwarf (Chomiuk et al., 2012; Lundqvist et al., 2020). This is consistent with the mass loss rate estimated for V3890 Sgr.

A small number of SNe have shown the presence of Hα emission lines and Na I D absorption lines, which have been interpreted as the presence of circumstellar material around them (e.g., Patat et al., 2007). A similar evolution of variable Na I D absorption features for RS Oph is presented by Patat et al. (2011). The circumstellar material around SN Ia PTF 11kx is also shown to be structured such that regions of less dense material alternate with those of higher density material, commonly referred to as cavities and shells, respectively (Dilday et al., 2012). Based on the complex surrounding medium of recurrent symbiotic novae (Walder et al., 2008; Booth et al., 2016), it is possible that a certain percentage of these systems are potential progenitors of SNe Ia. The estimated mass-loss rate and possible structural distribution of the circumbinary material as determined from the radio light curve presented here, cannot rule out V3890 Sgr as a type Ia progenitor.

3.4 Conclusion

The symbiotic recurrent nova V3890 Sgr was observed for ~ 9 months with MeerKAT, at an observing frequency of 1.28 GHz, following the most recent eruption in 2019 (Figure 3.3). The radio emission is detected 6 days after the optical discovery and peaks on day 15. The rapid time evolution of the radio light curve, steep spectral indices (Table 3.3) and high brightness temperatures (Figure 3.7) are indicators of synchrotron radiation from the nova, similar to what is observed in other symbiotic recurrent novae (see §1.3.2.1).

The source of synchrotron emission in V3890 Sgr can be explained in terms of interaction between the ejected nova envelope and a structured circumbinary medium formed by the pre-existing wind from the red giant star. The radio light curve is characterised by a secondary peak following the initial peak at $\tau = 1$, and then decays faster than the expected decay for a shock wave propagating in a windlike medium (Figure 3.11). This hints at a complex structure of circumstellar medium around the nova. This could be similar to other novae where the eruption occurs inside a red giant wind such as RS Oph.

The turn-on of the radio emission fits well with a model of decreasing opacity of the ionized circumstellar gas as the shock wave sweeps through it (Chevalier, 1981). Modelling of radio emission

provides a mass-loss rate of the red giant companion star on the order of $\dot{M} = 1.8 - 4.0 \times 10^{-8}$ $M_{\odot}$ yr^{-1} for $v_{wind} = 10$ km s^{-1} and a distance of 7 kpc. Similar mass-loss rates are estimated for RS Oph (Van Loon, 2008).

CHAPTER 4

THE RADIO EMISSION OF CLASSICAL NOVA V339 DEL

Abstract

The radio observations of V339 Delphini obtained using the Karl G. Jansky Very Large Array and the Arcminute Microkelvin Imager Large Array (AMI) following the 2013 eruption are presented. The AMI data were obtained every two days resulting in the most detailed radio light curve of a classical nova known to date. The radio data are used to test the hypothesis that the observations were due to a bipolar shaped ejecta as suggested from emission line modelling at optical wavelengths. Here, the morphology is utilised in predicting the ejected mass of V339 Del during the eruption. The radio light curve is modelled in the morpho-kinematical program SHAPE using a linearly expanding ionized ejecta, assuming that the nova emission is dominated by thermal free-free emission. Considering a bipolar geometry for the nova ejecta, the radio light curve fluxes can be replicated using an ejected mass of $M_{\rm ej} \approx 0.1 - 8 \times 10^{-5}$ $\mathrm{M}_{\odot}$. The mass estimate of the ejecta compares well with estimates of emission line modelling in optical spectroscopy and also γ-ray emission modelling. High resolution radio images of V339 Del obtained with the VLA's A configuration initially show a spherical structure when the ejecta is optically thick and later a ring structure when the ejecta is optically thin. The change in optical depth and apparent morphology is a further indication of a non-spherical geometry. V339 Del shows evidence of shock powered emission in the first 100 days after the nova eruption.

4.1 Discovery and multiwavelength observations

The classical nova V339 Del was discovered on 2013 August 14.6 UT (MJD 56519.08) as a bright optical source of magnitude $V \approx 6.8$ (Nakano et al., 2013). The day of eruption (t_0) is taken as 2013 August 13.8, MJD 56518.3 (Schaefer et al., 2014; Gehrz et al., 2015). Extensive observations across all wavelengths,

including radio, near-infrared, optical, X-ray, and gamma-rays, were carried out following the discovery. Presented here is a summary of the multi-wavelength observations, and relevant interpretations are discussed to show how the observational evidence over months/years has led to our current understanding of the system.

A detailed optical light curve is shown in Skopal (2019), showing different evolutionary stages of V339 Del's eruption using optical magnitudes obtained from the AAVSO International Database (Kafka, 2020). At 1.8 days after discovery, the nova reached a maximum magnitude of $V \approx 4.5$ (Munari et al., 2013). The time taken by V339 Del to decline by 3 mag (t_3) was determined as 23 days, and therefore it is classified as a fast nova (see Table 1.1). Dust was also detected from the nova approximately a month after optical discovery (Gehrz et al., 2015; Skopal, 2019). Between day 2 to day 11 after t_0, V339 Del was detected as a γ-ray source emitting at energies greater than 100 MeV with the *Fermi-LAT* telescope (Hays et al., 2013; Ackermann et al., 2014). V339 Del therefore belongs to the class of novae that emit at such high energies.

A detailed discussion on γ-ray novae is given in §1.2.3.4. The first classical nova to be detected at GeV energies was V959 Mon. The intensive multi-wavelength observations of V959 Mon following its discovery provided clues as to how particles are efficiently accelerated to emit non-thermal emission. Using high resolution radio imaging, Chomiuk et al. (2014) pinpointed the origin of non-thermal emission as the shock interaction between a slow outflow and a fast wind. In V959 Mon, the particles are accelerated to high energies internally within the nova ejecta, as the white dwarf continuously loses mass in distinct phases, such that the faster polar outflows catch up with slower equatorial outflows and interact to form shocked regions (Chomiuk et al., 2014). While it is not clear that V959 Mon's morphology is universal across novae, it is clear that shocks in these systems are due to some form of interaction of a fast wind catching up with slow moving material (e.g., Aydi et al., 2020). γ-ray emission from novae is consistently observed during the early phase ($\approx$ weeks) following a nova eruption (Ackermann et al., 2014). This emission is expected to be accompanied by radio non-thermal emission (Vlasov et al., 2016).

Bipolar structure may form as a result of slow dense material that is concentrated in the equatorial region of the binary and a fast wind that escapes from the less dense polar regions of the binary system (Lloyd et al., 1997). This structure is supported by various approaches analysing multi-wavelength data of novae, such as spectral line modelling, analysis of high resolution near-IR images and high resolution radio imaging (Woudt et al., 2009; Chesneau et al., 2012; Ribeiro et al., 2013; Chomiuk et al., 2014; Linford

et al., 2015). The slow outflow will be shaped by the orbit of the binary system, while the fast wind is driven by residual nuclear burning on the surface of the white dwarf.

During the first days after the optical discovery of V339 Del, Schaefer et al. (2014) studied the nova at near-infrared wavelengths using the CHARA array. Within the first forty days after discovery, the emission was partially optically thick at optical/IR wavelengths, making it possible to measure the expansion rate and determine the spatial distribution of the outer nova ejecta. The resolved images are symmetric, showing an expanding ejecta with an optically thick core at the centre and an optically thin envelope (Schaefer et al., 2014). A similar structure is identified based on the analysis of spectro-polarimetric observations early on in the eruption using VESPolA on the Araki telescope ($t - t_0 \approx 1$ day; Kawakita et al., 2019). This is consistent with optically thick material close to the binary system and transparent ejecta further away from the system. Later in the evolution, during the nebular phase around ≈ 1 year after discovery, Hα emission line profile modelling required a significant amount of mass at the equatorial region of the binary system compared to that hosted in the polar regions in order to replicate the observed features (Tarasova & Skopal, 2016).

Combining the expansion rate of resolved near-infrared images and the velocities obtained from optical emission lines, Schaefer et al. (2014) obtained a distance of 4.5 ± 0.6 kpc to the nova. Estimating the expansion rate of the nova from photometry during the early days of the evolution, Gehrz et al. (2015) determined a distance of 4.5 ± 0.8 kpc to V339 Del assuming the velocity representing that of an expanding envelope. The estimated distance of V339 Del using *Gaia* is between 1.7 to 4.4 kpc (Schaefer, 2018). A distance of 4.5 kpc is adopted for models of radio emission developed in this work.

In this chapter, radio light curves and high resolution radio imaging of V339 Del are presented. The radio emission from novae in the 1970's was well described as thermal emission from an ionized expanding nova envelope (Seaquist & Palimaka, 1977; Hjellming et al., 1979). Radio light curves of previously monitored novae demonstrate that the radio emission emerges days to weeks following the discovery in the optical wavelengths and is observed for years. Initially, the radio flux rises and brightens at all frequencies, due to an increase in the surface area of an optically thick expanding nova remnant. The flux density depends on degenerate parameters, including distance, temperature of the nova envelope, the maximum expansion velocity and the mass of the ejected material (Hjellming et al., 1979). The morphology and density distribution of the envelope also affect the radio light curve.

As the envelope expands with time, the material becomes less dense and the $\tau = 1$ radio photosphere recedes (at a given frequency, the radio emission originates from the surface of the emitting region at $\tau = 1$). It requires more ionized material (i.e., emission measure) to reach $\tau = 1$ at higher frequencies, so the transition to the optically thin phase begins first at higher frequencies and later at lower frequencies (e.g., Seaquist et al., 1980). The final evolution of the radio emission with time is the decrease in flux density when the ejected material is entirely optically thin, and continues to drop in density.

By assuming a particular density profile of the bulk of the nova envelope, some key parameters of the nova eruption can be estimated, including the mass of the ejected material and its kinetic energy. The standard Hubble flow model, where the outflow is homologous such that the innermost material is moving slower that the outermost material and the ejecta velocity (V) is proportional to radius (R), has been used extensively to describe radio light curves of novae. Therefore, the material is distributed between the maximum and minimum ejecta velocity, and the ratio of these two values of velocity is another factor in radio emission models (Hjellming et al., 1979).

However, other considerations in fitting radio light curves of novae include the variable wind and unified models (Seaquist & Bode, 2008). The differences in the models lie in their treatment of the inner boundary of the ejecta, which determines when the radio light curve becomes optically thin (Seaquist & Bode, 2008). The electron temperature during the optically thick phase is taken as a constant of $\sim 10^4$ K based on theoretical photoionization models where the ejecta are heated by a hot white dwarf undergoing residual hydrogen burning (Cunningham et al., 2015). The mass distribution within the finite shell can be described with a density profile that falls as $\rho \propto r^{-p}$ where $p = 2$ or 3 and both profiles produce reasonably similar predicted light curves (Seaquist et al., 1980).

Most nova envelopes are aspherical, as observed from emission line profiles in spectroscopy and spatially resolved nova remnants at optical and radio wavelengths. Most recent models have considered bipolar outflows. Ribeiro et al. (2014) showed that applying spherical radio models to novae which exhibit bipolar outflows results in an overestimation of the ejected mass by at least a factor of two. In addition, the spherical radio models show a relatively sharp peak before the final decay, while bipolar models will show a flatter, more gradual evolution. The time of almost constant flux depends on the mass distribution at the different regions of the nova envelope (Ribeiro et al., 2014).

Here the observations of V339 Del following the 2013 August outburst, obtained with the upgraded

Karl G. Jansky Very Large Array (VLA) and the Arcminute Microkelvin Imager Large Array (AMI) at cm wavelengths, and the Combined Array for Research in Millimeter-wave Astronomy CARMA at mm wavelengths, are analyzed. The observations are presented in §4.2. The radio light curves, spectral evolution and resolved images are presented in §4.3. The mass of the ejected material is estimated by replicating the light curves in SHAPE[1] version 5 (Steffen et al., 2011) and is presented in §4.4.

4.2 Observations and data analysis

The radio observations of V339 Del started two days after optical discovery. The observations were obtained over a broad range of frequencies between 1.2 GHz and 230.4 GHz.

4.2.1 VLA Data

Radio observations of V339 Del were obtained between 2013 August 16 and 2017 July 08 through the following VLA programs: 13A-455, 13B-057, S61420, 15B-343, 16A-258, 16B-330, 17A-335. The data were obtained in all array configurations and in VLA receiver bands L (1 – 2 GHz), C (4 – 8 GHz), Ku (12 – 18 GHz), and Ka (26.5 – 40 GHz). The details of the observations are given in Appendix B. The observing log is listed in Table B.1. The sources J1407+2827, J2021+2318 and J2033+2146 were used for gain calibration at different VLA configurations and observing frequencies. Bandpass and absolute flux density calibration for each run were done using 3C286. The observations were edited and reduced with standard procedures in `AIPS` and `CASA`.

Imaging was carried out primarily in `difmap`, weighting the data with a Briggs robust value of 1. For most of the observations, an iteration of phase-only self calibration was carried out, with a solution interval of 1 – 8 minutes. To obtain the flux density of V339 Del, a Gaussian was fit to the source in each image with the tasks `JMFIT` in `AIPS` and `imfit` in `CASA`. The width of the Gaussian was set equal to that of the synthesized beam, except when the VLA is in A configuration. If no radio emission was detected at the location of V339 Del, an upper limit on the flux density is determined as three times the image rms plus the value of the pixel at the target location. The final estimate of uncertainty was obtained by adding in quadrature (Equation 3.1), the uncertainty from the Gaussian fit and calibration errors of 5% at lower frequencies (< 10 GHz) and 10% at higher frequencies (> 10 GHz). The resulting flux densities and uncertainties are presented in Table B.1.

[1] http://bufadora.astrosen.unam.mx/shape/

4.2.2 CARMA Data

V339 Del was monitored with CARMA under the programme c1130 at 96 and 230 GHz between 2013 August 16 and 2014 March 26. The CARMA telescope was a millimeter interferometer located at the Owens Valley Radio Observatory in the US and comprised twenty three dishes with different diameters between 3.5-m and 10.4-m (Bock et al., 2006). The telescope ceased to operate in 2015. The data were reduced with standard procedures in `MIRIAD`. The measurements are presented in Table B.1. The quoted values of uncertainties include 10% calibration errors (see Equation 3.1).

4.2.3 AMI Data

The AMI performed high cadence monitoring of V339 Del, beginning 12 days following its discovery. AMI is a radio interferometer based near Cambridge in the UK, comprising of eight 12.8–m dishes in diameter that have a baseline range of 18 to 110 m and measure a single polarisation (Zwart et al., 2008). A total of 166 observations were obtained between 2013 August 26 and 2015 July 19. For each epoch, exposure times of one hour were used, which all took place pre-dating the correlator upgrade at the end of 2015 (Hickish et al., 2018). The observations therefore have a central frequency of 15.7 GHz and an effective bandwidth of 3.6 GHz. Initially the observations were obtained every 2 or 3 days until 2014 October 01 after which the cadence was dropped to once a week. The observations resulted in the highest cadence done for a classical nova, and consequently the most detailed radio light curve of any classical nova to date.

The AMI data were reduced using the fully automated pipeline `AMIsurvey` (Staley & Anderson, 2015), which utilises Python libraries that were built on the `AMI-REDUCE` software package (Dickinson et al., 2004). The pipeline performs flagging, calibration, and Fourier transforms of the AMI data. Imaging was performed with `CHIMENEA`, which is an imaging tool built on `CASA` and algorithms developed for the LOFAR Transient Key Science Project[2]. The imaging tool is specifically designed to clean and image multi-epoch radio observations of transients (Staley & Anderson, 2015). For more extensive details on the reduction process employed on this dataset see Anderson et al. (2018). Flux density errors of V339 Del (including upper limits for non-detections) presented in Table B.2 were measured using the LOFAR Transient Pipeline (TRAP; Swinbank et al., 2015). The errors include a 5% absolute flux calibration error appropriate for AMI data (Perrott et al., 2013).

[2]https://tkp.readthedocs.io/en/release2.0/;https://github.com/transientskp/tkp

4.3 Results

4.3.1 The radio light curve

The multi-band radio fluxes and light curves are presented in Table B.1 and B.2, and Figure 4.1. Due to drifts in central observing frequencies, some of the light curves include a combination of different central frequencies. For example 28.2 GHz and 29.5 GHz are plotted as one radio light curve. V339 Del was not detected at radio wavelengths between 1.3 GHz and 96.7 GHz in the early observations, on day 2 (with the VLA and CARMA) and day 14 (with GMRT; Roy et al., 2013; Chomiuk et al., 2013a). The first detection is on day 24.8, when the radio emission from V339 Del was detected with the VLA at 28 – 36 GHz with a flux density of 0.2 mJy. On day 44, it was detected at lower frequencies (~ 16 GHz) with a flux density of ~ 0.5 mJy. During this time, non-detections were recorded at lower frequencies (≤ 7.4 GHz; Chomiuk et al., 2013b). The first detection with AMI was on day 46.6, when V339 Del was detected at 15.7 GHz at 0.64 ± 0.13 mJy (Anderson et al., 2013).

V339 Del subsequently brightened at all frequencies, reaching a maximum of 126 ± 39 mJy at 230 GHz on day 54.6. The radio light curve shows two peaks, at day 100 and day 600, at frequencies 4 – 8 GHz (see Figure 4.1). At frequencies > 13 GHz the radio emission rises steadily up to day 100 followed by a plateau that lasts up to day 300. The radio emission is detected for more than 1000 days, behaviour similar to other novae studied at radio frequencies (Seaquist & Bode, 2008). The last observation of the nova with the VLA is on day 1424 when the flux density at 35 GHz had declined to 0.33 ± 0.05 mJy.

Considering the AMI light curve shown in Figure 4.2, the very well sampled radio light curve provides an opportunity to observe if there are any rapid changes in the flux densities of the target. In general, the radio light curve is characterised by dips throughout its evolution unlike the expected smooth rise, peak and decay observed in other novae (e.g, Hjellming, 1996; Seaquist & Bode, 2008; Wendeln et al., 2017).

4.3.2 Radio spectral evolution of V339 Del

The evolution of V339 Del's radio spectrum is presented in Figure 4.3 and 4.4. The simplest fit is a single power law which yields a spectral index, α, defined as $S_\nu \propto \nu^\alpha$, where S_ν is the flux density and ν is the observing frequency. The flux densities during the initial days, between day 43 and 300 after eruption, are fitted with a single power law with spectral index in the range $1.4 \leq \alpha \leq 1.6$, an indication of optically thick radio emission. For an optically thick ionized gas, the spectral index is theoretically expected to be $\alpha = 2.0$

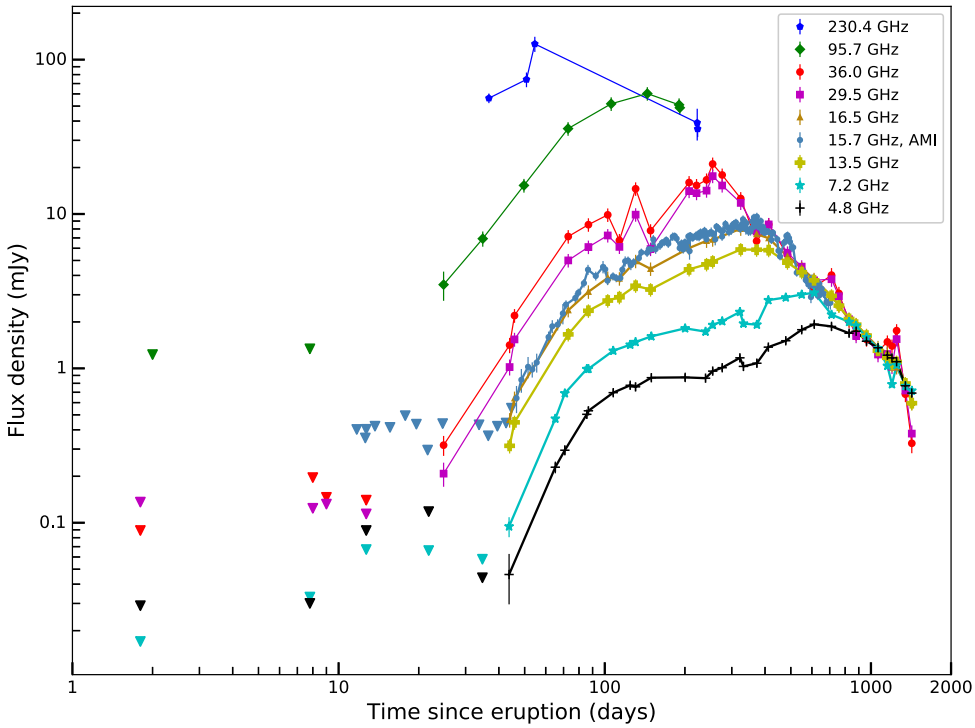

Figure 4.1: The radio light curve of V339 Del showing observations with the VLA from 4.8 GHz to 36 GHz, CARMA at 96 GHz and 230 GHz, and AMI at 15.7 GHz.

(e.g., see §6.2 in Pacholczyk, 1970). However, no nova to date has been observed to reach the theoretical value, with most showing $\alpha \approx 1.5$ during the optically thick phase (e.g., Krauss et al., 2011; Wendeln et al., 2017). Therefore, the early radio spectrum of V339 Del is consistent with that of other optically thick nova ejecta.

Later in the evolution on day 549 and 711, the spectra require a broken power law to be well fit, such that the higher frequencies (> 10 GHz) have a shallower power law ($\alpha \leq 0.4$) compared to that of lower frequencies (< 10 GHz) with $\alpha \approx 1$ (see Figure 4.4). The turnover is indicative of a receding photosphere at higher frequencies, where the higher frequency photosphere is smaller than that at lower frequencies. The spectral index during the decay phase of the light curve gradually declines even at lower frequencies from $\alpha = 0.24$ on day 1153 to $\alpha = -0.04$ on day 1347. Throughout the nova evolution, the spectra approach - but do not reach - the theoretically expected value of optically thin free-free emission of $\alpha = -0.1$ (e.g., see §6.2 of Pacholczyk, 1970).

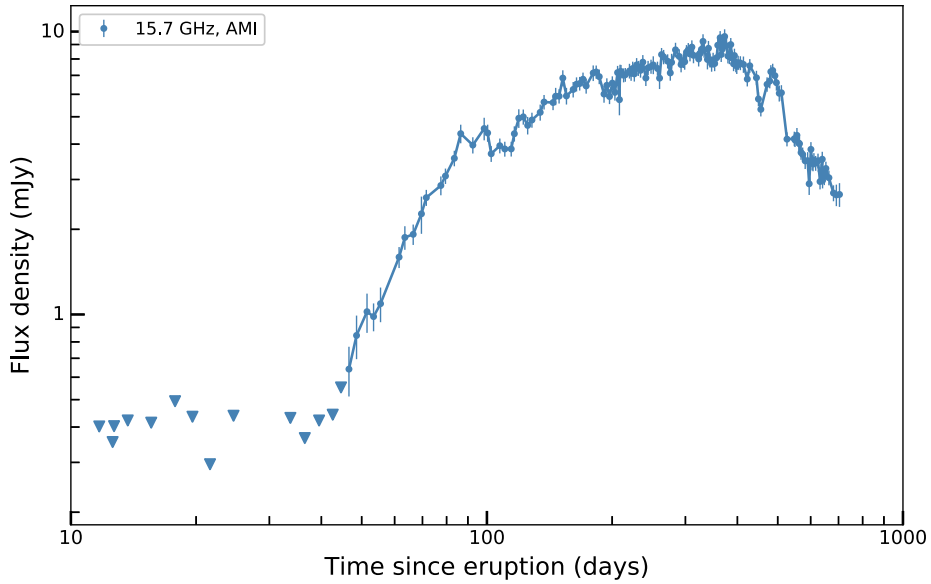

Figure 4.2: The radio light curve of V339 Del with AMI at 15.7 GHz showing dips of fluxes throughout the nova evolution.

4.3.3 High resolution images of V339 Del

Resolved radio images provide crucial hints to the nature of nova ejecta including their morphology (i.e., spherical, ellipsoidal, bipolar) and the presence of jets (e.g., Taylor et al., 1988; Hjellming, 1996; Linford et al., 2015; Sokoloski et al., 2008). VLA A-configuration observations of V339 Del were obtained between 2014 March 02 and 2017 January 13, during three VLA A configuration phases that spanned 3 – 4 months each with 12 months in between while the VLA was in more compact configurations (see Table B.1). Here, resolved radio images of the nova at Ku and Ka bands are considered. The VLA in A configuration at these frequency bands provides a synthesized beam in the range FWHM $\approx 0.065'' - 0.15''$.

The resolved images of the ejecta are shown in Figures 4.5 and 4.6. The resolved images around day 221 show an optically thick ejecta with a spherically symmetric structure in the Ka band (see Figure 4.6). A similar structure is observed from near-IR spatially resolved images (Schaefer et al., 2014). The deconvolved images provide an estimation of the size but cannot describe the structure in detail. A detailed description of the structure requires modelling the target in the uv plane. Around day 758, the images at

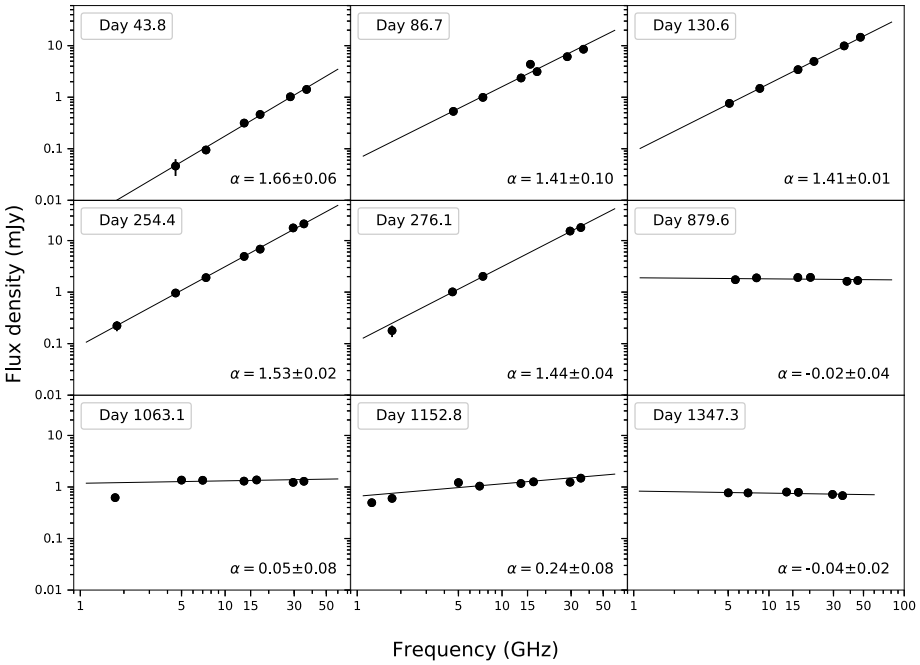

Figure 4.3: A sample of VLA and AMI spectra of V339 Del of its evolution. In most epochs the data are fitted with a single power-law and the spectral index is indicated in the bottom-right corner.

the Ka band can be described by a circular shaped shell with a central cavity reminiscent of a disc or a ring. The ring structure shows non-uniform distribution of intensity (see Figure 4.6). The images remain relatively circular shaped at the Ku band throughout the observations with VLA A configuration (see Figure 4.5).

A spherical structure at early times and a ring structure at late times implies possibilities of a symmetric outflow or a torus that constrains a bipolar outflow viewed pole on. These geometries have also been implied following spectroscopic and spectropolarimetric analyses of emission lines (Shore et al., 2016; Tarasova & Skopal, 2016; Kawakita et al., 2019).

During the early times, to about day 221, the ejecta are optically thick based on the spectral index at this time. The brightness temperature is estimated using the relation between angular size θ_a, θ_b (the diameters of the major and minor axis, respectively) and flux density S_ν (Equation 2.2). The angular size is estimated by fitting a Gaussian to the image using the `imfit` task in CASA. If the width of the Gaussian is left to vary when the nova was thought to be resolved i.e., at VLA A configuration and high frequencies, the

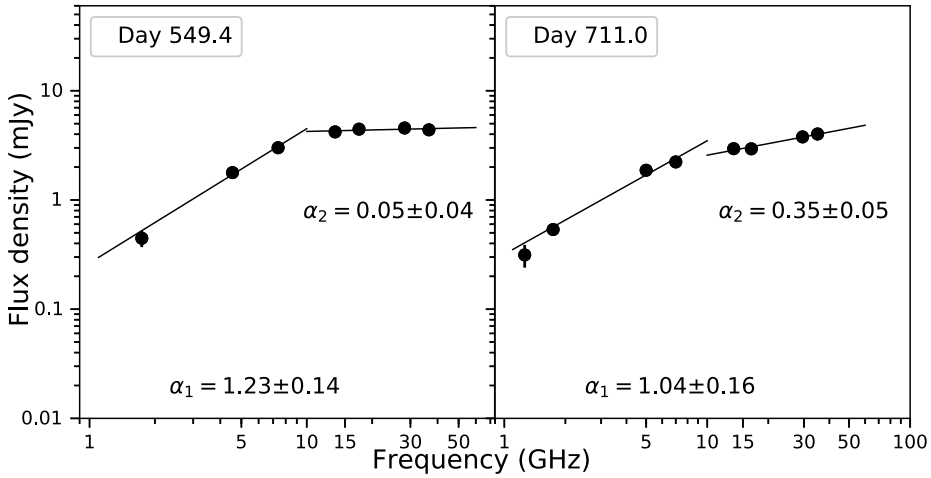

Figure 4.4: A sample of VLA and AMI spectra of V339 Del which are fitted with a broken power law. In this case, two values of spectral indices which represent lower and high frequency fits are quoted as α_1 and α_2 respectively.

angular size is determined by the gaussian width deconvolved by the synthesized beam. Using the image sizes, the brightness temperature is estimated as a few $\times$ 10^4 K consistent with theoretical predictions (e.g., Cunningham et al., 2015). Previously, the temperature of the ejecta has also been determined to be a few $\times$ 10^4 K based on resolved radio images of other novae (Taylor et al., 1988; Hjellming, 1996).

4.4 Discussion

4.4.1 Modelling the radio light curves of V339 Del

The increase in flux density before the first 100 days can be described by $S_\nu \propto t^{3.0}$ starting on day $t = 0$ at observing frequency 4.8 GHz. The standard Hubble flow model assumes linear expansion of a spherical shell from day $t = 0$, such that $S_\nu \propto t^\beta$, where $-3 \leq \beta \leq 2$ throughout the radio light curve evolution at the different phases. Initially, the flux density increases as the emitting region grows, as the radio photosphere coincides with the outermost regions of the expanding nova ejecta. The flux density scales as $S_\nu \propto \nu^2 t^2$ (Hjellming et al., 1979; Ribeiro et al., 2014) if the ejecta are emitting thermal emission. The steep rise in the radio flux observed in V339 Del has been observed in other novae such as QU Vul (Taylor et al., 1987), V1723 Aql (see Figure 1.16; Krauss et al., 2011), V5589 Sgr (Weston et al., 2016b), and V1324 Sco (Finzell et al., 2018). The early time radio peaks are characterised by high brightness temperatures on

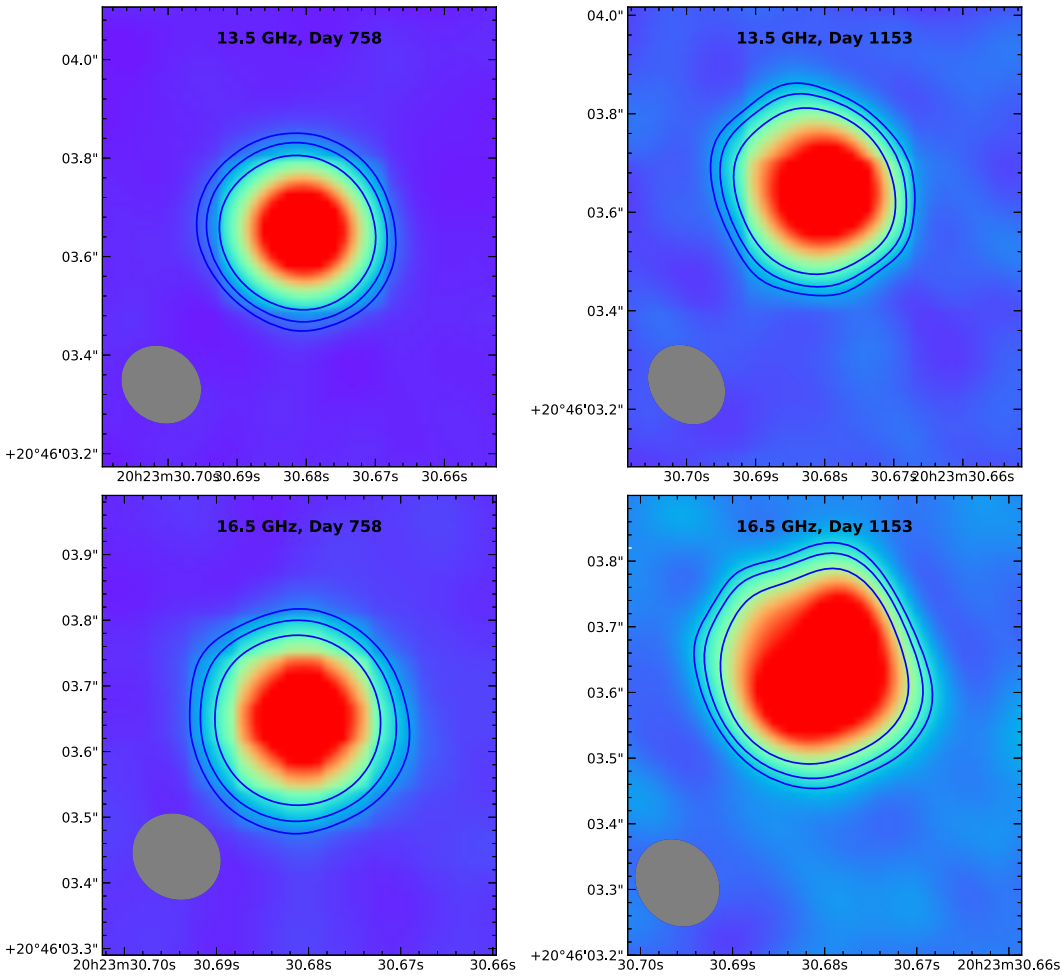

Figure 4.5: Ku band images of V339 Del over the course of 2015 to 2017 during the VLA A configuration. The upper panels show the maps of 13.5 GHz and the lower panels show the maps of 16.5 GHz. Shown at the bottom of each image in ellipse is the synthesized beam. The contour levels are 3, 5, 9 mJy/beam in all the images.

the order of $\sim 10^5$ K, which cannot be explained to originate from ionized ejecta being heated by the hot white dwarf which is expected to result in maximum temperatures of a few times 10^4 K (Cunningham et al., 2015). Shown in Figure 4.7 is the brightness temperature of V339 Del at a distance of 4.5 kpc. This was determined using the angular size expansion of the nova shell determined by Schaefer et al. (2014), based on resolving the ejecta very early on (within days of t_0) using the CHARA near-IR interferometer. During the early times, before day 100, the values of the brightness temperatures are of the order of $> 10^5$ K.

The early high brightness temperature bumps in novae are thought to originate from either shock-

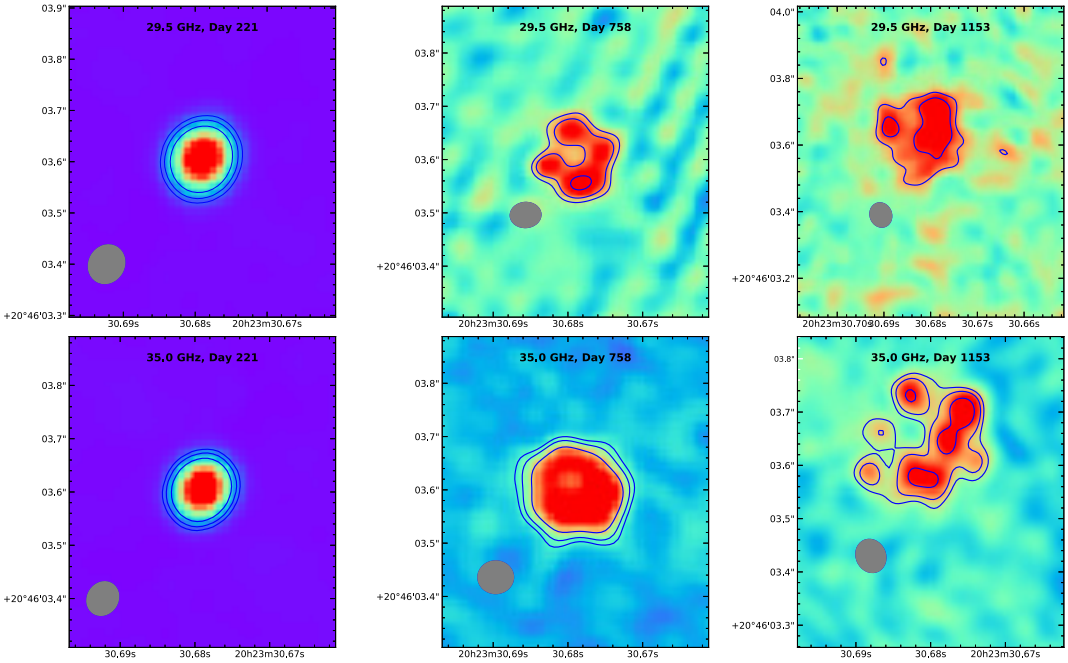

Figure 4.6: Ka band images of V339 Del over the course of 2014 to 2017 during the VLA A configuration. The upper panels show the maps of 29.5 GHz and the lower panels show the maps of 35.0 GHz. Shown at the bottom of each image in ellipse is the synthesized beam. The contour levels are 3, 5, 9 mJy/beam in all the images.

heated thermal gas or shock-powered non-thermal emission (Metzger et al., 2014; Vlasov et al., 2016). For the radio peak to be produced by hot thermal gas, based on theoretical models by Metzger et al. (2014), the shell of gas should also be dense in addition to the high temperatures. These two characteristics provide ideal environments for the production of hard X-ray emission. V339 Del was observed as an X-ray source in the 1–10 keV energy range using the X-ray Telescope on the *Neil Gehrels Swift Observatory* during early times (< 200 days; Page et al., 2013; Gordon et al., 2020). Shocks in novae are also shown to originate from interactions of different components with different velocities within the ejected material (O'Brien et al., 1994). It is therefore possible that the source of the radio peak in V339 Del was due to shocks within the ejecta.

As the ejecta expand and drop in density, the radio emission is detected due to a decrease in the optical depth (τ; Equation 1.6). For nova ejecta described with a density distribution of $\rho \propto r^{-2}$, the standard radio evolution model predicts $S_\nu \propto t^{1.3}$ during the transition from optically thick to thin emission, around the peak of the radio light curve (Seaquist & Bode, 2008). The transition phase in the radio light curve of V339 Del, measured between day 100 and 700 at 4.8 GHz, is less steep than expected, as the flux scales as $S_\nu \propto t^{0.5}$. The transition also lasts for a longer time compared to that of a spherically symmetric ejecta

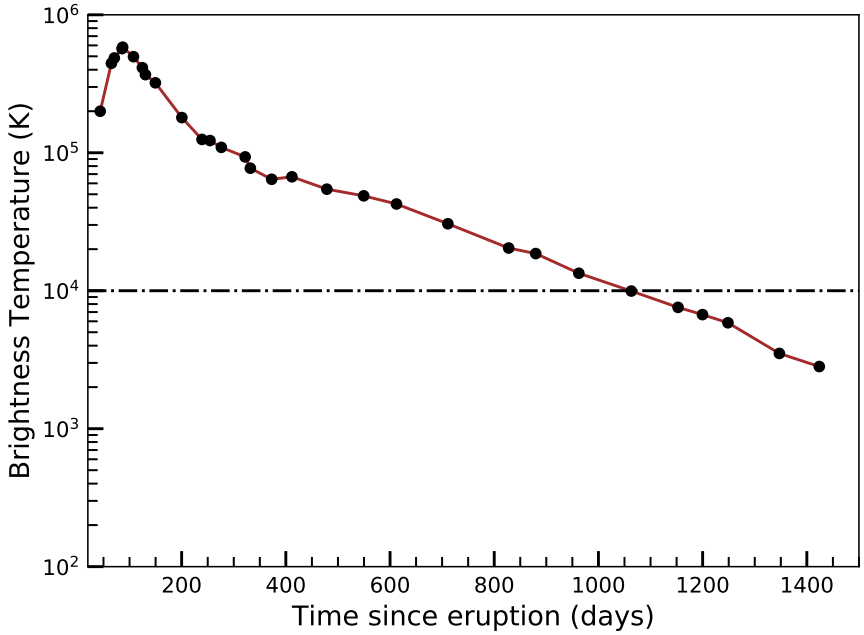

Figure 4.7: Brightness temperatures of 4.6 GHz emission of V339 Del estimated using the angular size expansion of the nova envelope determined by Schaefer et al. (2014).

possibly due to non-spherical morphology and the inclination of the nova envelope (Ribeiro et al., 2014). Simulated bipolar morphologies and resolved nova images show that material in the equatorial plane remains optically thick for longer periods (Heywood & O'Brien, 2007; Ribeiro et al., 2014; Linford et al., 2015). Consequently, the plateau indicates a balance between the less dense polar outflow becoming optically thin and the dense slow outflow contributing significantly to the radio emission. The time evolution during the decline phase for V339 Del is $S_\nu \propto t^{-1.6}$ at 4.8 GHz, which is also shallower than the steep decay, $S_\nu \propto t^{-3}$ predicted by standard radio models (Hjellming et al., 1979; Ribeiro et al., 2014).

Synchrotron emission from relativistic shocks as observed in SNe and SN remnants have spectral indices between -1 and -0.5 (Green et al., 2019). However, these range of spectral indices are not observed in novae early on in their evolution when shocks are thought to be present. Instead flat spectral indices, $\alpha < 1.0$, has been observed within days of optical discovery in other novae (Chomiuk et al., 2014; Finzell et al., 2018). This is due to presence of thermal ejecta which contributes to free-free absorption. However, the spectral indices of V339 Del at the initial phase of radio emission are consistent with optically thick emission (Figure 4.3). At this point it is difficult to differentiate between optically thick free-free or synchrotron emission absorbed by ionized gas. However, as discussed earlier in this chapter, V339 Del was discovered as a strong source of $\gamma-$ray emission (Ackermann et al., 2014). This emission is associated

with shock interactions in novae, which are also thought to be the origin of synchrotron emission in these binary systems (Vlasov et al., 2016). A non-detection of synchrotron emission with relatively flat spectral indices therefore could mean that the non-thermal emission of V339 Del was produced behind optically thick nova ejecta.

The evolution of the radio light curve of V339 Del is complex. As discussed above, there are signatures of shock emission and complex ejecta morphology. This implies the presence of more than one mechanism producing radio emission. The radio evolution of V339 Del at late stages ($\gtrsim$ 500 days) does not deviate from the standard model expected to be produced by a ionized remnant without shock interactions (Seaquist & Bode, 2008).

If thermal emission originates from an isothermal expanding shell, the maximum flux is expected at the radio photosphere's maximum physical size (Bode, 2002; O'Brien et al., 2015). The maximum flux density observed at 96 GHz on day 145 can be reproduced by assuming a distance of 4.5 kpc, a temperature of 12,000 K and ejecta mass of $\approx 8 \times 10^{-5}$ $M_{\odot}$. A more complex radio model requires a representation of the radial density profile and the three-dimensional morphology of the nova ejecta, as investigated in §4.4.2.

4.4.2 Modelling the radio light curves with SHAPE

The radio emission of V339 Del is modelled using a bipolar morphology in SHAPE, where an attempt is made to replicate the radio light curves and resolved radio images. SHAPE is a morphology and kinematics tool that is used to construct three-dimensional structures of astrophysical phenomena (Steffen et al., 2011).

To create models that can be compared with the observations, two things are key. These include the radiative transfer equations given in §1.3.1 and the geometry assumed for the nova ejecta. A bipolar structure is supported by high resolution VLA images that clearly show the slow dense flow dominating the late images, while the earlier images are dominated by the faster outflow (see §4.3.3). This geometry is also considered by many authors following the analysis of multi-wavelength data as discussed in §4.1. A bipolar morphology is therefore adopted to represent the nova outflows (see Figure 4.8 for a visual representation).

The input values of the ejecta expansion velocity and the inclination angle of the binary system are

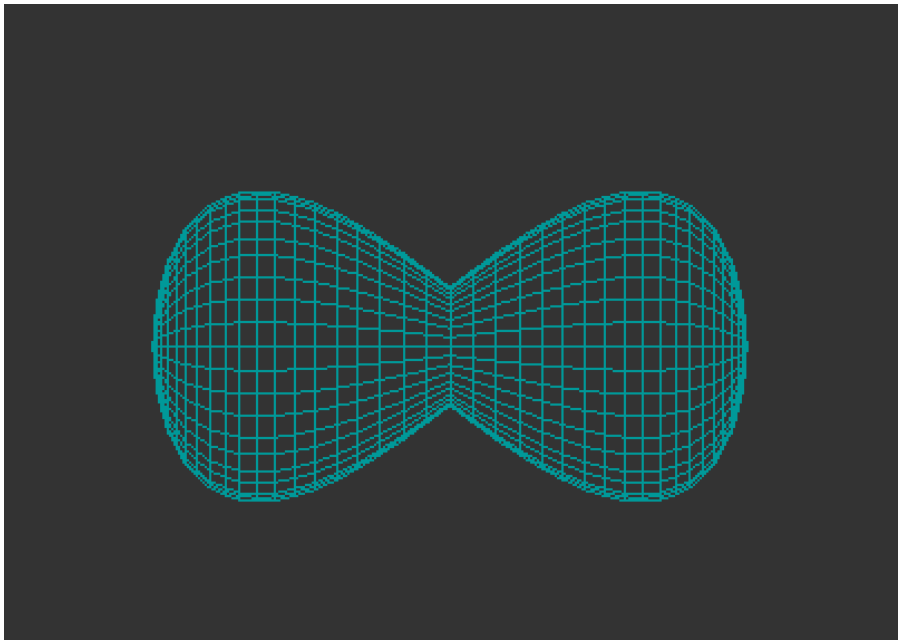

Figure 4.8: The structure representation of the nova ejecta used as input in SHAPE model.

those modelled by Shore et al. (2016) using Monte-Carlo radiative transfer techniques to reproduce the optical emission line profiles of V339 Del. The profiles are fit with a bipolar geometry, and lines widths are also fit to determine the velocity of the fastest ejecta. Shore et al. (2016) determined an inclination of 35° to 55° for V339 Del.

SHAPE consists of two major modules that are used to replicate emission lines and reproduce images of nova remnants for comparison with observations. These include the 3D module and the rendering module. The 3D module is used to set the basic structure of the remnant, such as a sphere or a torus with polar outflows. It also consists of modifiers such as *squeeze* that are used to change initial structures to more complex geometries. Other modifiers include velocity (Equation 4.1) and density. We take a linear proportionality between velocity and radius, such that $V \propto r$ which implies that the slow material is close to the compact object and vice versa.

$$V(r) = 2500(r/r_0) \text{ km s}^{-1} \tag{4.1}$$

where r is the radial distance and r_0 is the outer radius. The maximum velocity of the outflow is adopted as 2500 km s^{-1} (Shore et al., 2016). With an assumed shell thickness of 0.25 between the inner and outer radius, the minimum ejecta velocity can be estimated such that $V_{\text{min}} = 0.25V_{\text{max}} = 625$ km s^{-1}. This velocity range has been estimated using optical spectroscopy (Schaefer et al., 2014). The ratio between the

estimated minimum and maximum velocities of the expanding were used to set the shell thickness. This parameter was not varied in the SHAPE models.

Using the *squeeze* parameter in SHAPE, a bipolar morphology is created to consist of a major axis and a minor axis related by the equation

$$s = 1 - \frac{a}{b}$$

where a is the minor axis and b the major axis. Using the render module in SHAPE, the inclination of the binary system is set as 35° as the resolved radio images indicate a possible low inclination limit.

To estimate the flux, a ray of radiation is traced to the observer and is described by emission and absorption coefficients (see Equations 1.2 and 1.4) which depend on observing frequency, electron temperature and the density of the ejecta as explained in §1.3.1.1. The density is determined by the mass of the ejected envelope. For all the frequencies, the ejected range of masses estimated from spectroscopic observations is used to replicate the radio light curves using the standard model of thermal bremsstrahlung emission from an expanding ionized gas (Hjellming et al., 1979; Seaquist & Palimaka, 1977; Seaquist & Bode, 2008). The temperature of the warm photoionized gas is estimated from radio imaging as $T \approx 1.2 \times 10^4$ K (§4.3.3).

To determine a value of $M_{\rm ej}$, a maximum velocity ($V_{\rm max} = 2500$ km s^{-1}) and a distance to the nova ($d = 4.5$ kpc) are assumed and the radio emitting region is assumed to be between the inner and outer radius. The density is taken to vary as r^{-2}, although $\rho \propto r^{-3}$ has been successfully used to describe radio light curves of some novae (Seaquist et al., 1980). A filling factor of 1 was assumed. A model of an expanding thermal remnant is developed for frequencies between 4 GHz to 35 GHz as shown in Figure 4.9. The models are not done for lower frequencies (<1.75 GHz) and the observing frequencies of the CARMA telescope, as the intermediate frequencies are well sampled and have few non-detections. The first day when the ejecta started expanding is assumed to coincide with the thermonuclear eruption ($t = 0$).

Estimates of $M_{\rm ej}$ for V339 Del range between 10^{-5} M$_\odot$ to 10^{-4} M$_\odot$ (Shore et al., 2016; Tarasova & Skopal, 2016). Shown in Figure 4.9 and Figure 4.10 are models of the radio light curves using these mass estimates, respectively.

To compare the images from SHAPE to those of the observations, the same model utilised for the radio light curves was used. However, only resolved images were replicated, at 29.5 GHz. The higher ejecta mass of 10^{-4} M$_\odot$ was used together with the adopted values of distance, maximum ejecta velocity and

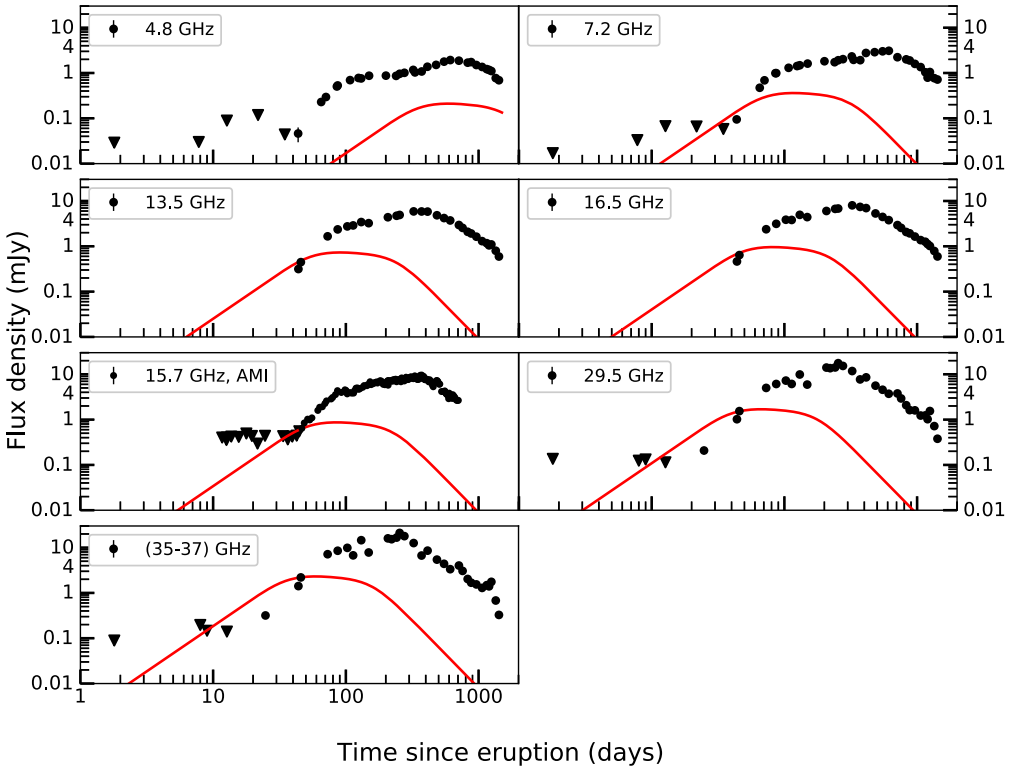

Figure 4.9: The observed radio data (black dots) at different frequencies and free expansion model (solid red line) in each frequency panel for the emission from the nova. The assumption is that the mass was ejected at $t_0 =$ 0 days after optical discovery. To replicate the data, a bipolar morphology of the ejecta and an inclination of 35° is assumed. Other adopted parameters include a distance to V339 Del (4.5 kpc), maximum expansion velocity of 2500 km s^{-1} and electron temperature of 12000 K. The ejected mass utilised to replicate the light curves is 10^{-5} $M_{\odot}$.

inclination of the binary system. In order to compare the model images and observation images, the models were convolved with the synthesized beam for the considered day and observing frequency. To create the residual images, the models were subtracted from the observed images. Figure 4.11 shows the images from the first VLA A configuration when the nova ejecta were optically thick. Figure 4.12 shows the images from the first VLA A configuration when the nova ejecta were optically thin.

The lower mass ejection model does not described the radio light curves at all the phases and under-predicts the flux density. The higher mass ejection model agrees reasonably well with the observed flux densities over a wide range of observing frequencies and time except for days > 600. This could be due to multiple components emitting free-free emission that has not been included in the model.

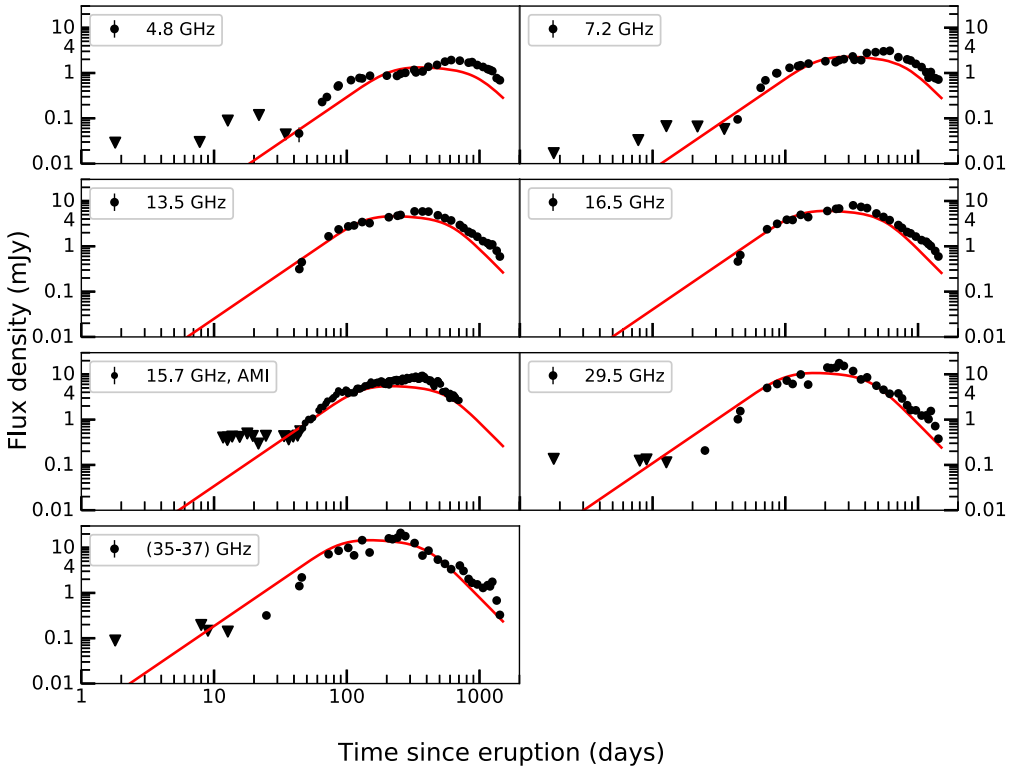

Figure 4.10: Same as Figure 4.9 but the ejected mass utilised to replicate the light curves is 10^{-4} $M_{\odot}$.

The high mass ejecta model overpredicts the flux density at high frequencies, > 15 GHz and underpredicts the flux density at lower frequencies during the optical thick phase of the radio light curve (see Figure 4.10). It is not suprising that the radio emission cannot be described by a free-free emission model with a simple morphology given the hints of non-thermal emission explained in §4.4.1. However, since the late time emission is consistent with thermal emission from an expanding nova remnant, a kinetic energy of the shell at a distance of 4.5 kpc with a range of velocities between a maximum and minimum velocity value is estimated as $\approx 10^{45}$ erg, typical of a classical nova.

The modelling applied for V339 Del radio light curves is that of a smooth distribution of mass in the nova remnant represented by a filling factor, $f = 1$. However, through modelling of optical emission line profiles, Shore et al., 2016 determined a filling factor, $f = 0.1$ for the nova. Such a filling factor means that the ejecta remain optically thick for a long time and increases the flux density during the transition

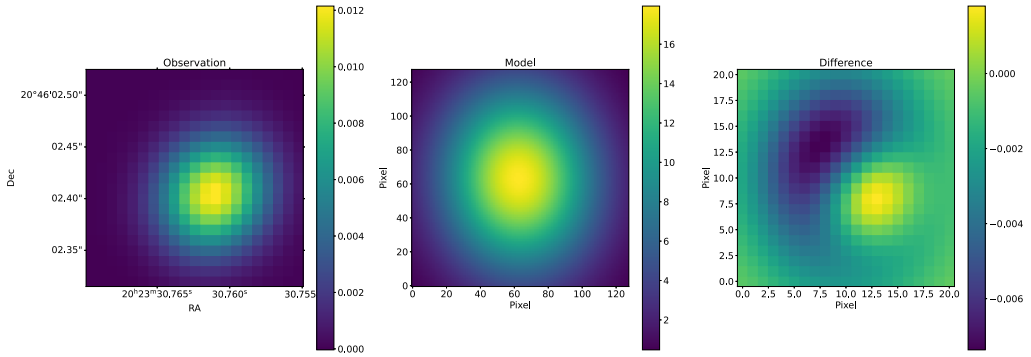

Figure 4.11: Comparisons between observations, model and the residual (observed−model) images from day 221 at 29.5 GHz. The SHAPE model assumed $M_{\rm ej} = 10^{-4}{\rm M}_{\odot}$.

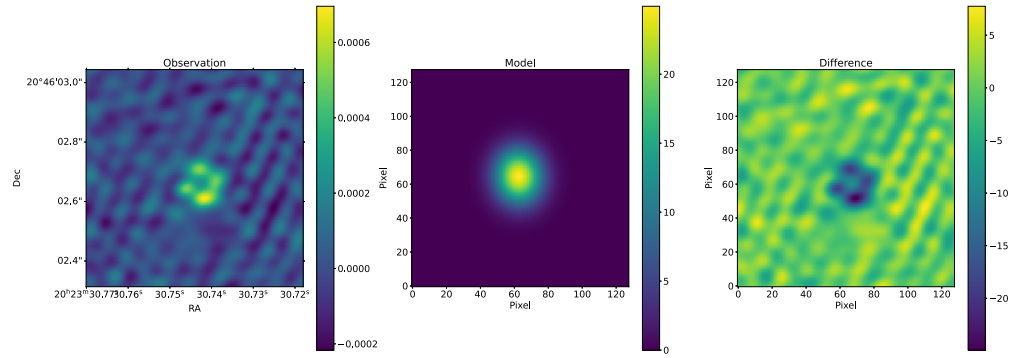

Figure 4.12: Same as Figure 4.11 but the image is for day 758.

phase of the radio light curve. The estimated ejecta mass in such a case will therefore decrease by a factor of $f^{0.5}$ (e.g., Finzell et al., 2018), such that adopting a value of 0.1 for the filling factors gives an estimate of 3×10^{-5} M$_{\odot}$ if the ejecta in V339 Del are clumpy. This is within the range of observational mass ejecta estimates for fast classical novae (Seaquist & Bode, 2008; Roy et al., 2012). Since a simple bipolar morphology and free-free emission are not fully descriptive of the emission from V339 Del, other factors as explained in §4.4.3 have to be considered.

4.4.3 Alternative models for radio emission from V339 Del

It has been shown through spectroscopic and imaging studies that nova ejecta are clumpy. Resolved nova shells at optical and radio wavelengths provide direct evidence of dense clumps possibly embedded in a wind following an eruption (e.g., Harman & O'Brien, 2003; Shara et al., 2012; Diaz et al., 2018). Spectroscopic studies of nova ejecta show that some emission line features at the nebular stage of evolution can be considered as originating from distinct ejected blobs of material (McLaughlin, 1964; Gallagher & Starrfield, 1976). In addition, X-ray light curves and spectra provide direct evidence of non-uniformity in the shells of novae (Williams, 2013; Takei et al., 2014). The ejecta of V339 Del have been associated with non-uniformity based on spectroscopic studies (Tarasova & Skopal, 2016). Tarasova et al. considered a non-uniform distribution of material to explain the non-symmetric emission lines of Hα. They concluded that the ejecta likely consist of a bipolar outflow confined at the equator by a disc.

This structure is not unique to V339 Del, as it has been observed in other novae (Mustel & Boyarchuk, 1970; Chomiuk et al., 2014, see also Chapter 2). This picture is supported by a non-uniform distribution of intensity in the resolved radio images of V339 Del. In order to reproduce the high-resolution images, a consideration would be obscuration of the receding component by a torus. In such a case the ejecta will consist of three components: polar outflows moving towards and away from the observer and a torus in between the outflows. If the torus is optically thick, then one of the polar outflows would be brighter than the other. The intensity distribution from such an outflow should depend on the orientation of the nova envelope (Hutchings, 1972; Seaquist & Bode, 2008). Such a model has long been considered for novae after analysis of their images and spectra (Mustel & Boyarchuk, 1970).

Another consideration to explain the discrepancy between the observations and models is that not all the emission from V339 Del is free-free emission. High brightness temperatures and detection of high energy emission indicate the presence of more than one form of radio emission. In order to model the free-free emission from the beginning of the eruption, the additional mechanism needs to be established and accounted for. The morphology of the nova and the expansion rate should be fully established through modelling of the images in the u,v plane to avoid confusion from the restoring beam.

4.5 Conclusions

V339 Del is observed with similar behaviour to other classical novae at radio wavelengths, with the radio emission observed to increase, peak and decay within a period of ~ 3.5 years (see Figure 4.1). However, the radio light curve at all the phases cannot be fully described by emission from an expanding thermal nova shell. The nova shows evidence of shock powered non-thermal emission in the form of hard X-ray and $\gamma-$ray emission early on during the evolution of the ejecta, and we also find tentative evidence of non-thermal radio emission.

Following the high resolution radio images throughout the nova evolution (Figure 4.5), it is clear that the early images on day 221 represent the bulk of the ejecta, while in the later images on day 758, the slower ejecta dominate the high resolution images. The morphology of V339 Del is similar to that of *Fermi*-detected classical nova V959 Mon, which was determined via emission line modelling and resolved radio imaging (Ribeiro et al., 2013; Linford et al., 2015). Since both novae are strong $\gamma-$ray sources, this adds to the growing evidence that bipolar morphology provides an ideal scenario for shocks in novae that produce non-thermal emission.

The radio light curves and images later on in the evolution, ≈ 1 year after the eruption, are compared with a bipolar model of an expanding nova envelope emitting free-free emission. Comparison of observations with synthetic light curves and radio images from SHAPE show that the radio emission was produced by ejecta of mass $M_{\rm ej} \approx 10^{-4}$ M$_\odot$ for a nova ejecta with smooth density distribution and $M_{\rm ej} \approx 3 \times 10^{-5}$ M$_\odot$ for a clumpy ejecta. The less massive ejection inferred from spectroscopic studies underpredicts the radio flux densities as shown in Figure 4.9.

CHAPTER 5

SUMMARY AND FUTURE WORK

Presented in this thesis are detailed radio frequency observations of three novae to study their ejecta resulting from a thermonuclear runaway in these systems. High cadence observations have proved vital in showing deviations from known radio models of novae. As discussed in Chapter 1, the nova ejecta are dominated by either thermal bremsstrahlung emission or synchrotron emission. The non-thermal synchrotron emission is determined by the strength of the amplified magnetic field and the number of relativistic particles accelerated in shocked regions: either within the ejecta, between different outflows, or from the ejecta impacting the circumstellar material. Thermal emission is due to ionized expelled ejecta.

In Chapter 2, the importance of shocks is highlighted in the helium nova V445 Pup. The helium nova was a strong radio source showing flux densities between 0.2 – 20 mJy, dominated by synchrotron emission throughout the seven years it was observed with the VLA (2001 – 2008). There is no evidence of thermal emission from the expanding ionized nova ejecta. Throughout the radio evolution, the light curve is characterised by four distinct radio flares, where some are susceptible to free-free absorption. High resolution radio images show that the location of synchrotron emission is close to the binary system, coinciding spatially with the inner edge of the nova shell.

These results imply that the source of synchrotron radio emission in V445 Pup is an interaction between an equatorial disc of ejecta and a wind from the white dwarf driven by radiation pressure due

to residual helium burning. This interaction can give rise to shocks where particle acceleration occurs producing synchrotron emission. This is the same way non-thermal emission is produced in hydrogen-rich classical novae. However, for V445 Pup, the emission lasts for almost a decade as compared to other novae where this can last for a few weeks or months. This implies that the equatorial disc of the ejected material and the wind were present throughout the seven years of synchrotron emission. The radio flares are suggested to be produced by changes in density of the material in the disc or variations in the velocity of the wind from the white dwarf.

In Chapter 3, shock-powered emission in the recurrent nova V3890 Sgr is investigated. The MeerKAT radio observations of the 2019 eruption last for nine months. Using an external free-free absorption model, the radio light curve is replicated by assuming the shock emission formed between the ejected envelope and a dense wind from the red giant companion star. These shocks formed sites for particle acceleration and consequently led to the production of synchrotron emission. However, the observed radio light curve cannot be explained by a single interaction of nova ejecta and a spherical wind-like medium. It is therefore possible for the surrounding medium to be structured as observed in other recurrent novae such as RS Oph.

In Chapter 4, comprehensive radio coverage of classical nova V339 Del is presented. The radio data demonstrate the presence of shock powered emission in addition to emission from expanding photoionized nova ejecta. This resulted in double peaked radio light curves. It is not surprising that shocks are observed in this nova given the structure of its ejecta, which consist of a combination of slow and faster moving material (Schaefer et al., 2014). This picture is in agreement with the high resolution images from the VLA presented in this work. The interface of different components moving away following an eruption has been shown to form sites of shocks during the common envelope phase where the binary system interacts with the ejected envelope.

From the study of the three novae presented in this work, it is clear that shocks in novae are important when studying their radio evolution. Based on these studies, several potential future research projects have been identified, which I discuss briefly below.

The helium nova V445 Pup is considered a SN type Ia progenitor by different authors. This is not surprising given that helium accretion onto a CO white dwarf has been considered as one of the pathways for formation of SNe Ia. However, the current formalisation of SN Ia blastwaves that produce synchrotron emission is different from the mechanism producing non-thermal emission in V445 Pup as discussed in

this thesis. Therefore, before the radio luminosity from V445 Pup can be compared with that of known SNe Ia, hydrodynamic modelling is required to determine the mass loss rate from the compact object and the distribution of material in the equatorial region of the binary system. This will thus make it possible to predict observational signatures for SNe resulting from helium accretion.

This work shows evidence that the recurrent nova V3890 Sgr is a possible progenitor of SNe Ia based on the rate of mass loss from the companion star and the distribution of the material surrounding the binary system. The structure of material around the binary system for another well studied recurrent symbiotic nova, RS Oph, has been determined in detail using hydrodynamic simulations (Mohamed et al., 2013). These models provide hints in connecting these systems to SNe Ia (Booth et al., 2016). The radio study carried out in this work (Chapter 3) provides an indication that the density falls faster than r^{-2} at a radial distance $1-2\times10^{15}$ cm from the white dwarf. Similar hydrodynamics simulations could reveal details about the mass transfer processes and interaction between a blast wave and the circumstellar material in these systems. Mass loss from the evolved companion star could be described in detail, such that the amount of material accreted onto the compact object, the fraction of material concentrated in the equatorial plane, and the amount of material distributed around the binary system is established. The mass distribution is thought to have implications in linking these systems to SNe Ia (Mohamed & Podsiadlowski, 2007).

The study of V339 Del presented here demonstrates that shocks in hydrogen-rich classical novae should be incorporated into radio emission models. Historical work on modelling the radio emission from nova ejecta after an eruption is based on a freely expanding cloud of gas with no shock interactions. The number of novae that are showing signatures of shock emission early on ($\sim$ day 100) after optical discovery is growing. Examples of such systems include the work on V339 Del in Chapter 4, QU Vul (Taylor et al., 1987), V959 Mon (Chomiuk et al., 2014), V1723 Aql (Weston et al., 2016a), V5589 Sgr (Weston et al., 2016b), and V1324 Sco (Finzell et al., 2018). Recently, attempts have been made to fit the early radio peaks with different colliding components internal to the nova that produce either hot-thermal gas or non-thermal emission. However, the fits do not describe the radio light curves adequately as shown by Metzger et al. (2014) and Vlasov et al. (2016). This provides an opportunity to investigate this phase of nova evolution and mechanisms that shape the nova ejecta. Neither the models presented in this work nor existing models utilised to describe radio emission from V339 Del account for the dips in the radio light curve.

Mass accretion and mass ejection/loss mechanisms in novae still remain poorly understood. This work

has added to the evidence that radio light curves of novae are quite diverse and are dominated by either free-free thermal emission, synchrotron emission, or both. While the origin of free-free emission is fairly well understood, the presence of shocks in novae—hence non-thermal emission—is still a field that needs more investigating. Some of the open questions include establishing whether complex morphologies of the ejecta are present for all novae showing shock powered emission such as that observed in V339 Del. There is observational evidence that mass loss in novae can occur in the form of a single impulsive event which occurs on the day of the eruption, optically thick winds driven by either residual helium or hydrogen burning, interaction between the ejecta and the binary, or a combination of these processes (Mason et al., 2018; Friedjung, 1966; Livio et al., 1990). It is unclear how the morphologies of nova ejecta connect with all the mass loss mechanisms. In order to form shells of material in the orbital plane of the binary system as seen in V445 Pup, a possible mass transfer process is shown in the nova RS Oph (Mohamed et al., 2013). However, the two novae have different orbital periods $P \approx$ several days for V445 Pup (Woudt et al., 2021 in prep) and 1.2 years for RS Oph (Kenyon & Garcia, 1986). This presents an unexplored parameter space of theoretical modelling of how relatively short orbital period binary systems can accrete mass and form regions of enhanced densities in the equatorial plane.

While thermal radio emission traces outflows stellar explosions, non-thermal emission traces shocked material from these systems. Both emissions have been shown to be present in novae and provide physical insights from the thermonuclear eruptions. Complexity of mass ejection processes in novae has been revealed by upgraded facilities such as the Karl G. Jansky Very Large Array and new facilities such as the MeerKAT telescope. The sensitivity of the Square Kilometre Array will provide an opportunity to perform complex tests of the mass loss theories in novae.

APPENDIX A

APPENDIX FOR CHAPTER 2 - V445 PUP

A.1 VLA observations of V445 Pup, measured flux densities and spectral indices

A.1.1 Log of VLA observations of V445 Pup

Table A.1: Log of VLA observations of V445 Pup

Observation	t	$t-t_0$	Configuration	Observation time on target (Mins)					
Date	MJD	Days		1.4 GHz	4.9 GHz	8.46 GHz	14.94 GHz	22.46 GHz	43.34 GHz
2001 Oct 04	52187	337	C&D	8.9	6.7	6.7	6.7	6.7	6.2
2001 Oct 08	52191	341	C&D	3.1	4.7	4.7	3.7	5.2	5.4
2001 Oct 10	52193	343	C&D	3.6	4.2	4.2	5.1	5.2	5.6
2001 Oct 12	52195	345	D	2.6	4.1	4.2	5.1	5.2	5.6
2001 Oct 14	52197	347	D	4.4	4.2	4.2	5.7	6.9	6.4
2001 Oct 17	52200	350	D	10.2	4.2	4.2	6.2	7.6	...
2001 Oct 22	52204	354	D	2.9	2.7	2.4	5.2	...	4.7
2001 Oct 24	52207	357	D	4.9	2.7	2.8	6.9	7.6	...
2001 Oct 26	52209	359	D	5.4	5.7	7.4	7.7	7.6	...
2001 Oct 27	52210	360	D	7.3	5.6	7.4	7.7	7.7	...
2001 Oct 29	52212	362	D	4.4	4.7	4.7	6.9	7.4	...
2001 Nov 02	52216	366	D	7.6	8.4	8.6	7.6	7.7	...
2001 Nov 04	52218	368	D	7.8	8.4	24.6	9.2	...	...
2001 Nov 06	52220	370	D	5.9	5.3	5.2	6.2	...	...
2001 Nov 07	52221	371	D	5.9	4.7	4.2	5.8	6.6	...
2001 Nov 11	52224	374	D	6.1	...	4.2	5.3	6.2	5.7
2001 Nov 14	52227	377	D	...	3.9	3.7	...	...	...
2001 Nov 15	52229	379	D	4.1	4.2	2.2	5.1	...	...
2001 Nov 16	52230	380	D	...	5.2	4.9	6.2	6.9	...
2001 Nov 18	52231	381	D	4.2	5.1	3.1	6.2	6.9	...
2001 Nov 20	52233	383	D	4.6	4.2	4.2	6.0	6.9	6.2
2001 Nov 23	52236	386	D	...	4.9	...	...	...	...
2001 Nov 24	52237	387	D	...	4.4	5.1	5.7	7.1	...
2001 Nov 26	52240	390	D	8.1	4.2	...	6.4	...	...
2001 Nov 29	52242	392	D	5.1	5.1	5.4	6.1	7.1	...
2001 Dec 07	52250	400	D	8.2	4.2	4.2	6.2	...	...
2001 Dec 09	52252	402	D	...	...	5.2	6.2	...	...
2001 Dec 31	52274	424	D	5.3	4.2	4.1	6.2	...	...
2002 Jan 05	52279	429	D	7.6	4.2	4.1	6.1	6.7	6.2
2002 Jan 12	52286	436	D	...	4.1	4.2	4.7	...	...
2002 Jan 13	52287	437	D	...	4.1	...	5.6	...	...
2002 Jan 23	52297	447	A	6.4	5.9	7.6	10.6	...	...
2002 Feb 07	52312	462	A	4.2	3.2	9.1	4.7	...	...
2002 Feb 14	52319	469	A	1.9	4.6	10.9	4.7	...	...
2002 Feb 21	52326	476	A	4.1	2.3	6.2	4.7	...	...

'...' indicates no observations for this epoch at that frequency. Here, t_0 is taken as 2000 November 02 (MJD = 51850).

Table A.1: Log of VLA observations of V445 Pup

Observation	t	$t-t_0$	Configuration	Observation time on target (Mins)					
Date	MJD	Days		1.4 GHz	4.9 GHz	8.46 GHz	14.94 GHz	22.46 GHz	43.34 GHz
2002 Mar 01	52334	484	A	3.9	3.1	7.6	3.7	...	...
2002 Mar 06	52339	489	A	...	...	4.7	...	...	...
2002 Mar 10	52343	493	A	4.6	4.6	9.1	3.7	4.2	...
2002 Mar 18	52351	501	A	2.6	3.2	4.6	3.2	3.2	...
2002 Apr 03	52367	517	A	3.2	5.2	6.1	3.6	3.2	...
2002 Apr 21	52385	535	A	3.2	5.2	6.1	...	...	...
2002 Apr 29	52393	543	A	6.6	5.2	15.3	5.9	...	...
2002 May 04	52398	548	A	6.1	5.2	...	6.1	...	...
2002 May 17	52412	562	A&B	3.3	4.2	...	...	...	...
2002 May 26	52421	571	A&B	3.2	3.1	...	...	...	...
2002 Jun 07	52433	583	A&B	4.0	3.2	...	...	...	...
2002 Jun 17	52443	593	B	3.6	3.2	...	...	...	...
2002 Jun 25	52451	601	B	3.4	3.2	3.1	..	...	...
2002 Jul 05	52461	611	B	3.4	3.2	3.1	...	...	...
2002 Jul 19	52475	625	B	...	...	16.3	...	...	...
2002 Jul 27	52483	633	B	4.1	3.2	4.7	...	...	...
2002 Aug 17	52504	654	B	4.72	6.2	10.6	...	...	...
2002 Aug 30	52517	667	B	10.6	14.0	13.6	...	...	...
2002 Sep 01	52519	669	B	6.6	8.1	7.9	...	...	...
2002 Oct 04	52552	702	B	...	7.1	7.6	...	...	...
2002 Oct 28	52575	725	B	4.9	4.1	4.2	...	...	...
2002 Oct 31	52579	729	B	...	...	4.1	...	...	4.7
2002 Dec 09	52617	767	C	...	8.2	8.4	...	...	...
2002 Dec 21	52629	779	C	...	6.2	6.1	...	...	...
2002 Dec 29	52637	787	C	...	6.1	6.1	...	...	...
2003 Jan 03	52642	792	C	...	8.1	8.1	...	...	...
2003 Jan 06	52645	795	C	...	8.1	8.2	...	...	...
2003 Jan 08	52647	797	C	...	8.1	8.2	...	...	...
2003 Jan 14	52653	803	C	...	9.2	9.2	...	...	...
2003 Jan 20	52659	809	C	...	9.1	9.1	...	...	...
2003 Jan 29	52668	818	C	...	9.7	9.0	...	...	...
2003 Feb 06	52676	826	D	8.6	9.7	9.1	...	...	...
2003 Feb 23	52693	843	D	...	9.7	9.1	...	...	...
2003 Mar 04	52702	852	D	...	10.4	9.9	...	...	...
2003 Mar 11	52709	859	D	...	10.3	12.2	...	...	...
2003 Mar 13	52711	861	D	...	16.4	22.1	...	...	...
2003 Mar 19	52717	867	D	...	10.4	9.2	...	...	...

'...' indicates no observations for this epoch at that frequency. Here, t_0 is taken as 2000 November 02 (MJD = 51850).

Table A.1: Log of VLA observations of V445 Pup

Observation	t	$t-t_0$	Configuration	Observation time on target (Mins)					
Date	MJD	Days		1.4 GHz	4.9 GHz	8.46 GHz	14.94 GHz	22.46 GHz	43.34 GHz
2003 Mar 26	52724	874	D	...	10.6	9.2	...	...	...
2003 Apr 18	52748	898	D	...	15.9	12.2	...	...	...
2003 May 30	52790	940	A	8.8	6.9	6.2	...	...	...
2003 Jun 04	52795	945	A	8.6	7.0	...	...	...	...
2003 Jun 16	52807	957	A	8.8	7.7	...	...	...	...
2003 Jun 30	52821	971	A	8.9	7.7	...	...	...	...
2003 Jul 18	52839	989	A	...	...	15.2	...	...	...
2003 Jul 21	52842	992	A	...	15.2	...	...	...	...
2003 Jul 25	52846	996	A	...	16.2	...	...	...	...
2003 Jul 31	52856	1002	A	...	...	9.6	...	...	...
2003 Aug 11	52863	1013	A	8.6	9.2	11.1	...	...	...
2003 Aug 25	52877	1027	A	6.9	9.1	10.7	...	...	...
2003 Sep 03	52886	1036	A	7.3	9.1	18.2	...	...	...
2003 Sep 11	52894	1044	A	10.9	10.1	22.4	...	...	...
2003 Sep 19	52902	1052	A	10.9	...	24.4	...	...	...
2003 Sep	52905	1055	A	8.6	8.1	10.7	...	...	...
2003 Sep 27	52910	1060	A&B	10.8	10.1	...	...	...	...
2003 Sep 29	52912	1062	A&B	...	10.6	11.6	...	...	...
2003 Oct 08	52921	1071	A& B	...	12.2	...	...	...	...
2003 Oct 21	52934	1084	B	...	10.2	14.2	...	...	...
2003 Nov 02	52946	1096	B	...	8.2	8.3	...		
003 Nov 09	52953	1103	B	...	8.7	18.4	...	...	...
2003 Nov 18	52962	1112	B	...	...	14.4	...	...	...
2003 Nov 24	52967	1117	B	...	8.7	10.2	...	...	...
2003 Dec 15	52988	1138	B	5.9	9.1	12.2	...	...	...
2003 Dec 28	53001	1151	B	5.9	9.1	12.2	...	...	...
2004 Jan 03	53007	1157	B	5.1	9.1	12.2	...	...	...
2004 Jan 08	53012	1162	B	5.7	9.2	11.7	...	...	...
2004 Jan 14	53018	1168	B	...	9.2	11.5	...	...	...
2004 Jan 23	53027	1177	B&C	...	6.2	6.4	...	...	...
2004 Feb 01	53036	1186	B&C	5.9	6.2	6.2			

'...' indicates no observations for this epoch at that frequency. Here, t_0 is taken as 2000 November 02 (MJD = 51850).

Table A.1: Log of VLA observations of V445 Pup

Observation	t	$t-t_0$	Configuration	Observation time on target (Mins)					
Date	MJD	Days		1.4 GHz	4.9 GHz	8.46 GHz	14.96 GHz	22.46 GHz	43.34 GHz
2004 Feb 02	53037	1187	B&C	...	...	4.1	10.3	10.2	10.7
2004 Feb 12	53047	1197	B&C	...	4.2	4.1	...	9.0	10.7
2004 Feb 24	53059	1209	B&C	...	4.2	4.1	...	11.9	...
2004 Mar 02	53066	1216	B&C	...	4.2	4.1	...	12.3	...
2004 Mar 10	53074	1224	C	...	57.4	...	...	...	...
2004 Mar 20	53084	1234	C	...	4.2	8.1	...	...	...
2004 Mar 22	53086	1236	C	...	...	6.2	...	...	...
2004 Apr 01	53096	1246	C	...	...	8.2	...	...	...
2004 Apr 07	53102	1252	C	...	4.2	8.1	...	13.6	...
2004 Apr 15	53111	1261	C	...	4.2	4.8	...	...	...
2004 May 03	53129	1279	C	...	5.2	8.1	...	...	...
2004 May 10	53136	1286	C	10.6	10.6	9.9	...	...	...
2004 May 17	53143	1293	C& D	10.6	8.9	10.1	...	...	...
2004 May 22	53147	1297	C& D	7.4	...	...	...	...	...
2004 May 30	53156	1306	C& D	6.8	5.2	5.1	...	...	...
2004 Jun 12	53169	1319	C& D	6.0	8.9	10.1	...	...	...
2004 Jun 25	53182	1332	D	...	8.9	10.1	...	...	...
2004 Jul 01	53188	1338	D	...	8.6	10.1	...	...	...
2004 Jul 10	53197	1347	D	...	...	10.1	20.4	...	...
2004 Jul 17	53204	1354	D	...	8.9	10.1	19.2	...	...
2004 Jul 23	53210	1360	D	...	8.6	6.9	....	...	...
2004 Aug 07	53225	1375	D	...	8.9	10.1	12.7	...	...
2004 Aug 21	53239	1389	D	...	9.2	10.2	10.2	...	...
2004 Sep 09	53258	1408	A	...	9.2	10.2	10.2	...	...
2004 Sep 23	53272	1422	A	...	8.6	12.2	...	...	...
2004 Oct 01	53280	1430	A	...	...	18.2	...	...	...
2004 Oct 08	53287	1437	A	...	...	17.4	...	...	...
2004 Oct 16	53295	1445	A	...	...	15.2	...	...	...
2004 Oct 31	53310	1460	A	...	9.1	9.2	...	...	...
2004 Nov 03	53312	1462	A	...	8.2	18.2	...	...	...
2004 Nov 07	53317	1467	A	...	...	14.1	...	...	...
2004 Nov 12	53321	1471	A	...	...	21.1	...	...	...
2004 Nov 20	53329	1479	A	...	...	20.8	...	...	...
2004 Nov 29	53338	1488	A	...	...	21.2	...	...	...
2004 Dec 22	53361	1511	A	...	...	14.6	...	...	...
2004 Dec 31	53370	1520	A	...	...	15.2	...	...	...
2005 Jan 06	53376	1526	A	...	...	13.6	...	...	...

'...' indicates no observations for this epoch at that frequency. Here, t_0 is taken as 2000 November 02 (MJD = 51850).

Table A.1: Log of VLA observations of V445 Pup

Observation	t	$t-t_0$	Configuration	Observation time on target (Mins)					
Date	MJD	Days		1.4 GHz	4.9 GHz	8.46 GHz	14.96 GHz	22.46 GHz	43.34 GHz
2005 Jan 16	53386	1536	A& B	...	...	10.2	...	...	...
2005 Jan 24	53394	1544	A& B	...	...	8.6	...	...	...
2005 Jan 29	53399	1549	A& B	...	12.1	11.8	...	...	...
2005 Feb 03	53404	1554	A& B	...	...	7.1	...	...	...
2005 Feb 26	53427	1577	B	...	8.6	9.2	...	...	...
2005 Mar 13	53442	1592	B	8.9	8.1	10.3	...	...	...
2005 Mar 20	53449	1599	B	8.8	8.1	10.4	...	...	...
2005 Mar 25	53454	1604	B	8.9	8.1	10.2	...	...	...
2005 Apr 04	53464	1614	B	...	37.7	...	...	...	...
2005 Apr 14	53475	1625	B	...	6.6	8.2	...	...	...
2005 Apr 26	53486	1636	B	...	6.4	9.1	...	...	...
2005 May 06	53497	1647	B	...	5.2	9.0	...	...	...
2005 May 14	53504	1654	B	...	5.1	10.2	...	...	...
2005 May 29	53520	1670	B	...	22.4	...	...	...	...
2005 Jun 03	53525	1675	B	...	19.9	...	...	...	...
2005 Jun 12	53534	1684	B&C	...	...	10.7	...	...	...
2005 Jun 18	53540	1690	B&C	...	...	15.4	...	...	...
2005 Jun 23	53545	1695	B&C	...	13.1	12.2	...	...	...
2005 Jul 02	53554	1704	B&C	11.4	13.1	12.2	...	...	...
2005 Jul 09	53561	1711	C	...	...	4.2	...	...	...
2005 Jul 14	53566	1716	C	...	10.9	...	...	...	...
2005 Jul 23	53575	1725	C	...	10.1	14.2	...	...	...
2005 Aug 02	53585	1735	C	...	...	17.2	...	...	...
2005 Aug 06	53589	1739	C	...	...	6.2	...	...	...
2005 Aug 27	53610	1760	C	...	20.2	12.2	...	...	...
2005 Sep 05	53619	1769	C	...	20.4	16.7	...	...	...
2005 Sep 25	53639	1789	C	...	22.2	...	...	...	...
2005 Sep 27	53641	1791	C	...	12.2	18.2	...	...	...
2005 Oct 01	53645	1795	C	...	20.4	16.7	...	...	...
2005 Oct 05	53649	1799	C&D	...	...	14.4	...	...	...
2005 Oct 16	53660	1810	C&D	...	...	10.4	...	18.7	...
2005 Oct 23	53666	1816	C&D	...	61.6	14.2	...	...	...
2005 Oct 31	53675	1825	C&D	...	...	18.4	...	...	...

'...' indicates no observations for this epoch at that frequency. Here, t_0 is taken as 2000 November 02 (MJD = 51850).

Table A.1: Log of VLA observations of V445 Pup

Observation	t	$t-t_0$	Configuration	Observation time on target (Mins)					
Date	MJD	Days		1.4 GHz	4.9 GHz	8.46 GHz	14.96 GHz	22.46 GHz	43.34 GHz
2005 Nov 08	53683	1833	D	...	9.1	9.2	...	...	...
2005 Nov 15	53690	1840	D	...	...	9.2	...	...	...
2005 Nov 21	53696	1846	D	...	...	21.2	...	...	...
2005 Nov 29	53703	1853	D	...	...	17.4	...	...	...
2005 Dec 01	53705	1855	D	...	13.2	15.6	...	...	...
2005 Dec 11	53715	1865	D	...	13.1	15.6	...	...	...
2005 Dec 20	53724	1874	D	...	13.1	15.2	...	...	...
2006 Jan 13	53748	1898	D	...	...	14.9	...	...	...
2006 Jan 15	53750	1900	D	...	...	18.2	...	...	...
2006 Jan 22	53757	1907	D	...	9.2	...	...	...	...
2006 Feb 09	53775	1925	A	...	...	16.2	...	...	...
2006 Mar 15	53809	1959	A	9.6	...	12.2	...	...	...
2006 Mar 22	53816	1966	A	9.5	...	...	...	...	...
2006 April 07	53832	1982	A	8.9	...	...	...	...	...
2006 May 08	53863	2013	A	...	...	20.2	...	...	...
2006 May 10	53865	2015	A	...	...	14.2	...	...	...
2006 Aug 05	53953	2103	B	...	...	24.6	...	...	...
2006 Aug 09	53957	2107	B	...	24.4	...	...	...	...
2006 Aug 31	53979	2129	B	...	20.6	...	...	...	...
2006 Sep 11	53990	2140	B	...	38.3	...	...	...	...
2007 Jan 23	54123	2273	C&D	...	...	29.3	...	...	...
2007 Sep 30	54374	2524	A&B	...	...	36.0	...	...	...
2008 Jan 17	54482	2632	B	...	...	28.0	...	...	...
2008 Mar 28	54554	2704	C	...	...	10.4	...	...	...

'...' indicates no observations for this epoch at that frequency. Here, t_0 is taken as 2000 November 02 (MJD = 51850).

A.1.2 Flux densities and spectral indices of V445 Pup

Table A.2: Flux densities and spectral indices of V445 Pup

t	$t-t_0$	Radio flux densities (mJy)						α
(MJD)	(Days)	1.43 GHz	4.86 GHz	8.46 GHz	14.94 GHz	22.46 GHz	43.34 GHz	
52187	337	12.62 ± 0.67	13.85 ± 0.71	12.01 ± 0.62	8.69 ± 0.91	5.98 ± 0.88	5.10 ± 1.21	−0.46 ± 0.08
52191	341	14.26 ± 0.76	14.01 ± 0.73	11.33 ± 0.60	7.54 ± 1.17	8.61 ± 1.26	4.30 ± 1.18	−0.43 ± 0.07
52193	343	13.54 ± 0.80	12.48 ± 0.66	9.29 ± 0.52	7.27 ± 0.88	5.13 ± 1.05	2.49 ± 0.78	−0.58 ± 0.06
52195	345	12.15 ± 0.85	11.46 ± 0.63	8.67 ± 0.49	5.83 ± 0.71	5.66 ± 0.75	7.00 ± 1.22	−0.24 ± 0.07
52197	347	14.75 ± 1.21	10.4 ± 0.57	7.64 ± 0.42	7.93 ± 0.87	7.79 ± 0.92	7.21 ± 1.16	−0.25 ± 0.06
52200	350	13.96 ± 1.18	8.81 ± 0.50	8.45 ± 0.46	8.31 ± 0.91	7.36 ± 1.0	...	−0.23 ± 0.06
52204	354	10.30 ± 1.31	8.83 ± 0.79	7.56 ± 0.46	5.82 ± 0.66	...	3.14 ± 0.86	−0.27 ± 0.07
52207	357	10.20 ± 0.93	7.37 ± 0.41	7.30 ± 0.44	6.18 ± 0.68	4.2 ± 0.57	...	−0.24 ± 0.02
52209	359	12.5 ± 1.18	8.2 ± 0.44	7.17 ± 0.37	5.69 ± 0.60	5.64 ± 0.72	...	−0.30 ± 0.02
52210	360	9.42 ± 0.84	7.23 ± 0.40	6.72 ± 0.36	4.52 ± 0.58	3.71 ± 0.69	...	−0.26 ± 0.07
52212	362	8.42 ± 0.45	7.52 ± 0.41	6.62 ± 0.38	4.30 ± 0.51	3.94 ± 0.72	...	−0.20 ± 0.07
52216	366	8.14 ± 0.44	6.99 ± 0.37	5.29 ± 0.30	3.62 ± 0.50	1.89 ± 0.41	...	−0.65 ± 0.13
52218	368	8.29 ± 0.42	6.33 ± 0.35	4.75 ± 0.25	3.95 ± 0.52	...	...	−0.30 ± 0.05
52220	370	10.26 ± 0.61	5.66 ± 0.35	4.28 ± 0.26	3.16 ± 0.49	...	...	−0.49 ± 0.01
52221	371	8.56 ± 0.45	5.52 ± 0.33	4.28 ± 0.26	3.51 ± 0.40	2.53 ± 0.54	...	−0.39 ± 0.02
52224	374	8.39 ± 0.42	...	4.48 ± 0.28	4.57 ± 0.65	2.96 ± 0.77	2.89 ± 0.477	−0.32 ± 0.03
52227	377		...	4.81 ± 0.037	4.29 ± 0.29	...	...	...
52229	379	6.79 ± 0.93	4.68 ± 0.29	4.71 ± 0.35	4.89 ± 0.83	...	...	−0.15 ± 0.09
52230	380	...	4.5 ± 0.28	5.01 ± 0.29	4.80 ± 0.60	3.72 ± 0.64	...	−0.22 ± 0.13
52231	381	5.61 ± 0.81	4.81 ± 0.30	5.25 ± 0.29	4.38 ± 0.54	3.88 ± 0.59	...	−0.10 ± 0.06
52233	383	9.99 ± 0.58	5.10 ± 0.33	4.66 ± 0.26	3.65 ± 0.47	3.15 ± 0.48	2.14 ± 0.63	−0.43 ± 0.04
52236	386	...	4.95 ± 0.41	...	...	...	...	...
52237	387	...	4.49 ± 0.33	4.01 ± 0.26	3.15 ± 0.44	2.39 ± 0.52	...	−0.34 ± 0.08
52240	390	6.39 ± 0.37	4.51 ± 0.32	...	2.35 ± 0.51	...	...	−0.33 ± 0.08
52242	392	12.38 ± 1.08	4.10 ± 0.29	3.46 ± 0.20	2.30 ± 0.33	2.59 ± 0.72	...	−0.43 ± 0.03
52250	400	4.91 ± 0.47	3.30 ± 0.30	2.49 ± 0.26	1.97 ± 0.47	...	...	−0.38 ± 0.03
52252	402	...	...	2.16 ± 0.22	2 .30 ± 0.40	...	...	...
52274	424	5.03 ± 0.27	2.02 ± 0.23	1.71 ± 0.18	3.09 ± 0.71	...	...	−0.54 ± 0.16
52279	429	6.31 ± 0.57	2.02 ± 0.17	2.65 ± 0.19	3.12 ± 0.42	3.77 ± 0.57	3.20 ± 1.15	0.36 ± 0.06
52286	436	...	3.91 ± 0.33	4.67 ± 0.33	4.36 ± 0.78	...	...	0.19 ± 0.15
52287	437	...	3.61 ± 0.30	...	2.80 ± 0.62	...	...	...
52297	447	4.46 ± 0.29	4.93 ± 0.31	9.38 ± 0.52	14.01 ± 1.52	...	...	0.44 ± 0.18
52312	462	6.91 ± 0.36	21.92 ± 1.12	17.68 ± 0.89	11.39 ± 1.30	...	...	−0.51 ± 0.13

'...' indicates no measurements for flux density for this epoch at that frequency

Table A.2: Flux densities and spectral indices of V445 Pup

t	$t-t_0$	Radio flux densities (mJy)						α
(MJD)	(Days)	1.43 GHz	4.86 GHz	8.46 GHz	14.94 GHz	22.46 GHz	43.34 GHz	
52319	469	11.49 ± 0.63	15.53 ± 0.83	13.02 ± 0.67	4.35 ± 0.95	...	...	−0.54 ± 0.44
52326	476	16.27 ± 0.83	14.09 ± 0.74	10.38 ± 0.54	6.46 ± 1.04	...	...	−0.26 ± 0.09
52334	484	17.91 ± 1.12	13.34 ± 0.82	9.23 ± 0.50	6.02 ± 0.91	...	...	−0.39 ± 0.08
52339	489	...	...	8.53 ± 0.57	...	...	...	...
52343	493	18.65 ± 0.95	11.48 ± 0.63	8.44 ± 0.45	4.73 ± 0.60	3.39 ± 0.42	...	−0.53 ± 0.08
52351	501	16.44 ± 0.84	9.03 ± 0.86	6.72 ± 0.43	4.22 ± 1.00	2.93 ± 0.57	...	−0.53 ± 0.04
52367	517	12.30 ± 0.68	7.31 ± 0.40	6.15 ± 0.34	4.66 ± 0.55	3.12 ± 0.96	...	−0.41 ± 0.02
52385	535	9.30 ± 0.49	5.25 ± 0.41	3.66 ± 0.28	...	...	...	−0.51 ± 0.04
52393	543	7.91 ± 0.41	4.53 ± 0.30	2.88 ± 0.18	2.01 ± 0.35	...	...	−0.55 ± 0.05
52398	548	6.52 ± 0.35	3.69 ± 0.29	...	1.70 ± 0.32	...	...	−0.51 ± 0.06
52412	562	7.66 ± 0.59	1.97 ± 0.13	...	...	...	...	...
52421	571	4.84 ± 0.31	1.95 ± 0.16	...	...	...	...	...
52433	583	2.32 ± 0.13	1.43 ± 0.09	...	...	...	...	...
52443	593	2.79 ± 0.16	1.10 ± 0.13	...	...	...	...	...
52451	601	2.10 ± 0.11	1.40 ± 0.14	1.07 ± 0.26	...	...	...	−0.35 ± 0.02
52461	611	3.35 ± 0.21	1.01 ± 0.12	0.94 ± 0.20	...	...	...	−0.87 ± 0.15
52475	625	...	...	0.68 ± 0.08	...	...	...	...
52483	633	1.89 ± 0.11	1.02 ± 0.11	0.88 ± 0.14	...	...	...	−0.46 ± 0.04
52504	654	1.73 ± 0.15	0.99 ± 0.15	0.75 ± 0.10	...	...	...	−0.47 ± 0.01
52517	667	1.06 ± 0.08	0.61 ± 0.06	0.49 ± 0.05	...	...	...	−0.44 ± 0.01
52519	669	2.09 ± 0.11	1.20 ± 0.15	0.92 ± 0.17	...	...	...	−0.46 ± 0.00
52552	702	...	0.78 ± 0.12	0.61 ± 0.11	...	...	...	...
52575	725	1.46 ± 0.19	0.89 ± 0.07	0.49 ± 0.11	...	...	...	−0.47 ± 0.07
52579	729	...	...	0.52 ± 0.12	...	...	1.50 ± 0.31	...
52617	767	...	1.15 ± 0.08	0.98 ± 0.14	...	...	...	...
52629	779	...	0.80 ± 0.06	0.86 ± 0.12	...	...	...	...
52637	787	...	0.99 ± 0.11	0.88 ± 0.14	...	...	...	...
52642	792	...	0.85 ± 0.11	0.71 ± 0.10	...	...	...	...
52645	795	...	1.08 ± 0.12	0.84 ± 0.10	...	...	...	...
52647	797	...	0.77 ± 0.11	0.66 ± 0.16	...	...	...	...
52653	803	...	0.84 ± 0.10	0.61 ± 0.10	...	...	...	...
52659	809	...	0.77 ± 0.07	0.65 ± 0.10	...	...	...	...

'...' indicates no measurements for flux density for this epoch at that frequency

Table A.2: Flux densities and spectral indices of V445 Pup

t	$t-t_0$	Radio flux densities (mJy)						α
(MJD)	(Days)	1.43 GHz	4.86 GHz	8.46 GHz	14.94 GHz	22.46 GHz	43.34 GHz	
52668	818	...	1.22 ± 0.09	0.60 ± 0.07	...	...	...	...
52676	826	2.85 ± 0.59	0.78 ± 0.09	0.77 ± 0.07	...	...	...	−0.79 ± 0.08
52693	843	...	0.86 ± 0.11	0.63 ± 0.09	...	...	...	...
52702	852	...	0.90 ± 0.11	0.724 ± 0.13	...	...	...	...
52709	859	...	0.93 ± 0.10	0.80 ± 0.12	...	...	...	...
52711	861	...	0.94 ± 0.09	0.74 ± 0.09	...	...	...	...
52717	867	...	0.84 ± 0.09	0.83 ± 0.10	...	...	...	...
52724	874	...	1.42 ± 0.18	1.15 ± 0.13	...	...	...	...
52748	898	...	1.17 ± 0.11	0.66 ± 0.09	...	...	...	...
52790	940	2.21 ± 0.19	0.91 ± 0.09	0.24 ± 0.04	...	...	...	−0.93 ± 0.47
52795	945	2.53 ± 0.27	0.78 ± 0.08	...	...	...	...	...
52807	957	2.55 ± 0.24	0.90 ± 0.10	...	...	...	...	...
52821	971	2.49 ± 0.22	1.76 ± 0.22	...	...	...	...	...
52839	989	...	...	1.14 ± 0.10	...	...	...	...
52842	992	...	1.7 ± 0.15	...	...	...	...	...
52846	996	...	1.56 ± 0.15	...	...	...	...	...
52852	1002	...	...	0.65 ± 0.08	...	...	...	..
52863	1013	1.69 ± 0.16	1.37 ± 0.10	1.07 ± 0.08	...	...	...	−0.25 ± 0.08
52877	1027	2.22 ± 0.32	1.59 ± 0.23	1.49 ± 0.20	...	...	...	...
52886	1036	2.67 ± 0.24	1.89 ± 0.31	1.01 ± 0.08	...	...	...	...
52894	1044	1.49 ± 0.17	1.43 ± 0.16	0.87 ± 0.08	...	...	...	...
52902	1052	1.02 ± 0.16	...	1.10 ± 0.07	...	...	...	...
52905	1055	1.49 ± 0.16	1.51 ± 0.16	1.00 ± 0.14	...	...	...	...
52910	1060	2.05 ± 0.18	1.44 ± 0.12	...	...	...	...	...
52912	1062	...	1.58 ± 0.20	0.87 ± 0.08	...	...	...	...
52921	1071	...	1.09 ± 0.21	...	...	...	...	...
52934	1084	...	1.38 ± 0.11	1.28 ± 0.13	...	...	...	...
52946	1096	...	1.32 ± 0.16	1.28 ± 0.17	...	...	...	...
52953	1103	...	1.34 ± 0.16	1.28 ± 0.12	...	...	...	...
52962	1112	...	...	1.44 ± 0.15	...	...	...	...
52967	1117	...	1.59 ± 0.15	1.30 ± 0.15	...	...	...	...
52988	1138	1.41 ± 0.25	1.82 ± 0.11	1.46 ± 0.08	...	...	...	−0.10 ± 0.24
53001	1151	2.06 ± 0.10	1.72 ± 0.12	1.60 ± 0.15	...	...	...	...
53007	1157	3.06 ± 0.22	1.80 ± 0.18	1.71 ± 0.18	...	...	...	...
53012	1162	2.01 ± 0.11	1.90 ± 0.20	1.62 ± 0.16	...	...	...	...
53018	1168	...	1.76 ± 0.13	1.56 ± 0.14	...	...	...	...
53027	1177	...	1.74 ± 0.14	1.67 ± 0.15	...	...	...	...

'...' indicates no measurements for flux density for this epoch at that frequency

Table A.2: Flux densities and spectral indices of V445 Pup

t	$t-t_0$	Radio flux densities (mJy)						α
(MJD)	(Days)	1.43 GHz	4.86 GHz	8.46 GHz	14.94 GHz	22.46 GHz	43.34 GHz	
53036	1186	2.17 ± 0.19	2.10 ± 0.21	1.50 ± 0.16	...	...	...	...
53037	1187	...	...	1.54 ± 0.15	1.33 ± 0.38	1.05 ± 0.22	0.78 ± 0.18	−0.42 ± 0.08
53047	1197	...	2.09 ± 0.30	1.85 ± 0.19	...	0.84 ± 0.17	1.29 ± 0.37	...
53059	1209	...	1.53 ± 0.13	1.35 ± 0.12	...	1.14 ± 0.27	...	−0.20 ± 0.02
53066	1216	...	1.33 ± 0.12	1.30 ± 0.10	...	0.84 ± 0.18	...	...
53074	1224	...	1.72 ± 0.10	...	...	...	....	...
53084	1234	...	1.54 ± 0.17	1.34 ± 0.13	...	...	...	...
53086	1236	...	...	1.29 ± 0.15	...	...	...	...
53096	1246	...	...	1.10 ± 0.12	...	...	...	...
53102	1252	...	1.15 ± 0.12	1.27 ± 0.12	...	0.73 ± 0.14	...	−0.24 ± 0.28
53111	1261	...	1.37 ± 0.20	1.04 ± 0.12	...	...	...	...
53129	1279	...	1.61 ± 0.20	1.14 ± 0.15	...	...	...	...
53136	1286	2.27 ± 0.28	1.48 ± 0.10	1.18 ± 0.08	....	...	...	−0.37 ± 0.02
53143	1293	0.94 ± 0.17	1.63 ± 0.20	1.13 ± 0.16	...	...	...	...
53147	1297	3.45 ± 0.50	...	...	...	...	...	...
53156	1306	1.49 ± 0.18	1.79 ± 0.22	1.52 ± 0.18	...	...	...	...
53169	1319	2.51 ± 0.24	1.50 ± 0.16	1.23 ± 0.12	...	...	...	...
53182	1332	...	1.01 ± 0.10	0.72 ± 0.08	...	...	...	...
53188	1338	...	1.29 ± 0.18	0.96 ± 0.13	...	...	...	...
53197	1347	...	...	0.89 ± 0.12	0.59 ± 0.11	...	...	...
53204	1354	...	1.46 ± 0.12	1.17 ± 0.09	0.91 ± 0.19	...	...	−0.42 ± 0.01
53210	1360	...	1.42 ± 0.18	1.25 ± 0.17	...	...	...	...
53225	1375	...	1.21 ± 0.16	1.07 ± 0.12	0.98 ± 0.21	...	...	...
53239	1389	...	1.61 ± 0.18	1.37 ± 0.15	1.46 ± 0.28	...	...	...
53258	1408	...	1.26 ± 0.19	1.45 ± 0.31	1.16 ± 0.28	...	...	−0.03 ± 0.17
53272	1422	...	1.07 ± 0.11	1.43 ± 0.19	...	...	...	...
53280	1430	...	...	1.51 ± 0.19	...	...	...	...
53287	1437	...	...	1.56 ± 0.14	...	...	...	...
53295	1445	...	...	1.71 ± 0.15	...	...	...	...
53310	1460	...	1.61 ± 0.14	1.09 ± 0.16	...	...	...	...
53312	1462	...	1.12 ± 0.12	1.38 ± 0.14	...	...	...	...
53317	1467	...	...	1.39 ± 0.13	...	...	...	...
53321	1471	...	...	1.54 ± 0.13	...	...	...	...
53329	1479	...	...	1.21 ± 0.15	...	...	...	...
53338	1488	...	...	1.26 ± 0.17	...	...	...	...

'...' indicates no measurements for flux density for this epoch at that frequency

Table A.2: Flux densities and spectral indices of V445 Pup

53361	1511	...	...	1.27 ± 0.19	...	...	...	...
53370	1520	...	...	1.46 ± 0.19	...	...	...	...
53376	1526	...	...	1.27 ± 0.11	...	...	...	..
53386	1536	...	...	1.21 ± 0.17	...	...	...	...
53394	1544	...	...	1.38 ± 0.15	...	...	...	...
53399	1549	...	1.36 ± 0.15	1.23 ± 0.14	...	...	...	...
53404	1554	...	...	1.41 ± 0.16	...	...	...	...
53427	1577	...	1.28 ± 0.14	1.20 ± 0.13	...	...	...	...
53442	1592	1.15 ± 0.12	0.94 ± 0.07	0.87 ± 0.08	...	...	...	−0.16 ± 0.01
53449	1599	0.89 ± 0.08	1.05 ± 0.08	1.06 ± 0.12	...	...	...	...
53454	1604	1.10 ± 0.11	1.32 ± 0.18	1.02 ± 0.16	...	...	...	...
53464	1614	...	1.17 ± 0.09	...	...	...	...	...
53475	1625	...	0.96 ± 0.12	0.86 ± 0.12	...	...	...	...
53486	1636	...	1.21 ± 0.15	0.93 ± 0.11	...	...	...	...
53497	1647	...	1.13 ± 0.14	0.72 ± 0.10	...	...	...	...
53504	1654	...	0.90 ± 0.16	0.80 ± 0.12	...	...	...	...
53520	1670	...	0.94 ± 0.12	...	...	...	...	...
53525	1675	...	0.99 ± 0.12	...	...	...	...	...
53534	1684	...	...	0.62 ± 0.074	...	...	...	...
53540	1690	...	...	0.83 ± 0.09	...	...	...	...
53545	1695	...	1.01 ± 0.13	0.76 ± 0.13	...	...	...	...
53554	1704	1.42 ± 0.10	0.73 ± 0.07	0.81 ± 0.11	...	...	...	...
53561	1711	...	...	0.64 ± 0.08	...	...	...	...
53566	1716	...	0.77 ± 0.08	...	...	...	...	...
53575	1725	...	0.68 ± 0.08	0.51 ± 0.06	...	...	...	...
53585	1735	...	...	0.47 ± 0.08	...	...	...	...
53589	1739	...	...	0.78 ± 0.09	...	...	...	...
53610	1760	...	0.86 ± 0.09	0.53 ± 0.07	...	...	...	...
53619	1769	...	1.12 ± 0.14	0.53 ± 0.05	...	...	...	...
53639	1789	...	0.73 ± 0.08	...	...	...	...	...
53641	1791	...	0.58 ± 0.05	0.68 ± 0.04	...	...	...	...
53645	1795	...	0.65 ± 0.05	0.54 ± 0.05	...	...	...	...
53649	1799	...	...	0.61 ± 0.09	...	...	...	...

'...' indicates no measurements for flux density for this epoch at that frequency

Table A.2: Flux densities and spectral indices of V445 Pup

t	$t-t_0$	Radio flux densities (mJy)						α
(MJD)	(Days)	1.43 GHz	4.86 GHz	8.46 GHz	14.94 GHz	22.46 GHz	43.34 GHz	
53660	1810	...	...	0.75 ± 0.07	...	1.10 ± 0.30	...	...
53666	1816	...	...	0.66 ± 0.06	...	...	...	...
53675	1825	...	...	0.64 ± 0.07	...	...	...	...
53683	1833	...	0.62 ± 0.11	0.58 ± 0.09	...	...	...	...
53689	1840	...	...	0.57 ± 0.08	...	...	...	...
53696	1846	...	...	0.54 ± 0.07	...	...	...	...
53703	1853	...	...	0.74 ± 0.09	...	...	...	...
53705	1855	...	0.51 ± 0.05	0.55 ± 0.05	...	...	...	...
53715	1865	...	0.82 ± 0.18	0.64 ± 0.08	...	...	...	...
53724	1874	...	0.60 ± 0.12	0.53 ± 0.08	...	...	...	...
53748	1898	...	...	0.59 ± 0.08	...	...	...	...
53750	1900	...	...	0.48 ± 0.08	...	...	...	...
53757	1907	...	0.47 ± 0.09	...	...	...	...	...
53775	1925	...	...	0.43 ± 0.09	...	...	...	...
53809	1959	0.54 ±0.18	...	0.40 ± 0.09	...	...	...	...
53816	1966	0.51 ±0.12	...	...	...	...	...	...
53832	1982	0.61 ±0.22	...	...	...	...	...	...
53863	2013	...	...	0.66 ± 0.09	...	...	...	...
53865	2015	...	...	0.37 ± 0.05	...	...	...	...
53953	2103	...	...	0.21 ± 0.03	...	....	...	...
53957	2107	...	0.42 ± 0.08	...	...	...	...	...
53979	2129	...	0.30 ± 0.06	...	...	...	...	...
54123	2273	...	...	0.29 ± 0.06	...	...	...	...
54374	2524	...	...	0.22 ± 0.06	...	...	...	...
54482	2632	...	...	0.26 ± 0.09	...	...	...	...
54554	2704	...	...	0.19 ± 0.04	...	...	...	...

'...' indicates no measurements for flux density for this epoch at that frequency

APPENDIX B

APPENDIX FOR CHAPTER 4 - V339 DEL

B.1 Observation logs and measured flux densities of V339 Del

Table B.1: Flux densities of V339 Del obtained using VLA and CARMA telescopes

Date of observation	t (MJD)	$t-t_0$ (Days)	Array configuration	Frequency (GHz)	S_ν (mJy)	Frequency (GHz)	S_ν (mJy)
2013 Aug 16	56520.1	1.8	C	4.64	< 0.029	28.21	< 0.136
		1.8	C	7.38	< 0.017	36.53	< 0.089
2013 Aug 16	56520.3	2.0	CARMA E	95.7	< 1.23		
2013 Aug 22	56526.1	7.8	C	1.42	< 0.524	4.63	< 0.030
		7.8	C	1.76	< 0.348	7.37	< 0.033
		7.8	CARMA E	95.68	< 1.34		
2013 Aug 22	56526.3	8.0	C	28.21	< 0.124	36.53	< 0.196
2013 Aug 23	56527.3	9.0	C	28.21	< 0.132	36.53	< 0.146
2013 Aug 27	56531.0	12.7	C	1.42	< 0.523	7.39	< 0.067
		12.7	C	1.76	< 0.688	28.21	< 0.114
		12.7	C	4.62	< 0.089	36.53	< 0.140
2013 Sep 05	56540.1	21.8	C & B	1.41	< 0.327	4.66	< 0.118
		21.8	C	1.75	< 0.253	7.38	< 0.066
2013 Sep 08	56543.1	24.8	C & B	28.21	0.21 ± 0.04	36.53	0.32 ± 0.05
		24.8	CARMA E	95.7	3.49 ± 0.75		
2013 Sep 18	56553.0	34.7	C & B	4.63	< 0.044	7.39	< 0.058
	56553.1	34.8	CARMA E	95.7	6.92 ± 0.78		
2013 Sep 20	56555.0	36.7	CARMA E	230.4	56.28 ± 4.02		
2013 Sep 27	56562.0	43.7	B	1.25	< 0.672	4.55	0.046 ± 0.017
		43.7	B	1.73	< 0.30	7.38	0.095 ± 0.014
2013 Sep 27	56562.2	43.9	B	13.54	0.32 ± 0.03	28.21	1.02 ± 0.12
		43.9	B	17.44	0.46 ± 0.05	36.53	1.42 ± 0.16
2013 Sep 29	56564.1	45.8	B	13.54	0.45 ± 0.05	28.21	1.54 ± 0.16
		45.8	B	17.44	0.64 ± 0.07	36.53	2.20 ± 0.22
2013 Oct 03	56568.0	49.7	CARMA E	95.7	15.32 ± 1.56		
2013 Oct 04	56569.1	50.8	CARMA E	230.4	74.39 ± 8.12		
2013 Oct 07	56572.9	54.6	CARMA E	230.4	126.4 ± 14.2		
2013 Oct 19	56583.5	65.2	B	1.25	< 0.689	4.55	0.23 ± 0.02
			B	1.73	< 0.247	7.38	0.47 ± 0.03
2013 Oct 24	56589.1	70.8	B	1.25	< 0.398	4.55	0.30 ± 0.02
			B	1.73	< 0.335	7.38	0.69 ± 0.04
2013 Oct 26	56591.1		CARMA E	95.7	35.73 ± 3.62		
2013 Oct 26	56591.2	72.9	B	13.54	1.66 ± 0.17	28.21	5.01 ± 0.50
			B	17.44	2.38 ± 0.24	36.53	7.15 ± 0.72
2013 Nov 07	56603.9	85.6	B	1.49	< 0.346	7.38	0.99 ± 0.05
			B	4.55	0.50 ± 0.03		
2013 Nov 09	56605.1	86.8	B	1.49	< 0.420	17.45	3.13 ± 0.31
			B	4.61	0.53 ± 0.03	28.21	6.11 ± 0.61
			B	7.38	0.99 ± 0.05	36.53	8.53 ± 0.85
			B	13.54	2.36 ± 0.24		
2013 Nov 24	56620.9	102.6	B	13.54	2.75 ± 0.28	28.21	7.26 ± 0.73
			B	17.45	3.86 ± 0.39	36.53	9.87 ± 0.99
2013 Nov 28	56624.0	105.7	CARMA E	95.7	51.75 ± 5.25		
2013 Nov 29	56625.9	107.6	B	1.49	< 0.327	7.38	1.30 ± 0.07
			B	4.55	0.70 ± 0.04		
2013 Dec 05	56631.8		B	13.54	2.89 ± 0.29	28.21	6.12 ± 0.62
			B	17.45	3.82 ± 0.38	36.53	6.75 ± 0.68
2013 Dec 16	56642.9	124.6	B	1.49	< 1.06	7.38	1.42 ± 0.07
			B	4.55	0.78 ± 0.04		

Table B.1: Flux densities of V339 Del obtained using VLA and CARMA telescopes.

Date of observation	t (MJD)	$t-t_0$ (Days)	Array configuration	Frequency (GHz)	S_ν (mJy)	Frequency (GHz)	S_ν (mJy)
2013 Dec 22	56649.0	131.0	B	1.49	< 0.528	17.45	4.95 ± 0.50
			B	4.55	0.76 ± 0.05	28.21	9.90 ± 0.99
			B	7.38	1.48 ± 0.08	36.53	14.57 ± 1.46
			B	13.54	3.43 ± 0.34		
2014 Jan 5	56662.8		CARMA E	95.7	60.27 ± 6.05		
2014 Jan 10	56666.9	148.6	B	13.54	3.24 ± 0.32	28.21	5.93 ± 0.59
			B	17.45	4.41 ± 0.44	36.53	7.80 ± 0.78
2014 Jan 11	56667.9	149.6	B	1.49	< 0.958	7.38	1.61 ± 0.08
			B	4.55	0.87 ± 0.05		
2014 Jan 20	56708.5	190.2	CARMA D	95.7	50.96 ± 5.16		
2014 Feb 21	56709.7		CARMA D	95.7	48.77 ± 4.91		
2014 Mar 02	56718.7	200.4	A	1.49	< 0.385	7.38	1.82 ± 0.09
			B	4.55	0.87 ± 0.05		
2014 Mar 09	56725.7	207.4	A	13.54	4.38 ± 0.44	28.21	14.08 ± 1.41
			A	17.45	6.02 ± 0.60	36.53	15.99 ± 1.61
2014 Mar 23	56739.5	221.2	A	29.5	13.65 ± 1.37	35.0	15.32 ± 1.53
2014 Mar 24	56740.8		CARMA C	230.4	39.0 ± 9.08		
2014 Mar 25	56741.6		CARMA C	230.4	35.59 ± 4.10		
2014 Apr 10	56757.4	239.1	A	4.55	0.86 ± 0.05	7.38	1.73 ± 0.09
2014 Apr 12	56759.5	241.2	A	13.54	4.72 ± 0.47	29.5	14.17 ± 1.42
			A	17.45	6.70 ± 0.67	36.5	16.64 ± 1.67
2014 Apr 25	56773.0	254.3	A	1.26	< 0.281	13.54	4.92 ± 0.49
			A	1.79	0.22 ± 0.048	17.45	6.82 ± 0.68
			A	4.55	0.96 ± 0.05	29.5	17.60 ± 1.76
			A	7.38	1.91 ± 0.10	35.0	21.09 ± 2.11
2014 May 17	56795.0	276.1	A	1.26	< 0.367	7.38	2.02 ± 0.10
			A	1.74	0.179 ± 0.045	29.5	15.30 ± 1.53
			A	4.55	1.01 ± 0.05	35.0	17.90 ± 1.79
2014 Jul 02	56840.2	321.9	D	1.26	< 3.78	4.61	1.17 ± 0.06
			A	1.79	< 0.758	7.38	2.32 ± 0.12
2014 Jul 04	56842.5	324.2	D	13.5	5.89 ± 0.59	28.2	11.80 ± 1.18
			D	17.4	8.02 ± 0.80	36.5	12.60 ± 1.26
2014 Jul 13	56850.2	331.9	D	1.26	< 2.19	4.55	1.03 ± 0.06
			D	1.79	< 0.751	7.38	1.95 ± 0.10
2014 Aug 21	56890.2	371.9	D	13.5	5.87 ± 0.59	28.2	7.71 ± 0.77
			D	17.4	7.41 ± 0.74	36.5	6.68 ± 0.67
2014 Aug 22	56891.1	372.8	D	1.26	< 0.895	4.55	1.08 ± 0.07
			D	1.79	< 0.414	7.38	1.92 ± 0.10
2014 Sep 29	56930.0	411.7	D	1.26	< 1.03	4.55	1.37 ± 0.07
			D	1.79	0.68 ± 0.22	7.38	2.77 ± 0.14
2014 Oct 01	56931.2	412.9	D&C	13.5	5.83 ± 0.58	28.2	8.56 ± 0.86
			D&C	17.4	6.97 ± 0.70	36.5	8.57 ± 0.86
2014 Dec 06	56997.0	478.7	C	1.26	< 1.12	4.55	1.51 ± 0.08
			C	1.74	< 0.433	7.38	2.88 ± 0.15
2014 Dec 13	57004.0	485.7	C	13.5	4.84 ± 0.48	28.2	5.61 ± 0.56
			C	17.4	5.31 ± 0.53	36.5	5.43 ± 0.54

Table B.1: Flux densities of V339 Del obtained using VLA and CARMA telescopes.

Date of observation	t (MJD)	$t-t_0$ (Days)	Array configuration	Frequency (GHz)	S_ν (mJy)	Frequency (GHz)	S_ν (mJy)
2014 Feb 14	57068.0	549.3	B	1.26	< 0.564	13.5	4.20 ± 0.42
			B	1.74	0.45 ± 0.076	17.4	4.45 ± 0.45
			B	4.55	1.78 ± 0.09	28.2	4.56 ± 0.46
			B	7.38	3.01 ± 0.15	36.5	4.39 ± 0.44
2015 Apr 17	57129.6	611.3	B	13.5	3.72 ± 0.37	28.2	3.72 ± 0.37
			B	17.4	3.78 ± 0.38	36.5	3.34 ± 0.34
2015 Apr 18	57130.7	612.4	B	1.26	< 0.898	4.55	1.93 ± 0.10
			B	1.74	0.43 ± 0.092	7.38	3.09 ± 0.16
2015 Apr 26	57229.3	711.0	A	1.26	0.31 ± 0.074	13.5	2.95 ± 0.30
			A	1.74	0.54 ± 0.067	16.5	2.94 ± 0.30
			A	5.0	1.87 ± 0.10	29.5	3.78 ± 0.41
			A	7.0	2.23 ± 0.11	35.0	4.02 ± 0.44
2015 Sep 11	57276.2	757.9	A	13.5	2.55 ± 0.26	29.5	2.93 ± 0.30
			A	16.5	2.55 ± 0.26	35.0	3.06 ± 0.31
2015 Nov 20	57346.0	827.7	D	1.26	< 1.60	13.5	2.09 ± 0.21
			D	1.77	< 1.06	16.5	2.07 ± 0.21
			D	5.0	1.69 ± 0.09	29.5	2.08 ± 0.21
			D	7.0	2.00 ± 0.10	35.0	2.03 ± 0.21
2016 Jan 10	57397.9	879.6	D	5.0	1.74 ± 0.09	16.5	1.93 ± 0.19
			D	7.0	1.89 ± 0.10	29.5	1.62 ± 0.16
			D	13.5	1.92 ± 0.19	35.0	1.68 ± 0.17
2016 Apr 02	57480.7	962.4	C	1.26	< 2.25	13.5	1.63 ± 0.16
			C	1.74	< 0.689	16.5	1.64 ± 0.16
			C	5.0	1.50 ± 0.08	29.5	1.60 ± 0.16
			C	7.0	1.59 ± 0.08	35.0	1.54 ± 0.16
2016 Jul 12	57581.4	1063.1	B	1.26	< 1.08	13.5	1.30 ± 0.13
			B	1.74	0.62 ± 0.10	16.5	1.37 ± 0.14
			B	5.0	1.36 ± 0.07	29.5	1.23 ± 0.14
			B	7.0	1.35 ± 0.069	35.0	1.29 ± 0.14
2016 Oct 10	57671.1	1152.8	A	1.26	0.50 ± 0.081	13.5	1.17 ± 0.12
			A	1.74	0.60 ± 0.049	16.5	1.26 ± 0.13
			A	5.0	1.22 ± 0.06	29.5	1.24 ± 0.13
			A	7.0	1.04 ± 0.05	35.0	1.48 ± 0.15
2016 Nov 25	57718.0	1199.7	A	1.26	0.45 ± 0.057	13.5	1.05 ± 0.11
			A	1.74	0.71 ± 0.048	16.5	1.12 ± 0.11
			A	5.0	1.17 ± 0.06	29.5	1.02 ± 0.10
			A	7.0	0.79 ± 0.04	35.0	1.40 ± 0.14
2017 Jan 13	57766.9	1248.6	A	1.26	0.35 ± 0.049	13.5	1.10 ± 0.11
			A	1.74	0.71 ± 0.05	16.5	1.02 ± 0.10
			A	5.0	1.11 ± 0.06	29.5	1.55 ± 0.16
			A	7.0	1.05 ± 0.05	35.0	1.76 ± 0.18
2017 April 22	57865.6	1347.3	D	1.26	< 1.10	13.5	0.80 ± 0.08
			D	1.74	< -0.085	16.5	0.79 ± 0.08
			D	5.0	0.77 ± 0.05	29.5	0.72 ± 0.08
			D	7.0	0.77 ± 0.04	35.0	0.68 ± 0.08
2017 Jul 08	57942.2	1423.9	C	1.26	< 1.27	13.5	0.60 ± 0.06
			C	1.74	0.97 ± 0.16	16.5	0.60 ± 0.06
			C	5.0	0.69 ± 0.04	29.5	0.38 ±0.05
			C	7.0	0.72 ± 0.04	35.0	0.33 ± 0.05

Table B.2: Flux densities of V339 Del obtained with the AMI-LA telescope

Date of observation	t (MJD)	$t-t_0$ (Days)	S_ν mJy	Date of observation	t (MJD)	$t-t_0$ (Days)	S_ν (mJy)
2013 Aug 26	56530.0	11.7	< 0.402	2014 Jan 25	56682.5	164.2	6.52 ± 0.37
2013 Aug 26	56530.9	12.6	< 0.354	2014 Jan 28	56685.4	167.1	6.55 ± 0.36
2013 Aug 27	56531.0	12.7	< 0.403	2014 Jan 31	56688.5	170.2	6.78 ± 0.38
2013 Aug 28	56532.0	13.7	< 0.422	2014 Feb 03	56691.5	173.2	6.42 ±0.39
2013 Aug 29	56533.9	15.6	< 0.415	2014 Feb 10	56698.4	180.1	7.14 ± 0.45
2013 Sep 01	56536.1	17.8	< 0.494	2014 Feb 13	56701.4	183.1	7.20 ± 0.39
2013 Sep 02	56537.9	19.6	< 0.435	2014 Feb 16	56704.5	186.2	6.93 ± 0.41
2013 Sep 04	56539.9	21.6	< 0.296	2014 Feb 21	56709.5	191.2	6.01 ± 0.41
2013 Sep 07	56542.9	24.6	< 0.439	2014 Feb 24	56712.5	194.2	6.46 ± 0.38
2013 Sep 16	56552.0	33.7	< 0.431	2014 Feb 27	56715.4	197.1	5.90 ± 0.35
2013 Sep 19	56554.8	36.5	< 0.366	2014 Mar 02	56718.5	200.2	6.57 ± 0.37
2013 Sep 22	56557.8	39.5	< 0.422	2014 Mar 05	56721.4	203.1	6.10 ± 0.40
2013 Sep 25	56560.9	42.6	< 0.442	2014 Mar 08	56724.4	206.1	7.16 ± 0.40
2013 Sep 27	56562.9	44.6	< 0.552	2014 Mar 10	56726.5	208.2	5.75 ± 0.69
2013 Sep 29	56564.9	46.6	0.64 ± 0.13	2014 Mar 11	56727.2	208.9	7.22 ± 0.42
2013 Oct 01	56566.9	48.6	0.84 ± 0.15	2014 Mar 12	56728.3	210.0	7.23 ± 0.39
2013 Oct 04	56569.8	51.5	1.02 ± 0.16	2014 Mar 15	56731.4	213.1	7.01 ± 0.40
2013 Oct 06	56571.7	53.4	0.98 ± 0.11	2014 Mar 17	56733.4	215.1	7.04 ± 0.39
2013 Oct 08	56573.8	55.5	1.09 ± 0.15	2014 Mar 22	56738.4	220.1	7.26 ± 0.44
2013 Oct 14	56579.8	61.5	1.60 ± 0.14	2014 Mar 24	56740.4	222.1	7.12 ± 0.42
2013 Oct 16	56581.8	63.5	1.87 ± 0.18	2014 Mar 26	56742.4	224.1	7.41 ± 0.42
2013 Oct 19	56584.8	66.5	1.92 ± 0.16	2014 Mar 28	56744.4	226.1	7.09 ± 0.43
2013 Oct 22	56587.9	69.6	2.27 ± 0.34	2014 Mar 31	56747.3	229.0	7.62 ± 0.44
2013 Oct 24	56589.8	71.5	2.59 ± 0.17	2014 Apr 02	56749.4	231.1	7.42 ± 0.45
2013 Oct 30	56595.8	77.5	2.86 ± 0.22	2014 Apr 05	56752.3	234.0	7.30 ± 0.42
2013 Nov 01	56597.8	79.5	3.09 ± 0.19	2014 Apr 08	56755.3	237.0	7.80 ± 0.46
2013 Nov 05	56601.8	83.5	3.57 ± 0.23	2014 Apr 12	56759.3	241.0	6.85 ± 0.43
2013 Nov 08	56604.8	86.5	4.36 ± 0.33	2014 Apr 15	56762.3	244.0	7.45 ± 0.43
2013 Nov 14	56610.8	92.5	3.97 ± 0.26	2014 Apr 19	56766.3	248.0	7.52 ± 0.43
2013 Nov 20	56616.8	98.5	4.54 ± 0.42	2014 Apr 22	56769.4	251.1	7.62 ± 0.55
2013 Nov 22	56618.7	100.4	4.38 ± 0.31	2014 Apr 28	56775.3	257.0	7.41 ±0.42
2013 Nov 24	56620.7	102.4	3.70 ± 0.24	2014 May 01	56778.3	260.0	6.85 ± 0.58
2013 Nov 29	56625.7	107.4	3.95 ± 0.24	2014 May 04	56781.2	262.9	8.29 ± 0.46
2013 Dec 02	56628.7	110.4	3.85 ± 0.23	2014 May 07	56784.2	265.9	8.14 ± 0.48
2013 Dec 06	56632.7	114.4	3.85 ± 0.23	2014 May 13	56790.2	271.9	7.86 ± 0.45
2013 Dec 08	56634.7	116.4	4.35 ± 0.27	2014 May 17	56794.2	275.9	7.14 ± 0.44
2013 Dec 11	56637.6	119.3	4.94 ± 0.37	2014 May 19	56796.2	277.9	7.78 ± 0.56
2013 Dec 14	56640.6	122.3	5.0 ± 0.31	2014 May 25	56802.3	284.0	8.62 ± 0.51
2013 Dec 17	56643.6	125.3	4.66 ± 0.33	2014 May 31	56808.2	289.9	8.17 ± 0.49
2013 Dec 20	56646.6	128.3	4.87 ± 0.30	2014 Jun 03	56811.2	292.9	7.64 ± 0.47
2013 Dec 26	56652.6	134.3	5.18 ± 0.34	2014 Jun 07	56815.2	296.9	7.91 ± 0.48
2013 Dec 29	56655.5	137.2	5.64 ± 0.33	2014 Jun 09	56817.1	298.8	7.82 ± 0.49
2014 Jan 05	56662.5	144.2	5.61 ± 0.34	2014 Jun 12	56820.1	301.8	8.46 ± 0.50
2014 Jan 07	56664.6	146.3	5.91 ± 0.42	2014 Jun 15	56823.1	304.8	8.62 ± 0.49
2014 Jan 10	56667.4	149.1	5.91 ± 0.34	2014 Jun 17	56826.0	307.7	8.34 ± 0.49
2014 Jan 13	56670.5	152.2	6.85 ± 0.45	2014 Jun 21	56829.2	310.9	8.81 ± 0.50
2014 Jan 16	56673.6	155.3	5.92 ± 0.40	2014 Jun 23	56832.0	313.7	8.24 ± 0.52
2014 Jan 22	56679.5	161.2	6.24 ± 0.39	2014 Jul 03	56841.1	322.8	8.01 ± 0.48

Table B.2: Flux densities of V339 Del obtained with the AMI-LA telescope

Date of observation	t (MJD)	$t-t_0$ (Days)	S_ν mJy	Date of observation	t (MJD)	$t-t_0$ (Days)	S_ν (mJy)
2014 Jul 04	56842.1	323.8	8.31 ± 0.49	2014 Nov 28	56989.7	471.4	6.51 ± 0.38
2014 Jul 06	56844.0	325.7	8.39 ± 0.50	2014 Dec 05	56996.7	478.4	6.68 ± 0.38
2014 Jul 08	56846.0	327.7	8.61 ± 0.52	2014 Dec 08	56999.6	481.3	7.21 ± 0.40
2014 Jul 11	56849.0	330.7	9.23 ± 0.55	2014 Dec 13	57004.6	486.3	7.28 ± 0.41
2014 Jul 13	56851.0	332.7	8.61 ± 0.52	2014 Dec 19	57010.6	492.3	6.98 ± 0.39
2014 Jul 19	56857.2	338.9	7.97 ± 0.62	2014 Dec 23	57014.7	496.4	6.60 ± 0.42
2014 Jul 21	56859.1	340.8	8.73 ± 0.54	2014 Dec 31	57022.6	504.3	6.05 ± 0.39
2014 Jul 24	56862.0	343.7	7.91 ± 0.45	2015 Jan 06	57028.6	510.3	6.08 ± 0.39
2014 Jul 27	56865.1	346.8	7.69 ± 0.48	2015 Jan 22	57044.6	526.3	4.17 ± 0.24
2014 Jul 30	56868.0	349.7	7.93 ± 0.48	2015 Feb 13	57066.4	548.1	4.18 ± 0.25
2014 Aug 02	56871.0	352.7	7.71 ± 0.46	2015 Feb 15	57068.5	550.2	4.14 ± 0.23
2014 Aug 05	56875.0	356.7	8.08 ± 0.49	2015 Feb 21	57074.4	556.1	4.30 ± 0.27
2014 Aug 08	56877.1	358.8	8.95 ± 0.53	2015 Feb 27	57080.3	562.0	4.03 ± 0.24
2014 Aug 12	56881.9	363.6	9.51 ± 0.53	2015 Mar 01	57082.3	564.0	4.01 ± 0.23
2014 Aug 14	56884.0	365.7	8.30 ± 0.49	2015 Mar 06	57087.3	569.0	3.74 ± 0.22
2014 Aug 16	56886.0	367.7	8.66 ± 0.48	2015 Mar 11	57092.3	574.0	3.68 ± 0.21
2014 Aug 19	56888.8	370.5	9.10 ± 0.51	2015 Mar 19	57100.4	582.1	3.49 ± 0.22
2014 Aug 22	56891.0	372.7	9.61 ± 0.58	2015 Mar 27	57108.4	590.1	3.50 ± 0.25
2014 Aug 26	56895.0	376.7	8.90 ± 0.82	2015 Apr 01	57113.4	595.1	2.90 ± 0.25
2014 Aug 28	56897.9	379.6	8.20 ± 0.48	2015 Apr 07	57119.2	600.9	3.83 ± 0.23
2014 Aug 31	56900.9	382.6	8.16 ± 0.49	2015 Apr 11	57123.2	604.9	3.45 ± 0.22
2014 Sep 03	56903.9	385.6	9.0 ± 0.49	2015 Apr 14	57126.2	607.9	3.41 ± 0.20
2014 Sep 06	56906.8	388.5	8.06 ± 0.51	2015 Apr 17	57129.2	610.9	3.51 ± 0.20
2014 Sep 09	56909.9	391.6	7.69 ± 0.45	2015 Apr 23	57135.1	616.8	3.43 ± 0.21
2014 Sep 11	56911.8	393.5	8.23 ± 0.47	2015 May 01	57143.2	624.9	3.50 ± 0.21
2014 Sep 14	56914.9	396.6	7.64 ± 0.46	2015 May 08	57150.3	632.0	2.95 ± 0.18
2014 Sep 16	56916.9	398.6	7.54 ± 0.46	2015 May 12	57154.1	635.8	3.21 ± 0.20
2014 Sep 19	56919.9	401.6	7.76 ± 0.45	2015 May 16	57158.1	639.8	3.54 ± 0.22
2014 Sep 24	56924.9	406.6	7.74 ± 0.44	2015 May 17	57159.2	640.9	2.98 ± 0.19
2014 Oct 01	56931.9	413.6	7.66 ± 0.51	2015 May 23	57165.2	646.9	3.08 ± 0.21
2014 Oct 10	56940.8	422.5	6.79 ± 0.40	2015 May 29	57171.1	652.8	3.28 ± 0.19
2014 Oct 16	56946.7	428.4	7.57 ± 0.42	2015 Jun 09	57182.1	663.8	3.04 ± 0.18
2014 Nov 01	56962.8	444.5	6.87 ± 0.40	2015 Jun 26	57199.1	680.8	2.69 ± 0.17
2014 Nov 06	56967.7	449.4	5.78 ± 0.33	2015 Jul 07	57210.0	691.7	2.65 ± 0.23
2014 Nov 12	56973.7	455.4	5.31 ± 0.30	2015 Jul 19	57222.1	703.8	2.66 ± 0.26

References

Abdo A. A., et al., 2010, Science, 329, 817

Ackermann M., et al., 2014, Science, 345, 554

Adelberger E. G., et al., 2011, Reviews of Modern Physics, 83, 195

Anderson G., Fender R., Chomiuk L., Staley T., 2013, The Astronomer's Telegram, 5428, 1

Anderson G. E., et al., 2018, MNRAS, 473, 1512

Andrea J., Drechsel H., Starrfield S., 1994, A&A, 291, 869

Anupama G. C., Mikołajewska J., 1999, A&A, 344, 177

Anupama G. C., Sethi S., 1994, MNRAS, 269, 105

Anupama G. C., et al., 2013, A&A, 559, A121

Ashok N. M., Banerjee D. P. K., 2001, IAU Circ., 7559, 2

Ashok N. M., Banerjee D. P. K., 2003, A&A, 409, 1007

Aydi E., 2018, PhD thesis, University of Cape Town

Aydi E., et al., 2019, arXiv e-prints, p. arXiv:1903.09232

Aydi E., et al., 2020, Nature Astronomy, 4, 776

Bailer-Jones C. A. L., Rybizki J., Fouesneau M., Mantelet G., Andrae R., 2018, AJ, 156, 58

Banerjee D. P. K., Joshi V., Venkataraman V., Ashok N. M., Marion G. H., Hsiao E. Y., Raj A., 2014, ApJ, 785, L11

Bath G. T., Shaviv G., 1976, MNRAS, 175, 305

Bell A. R., 1978, MNRAS, 182, 147

Bell A. R., 2004, MNRAS, 353, 550

Blandford R. D., Ostriker J. P., 1978, ApJ, 221, L29

Blandford R., Meier D., Readhead A., 2019, ARA&A, 57, 467

Bock D. C. J., et al., 2006, in Stepp L. M., ed., Society of Photo-Optical Instrumentation Engineers (SPIE) Conference Series Vol. 6267, Society of Photo-Optical Instrumentation Engineers (SPIE) Conference Series. p. 626713, doi:10.1117/12.674051

Bode M. F., 2002, in Hernanz M., José J., eds, American Institute of Physics Conference Series Vol. 637, Classical Nova Explosions. pp 497–508 (arXiv:astro-ph/0211437), doi:10.1063/1.1518252

Bode M. F., 2004, in Meixner M., Kastner J. H., Balick B., Soker N., eds, Astronomical Society of the Pacific Conference Series Vol. 313, Asymmetrical Planetary Nebulae III: Winds, Structure and the Thunderbird. p. 504 (arXiv:astro-ph/0310068)

Bode M. F., 2010, Astronomische Nachrichten, 331, 160

Bode M. F., Evans A., 2008, Classical Novae, 2 edn. Cambridge Astrophysics, Cambridge University Press, doi:10.1017/CBO9780511536168

Bode M. F., Kahn F. D., 1985, MNRAS, 217, 205

Bode M. F., et al., 2006, ApJ, 652, 629

Booth R. A., Mohamed S., Podsiadlowski P., 2016, MNRAS, 457, 822

Brandi E., Quiroga C., Mikołajewska J., Ferrer O. E., García L. G., 2009, A&A, 497, 815

Buckley D. A. H., Wargau W. F., Soltynski M. G., Shao C. Y., Hazen M. L., 1990, IAU Circ., 5019, 1

Buson S., Jean P., Cheung C. C., 2019, The Astronomer's Telegram, 13114, 1

Cassisi S., Iben Icko J., Tornambè A., 1998, ApJ, 496, 376

Cendes Y., Drout M. R., Chomiuk L., Sarbadhicary S. K., 2020, ApJ, 894, 39

Chandrasekhar S., 1931, ApJ, 74, 81

Chauhan J., et al., 2021, MNRAS, 501, L60

Chesneau O., et al., 2012, A&A, 545, A63

Cheung C. C., et al., 2016, ApJ, 826, 142

Chevalier R. A., 1981, ApJ, 251, 259

Chevalier R. A., 1982a, ApJ, 258, 790

Chevalier R. A., 1982b, ApJ, 259, 302

Chevalier R. A., 1998, ApJ, 499, 810

Chevalier R. A., Fransson C., 2006, ApJ, 651, 381

Chomiuk L., et al., 2012, ApJ, 750, 164

Chomiuk L., et al., 2013a, The Astronomer's Telegram, 5298, 1

Chomiuk L., et al., 2013b, The Astronomer's Telegram, 5382, 1

Chomiuk L., et al., 2014, Nature, 514, 339

Chomiuk L., et al., 2016, ApJ, 821, 119

Cunningham T., Wolf W. M., Bildsten L., 2015, ApJ, 803, 76

Darnley M. J., Ribeiro V. A. R. M., Bode M. F., Hounsell R. A., Williams R. P., 2012, ApJ, 746, 61

Darnley M. J., Williams S. C., Bode M. F., Henze M., Ness J. U., Shafter A. W., Hornoch K., Votruba V., 2014, A&A, 563, L9

Darnley M. J., et al., 2019, Nature, 565, 460

Derdzinski A. M., Metzger B. D., Lazzati D., 2017, mnras, 469, 1314

Diaz M. P., Bruch A., 1997, A&A, 322, 807

Diaz M. P., Abraham Z., Ribeiro V. A. R. M., Beaklini P. P. B., Takeda L., 2018, MNRAS, 480, L54

Dickinson C., et al., 2004, MNRAS, 353, 732

Dilday B., et al., 2012, Science, 337, 942

Duerbeck H. W., 2008, CAMBRIDGE ASTROPHYSICS SERIES, 43, 1

Eckart A., Witzel A., Biermann P., Johnston K. J., Simon R., Schalinski C., Kuhr H., 1986, A&A, 168, 17

Evans A., Banerjee D. P. K., Geballe T. R., Joshi V., Woodward C. E., Gehrz R. D., 2019, The Astronomer's Telegram, 13088, 1

Eyres S. P. S., Davis R. J., Bode M. F., 1996, MNRAS, 279, 249

Eyres S. P. S., et al., 2009, MNRAS, 395, 1533

Ferland G. J., 2003, ARA&A, 41, 517

Finzell T. M. B., 2017, PhD thesis, Michigan State University

Finzell T., et al., 2018, ApJ, 852, 108

Foley R. J., et al., 2012, ApJ, 752, 101

Franckowiak A., Jean P., Wood M., Cheung C. C., Buson S., 2018, A&A, 609, A120

Friedjung M., 1966, MNRAS, 132, 317

Gallagher J. S., Starrfield S., 1976, MNRAS, 176, 53

Gallagher J. S., Starrfield S., 1978, ARA&A, 16, 171

Gehrz R. D., 1988, ARA&A, 26, 377

Gehrz R. D., et al., 2015, ApJ, 812, 132

Geisel S. L., Kleinmann D. E., Low F. J., 1970, ApJ, 161, L101

Gill C. D., O'Brien T. J., 1998, MNRAS, 300, 221

Gill C. D., O'Brien T. J., 2000, MNRAS, 314, 175

Gonzalez-Riestra R., 1992, A&A, 265, 71

Gordon A. C., Aydi E., Page K. L., Li K.-L., Chomiuk L., Sokolovsky K. V., Mukai K., Seitz J., 2020, arXiv e-prints, p. arXiv:2010.15930

Green G. M., Schlafly E., Zucker C., Speagle J. S., Finkbeiner D., 2019, ApJ, 887, 93

Greisen E. W., 2003, AIPS, the VLA, and the VLBA. p. 109, doi:10.1007/0-306-48080-8_7

Gutierrez J., Garcia-Berro E., Iben Icko J., Isern J., Labay J., Canal R., 1996, ApJ, 459, 701

Hachisu I., Kato M., 2006, ApJS, 167, 59

Hameury J. M., 2020, Advances in Space Research, 66, 1004

Harman D. J., O'Brien T. J., 2003, MNRAS, 344, 1219

Harris C. E., Nugent P. E., Kasen D. N., 2016, ApJ, 823, 100

Harrison T. E., Johnson J. J., Spyromilio J., 1993, AJ, 105, 320

Hauschildt P. H., Shore S. N., Schwarz G. J., Baron E., Starrfield S., Allard F., 1997, ApJ, 490, 803

Hays E., Cheung T., Ciprini S., 2013, The Astronomer's Telegram, 5302, 1

Hellier C., 2001, Cataclysmic Variable Stars-how and why they vary. Springer Science & Business Media

Henze M., et al., 2014, A&A, 563, A2

Hernanz M., 2005, in Hameury J. M., Lasota J. P., eds, Astronomical Society of the Pacific Conference Series Vol. 330, The Astrophysics of Cataclysmic Variables and Related Objects. p. 265 (arXiv:astro-ph/0412333)

Hernanz M., José J., 2004, New A Rev., 48, 35

Hewitt D. M., et al., 2020, MNRAS, 496, 2542

Heywood I., O'Brien T. J., 2007, MNRAS, 379, 1453

Heywood I., O'Brien T. J., Eyres S. P. S., Bode M. F., Davis R. J., 2005, MNRAS, 362, 469

Hickish J., et al., 2018, MNRAS, 475, 5677

Hillman Y., Prialnik D., Kovetz A., Shara M. M., 2016, ApJ, 819, 168

Hjellming R. M., 1996, in Taylor A. R., Paredes J. M., eds, Astronomical Society of the Pacific Conference Series Vol. 93, Radio Emission from the Stars and the Sun. p. 174

Hjellming R. M., Wade C. M., Vandenberg N. R., Newell R. T., 1979, AJ, 84, 1619

Hjellming R. M., van Gorkom J. H., Taylor A. R., Sequist E. R., Padin S., Davis R. J., Bode M. F., 1986, ApJ, 305, L71

Hoffmann S. M., Vogt N., Protte P., 2020, Astronomische Nachrichten, 341, 79

Hounsell R., et al., 2010, ApJ, 724, 480

Hoyle F., Fowler W. A., 1960, ApJ, 132, 565

Hric L., Petrík K., Urban Z., Hanžl D., 1998, A&AS, 133, 211

Hutchings J. B., 1972, MNRAS, 158, 177

Hyland A. R., Neugebauer G., 1970, ApJ, 160, L177

Iben I. J., 2003, in Corradi R. L. M., Mikolajewska J., Mahoney T. J., eds, Astronomical Society of the Pacific Conference Series Vol. 303, Symbiotic Stars Probing Stellar Evolution. p. 177

Iben Icko J., Tutukov A. V., 1991, ApJ, 370, 615

Iben Icko J., Tutukov A. V., 1994, ApJ, 431, 264

Iijima T., Nakanishi H., 2008, A&A, 482, 865

Irwin J. A., 2007, Astrophysics: Decoding the Cosmos. Chichester: Wiley

Jack D., et al., 2017, Astronomische Nachrichten, 338, 91

Jansky K. G., 1933, Popular Astronomy, 41, 548

Jiang J.-A., et al., 2017, Nature, 550, 80

Jonas J., MeerKAT Team 2016, in MeerKAT Science: On the Pathway to the SKA. p. 1

José J., 2012, Bulletin of the Astronomical Society of India, 40, 443

Jose J., 2016, Stellar explosions: hydrodynamics and nucleosynthesis. CRC Press

José J., Hernanz M., Iliadis C., 2006, Nucl. Phys. A, 777, 550

Jurdana-Šepić R., Ribeiro V. A. R. M., Darnley M. J., Munari U., Bode M. F., 2012, A&A, 537, A34

Kafka S., 2020, Observations from the AAVSO International Database, https://www.aavso.org

Kantharia N. G., 2012, Bulletin of the Astronomical Society of India, 40, 311

Kantharia N. G., et al., 2016, MNRAS, 456, L49

Kato M., Hachisu I., 1994, ApJ, 437, 802

Kato M., Hachisu I., 2004, ApJ, 613, L129

Kato M., Saio H., Hachisu I., 1989, ApJ, 340, 509

Kato T., Kanatsu K., Takamizawa K., Takao A., Stubbings R., 2000, IAU Circ., 7552, 1

Kawakita H., Shinnaka Y., Arai A., Arasaki T., Ikeda Y., 2019, ApJ, 872, 120

Kelly P. L., et al., 2014, ApJ, 790, 3

Kenyon S. J., Garcia M. R., 1986, AJ, 91, 125

Knigge C., Baraffe I., Patterson J., 2011, ApJS, 194, 28

Koester D., Chanmugam G., 1990, Reports on Progress in Physics, 53, 837

Kolotilov E. A., 1980, Soviet Astronomy Letters, 6, 268

Kovetz A., Prialnik D., 1997, ApJ, 477, 356

Krauss M. I., et al., 2011, ApJ, 739, L6

Krautter J., Oegelman H., Starrfield S., Wichmann R., Pfeffermann E., 1996, ApJ, 456, 788

Kuin P., et al., 2019, The Astronomer's Telegram, 13072, 1

Kundu E., Lundqvist P., Pérez-Torres M. A., Herrero-Illana R., Alberdi A., 2017, ApJ, 842, 17

Kwok S., 2007, Physics and chemistry of the interstellar medium. University Science Books

Lallement R., Vergely J. L., Valette B., Puspitarini L., Eyer L., Casagrande L., 2014, A&A, 561, A91

Lamers H. J. G. L. M., Levesque E. M., 2017, Understanding Stellar Evolution. IoP Publishing Bristol

Lang K. R., 1980, Astrophysical Formulae. A Compendium for the Physicist and Astrophysicist. Springer study edition, Springer-Verlag

Li W., et al., 2011, Nature, 480, 348

Linford J. D., et al., 2015, ApJ, 805, 136

Linford J. D., et al., 2017, ApJ, 842, 73

Livio M., Shankar A., Burkert A., Truran J. W., 1990, ApJ, 356, 250

Livne E., 1990, ApJ, 354, L53

Lloyd H. M., O'Brien T. J., Bode M. F., 1997, MNRAS, 284, 137

Luna G. J. M., 2019, Boletin de la Asociacion Argentina de Astronomia La Plata Argentina, 61, 93

Lundqvist P., et al., 2020, ApJ, 890, 159

Lynch D. K., Russell R. W., Sitko M. L., 2001, AJ, 122, 3313

Lynch D. K., Rudy R. J., Mazuk S., Venturini C. C., Puetter R. C., Perry R. B., 2004, AJ, 128, 2962

MacDonald J., 1984, ApJ, 283, 241

MacDonald J., 1996, Classical nova evolution: clues from soft X-ray emission. Cambridge University Press, p. 281, doi:10.1007/978-94-009-0325-8_82

MacDonald J., Fujimoto M. Y., Truran J. W., 1985, ApJ, 294, 263

Maoz D., Mannucci F., Nelemans G., 2014, ARA&A, 52, 107

Martin P., Dubus G., 2013, A&A, 551, A37

Martin P., Dubus G., Jean P., Tatischeff V., Dosne C., 2018, A&A, 612, A38

Mason E., Della Valle M., Gilmozzi R., Lo Curto G., Williams R. E., 2005, A&A, 435, 1031

Mason E., Ederoclite A., Williams R. E., Della Valle M., Setiawan J., 2012, A&A, 544, A149

Mason E., Shore S. N., De Gennaro Aquino I., Izzo L., Page K., Schwarz G. J., 2018, ApJ, 853, 27

McCully C., et al., 2014, Nature, 512, 54

McLaughlin D. B., 1939, Popular Astronomy, 47, 410

McLaughlin D. B., 1964, Annales d'Astrophysique, 27, 450

McMullin J. P., Waters B., Schiebel D., Young W., Golap K., 2007, in Shaw R. A., Hill F., Bell D. J., eds, Astronomical Society of the Pacific Conference Series Vol. 376, Astronomical Data Analysis Software and Systems XVI. p. 127

Metzger B. D., Hascoët R., Vurm I., Beloborodov A. M., Chomiuk L., Sokoloski J. L., Nelson T., 2014, MNRAS, 442, 713

Metzger B. D., Finzell T., Vurm I., Hascoët R., Beloborodov A. M., Chomiuk L., 2015, MNRAS, 450, 2739

Mezger P. G., Henderson A. P., 1967, ApJ, 147, 471

Mikolajewska J., 2010, arXiv e-prints, p. arXiv:1011.5657

Miller L. T. P., 1991, Journal of the American Association of Variable Star Observers (JAAVSO), 20, 182

Miszalski B., et al., 2016, MNRAS, 456, 633

Mohamed S., Podsiadlowski P., 2007, in Napiwotzki R., Burleigh M. R., eds, Astronomical Society of the Pacific Conference Series Vol. 372, 15th European Workshop on White Dwarfs. p. 397

Mohamed S., Booth R., Podsiadlowski P., 2013, in Di Stefano R., Orio M., Moe M., eds, Vol. 281, Binary Paths to Type Ia Supernovae Explosions. pp 195–198, doi:10.1017/S1743921312014998

Mohamed S., Booth R., Podsiadlowski P., Ramstedt S., Vlemmings W., Maercker M., 2015, in EAS Publications Series. pp 81–86, doi:10.1051/eas/1571015

Moll R., Woosley S. E., 2013, ApJ, 774, 137

Mondal A., Anupama G. C., Kamath U. S., Das R., Selvakumar G., Mondal S., 2018, MNRAS, 474, 4211

Moraes M., Diaz M., 2011, PASP, 123, 844

Mukai K., Ishida M., 2001, ApJ, 551, 1024

Mukai K., Orio M., Della Valle M., 2008, ApJ, 677, 1248

Munari U., 2019, The Symbiotic Stars. Cambridge University Press, pp 77–91, doi:10.1017/9781108553070.008

Munari U., Walter F. M., 2019a, The Astronomer's Telegram, 13069, 1

Munari U., Walter F. M., 2019b, The Astronomer's Telegram, 13081, 1

Munari U., Henden A., Dallaporta S., Cherini G., 2013, Information Bulletin on Variable Stars, 6080

Munari U., Henden A., Banerjee D. P. K., Ashok N. M., Righetti G. L., Dallaporta S., Cetrulo G., 2015, MNRAS, 447, 1661

Mürset U., Schmid H. M., 1999, A&AS, 137, 473

Mustel E. R., Boyarchuk A. A., 1970, Ap&SS, 6, 183

Nakano S., et al., 2013, Central Bureau Electronic Telegrams, 3628, 1

Nelson T., et al., 2014, ApJ, 785, 78

Nogami D., Kato T., Baba H., 2002, PASJ, 54, 987

Nomoto K., 1982, ApJ, 257, 780

Nyamai M. M., Woudt P. A., Ribeiro V. A. R. M., Chomiuk L., 2019, The Astronomer's Telegram, 13089, 1

O'Brien T., Bode M., 2008, Resolved nebular remnants, 2 edn. Cambridge University Press, pp 285–307, doi:10.1017/CBO9780511536168.014

O'Brien T. J., Bode M. F., Kahn F. D., 1992, MNRAS, 255, 683

O'Brien T. J., Lloyd H. M., Bode M. F., 1994, MNRAS, 271, 155

O'Brien T. J., et al., 2006, Nature, 442, 279

O'Brien T., Rupen M., Chomiuk L., Ribeiro V., Bode M., Sokoloski J., Woudt P. A., 2015, in Advancing Astrophysics with the Square Kilometre Array (AASKA14). p. 62 (arXiv:1502.04927)

Offringa A. R., van de Gronde J. J., Roerdink J. B. T. M., 2012, A&A, 539, A95

Offringa A. R., et al., 2014, MNRAS, 444, 606

Orio M., 1999, Phys. Rep., 311, 419

Orio M., et al., 2020, ApJ, 895, 80

Orlando S., Drake J. J., Miceli M., 2017, MNRAS, 464, 5003

Osborne J. P., et al., 2011, ApJ, 727, 124

Pacholczyk A. G., 1970, Radio astrophysics : Nonthermal processes in galactic and extragalactic sources.. A series of books in astronomy and astrophysics, W. H. Freeman, San Francisco

Paczynski B., 1976, in Eggleton P., Mitton S., Whelan J., eds, IAU Symposium Vol. 73, Structure and Evolution of Close Binary Systems. p. 75

Paczynski B., Sienkiewicz R., 1981, ApJ, 248, L27

Page K. L., Osborne J. P., Kuin N. P. M., Woodward C. E., Schwarz G. J., Starrfield S., Shore S. N., Walter F. M., 2013, The Astronomer's Telegram, 5470, 1

Page K. L., et al., 2015, MNRAS, 454, 3108

Panagia N., Felli M., 1975, A&A, 39, 1

Panagia N., Van Dyk S. D., Weiler K. W., Sramek R. A., Stockdale C. J., Murata K. P., 2006, ApJ, 646, 369

Patat F., et al., 2007, Science, 317, 924

Patat F., Chugai N. N., Podsiadlowski P., Mason E., Melo C., Pasquini L., 2011, A&A, 530, A63

Payne-Gaposchkin C., 1964, The Galactic Novae. Dover Books on Astronomy and Astrophysics, Dover Publications

Pejcha O., Metzger B. D., Tomida K., 2016a, MNRAS, 455, 4351

Pejcha O., Metzger B. D., Tomida K., 2016b, MNRAS, 461, 2527

Pellegrino C., et al., 2020, ApJ, 897, 159

Pérez-Torres M. A., et al., 2014, ApJ, 792, 38

Perrott Y. C., et al., 2013, MNRAS, 429, 3330

Piersanti L., Tornambé A., Yungelson L., Straniero O., 2013, in Di Stefano R., Orio M., Moe M., eds, IAU Symposium Vol. 281, Binary Paths to Type Ia Supernovae Explosions. Cambridge University Press, pp 209–212, doi:10.1017/S1743921312015049

Piersanti L., Tornambé A., Yungelson L. R., 2014, MNRAS, 445, 3239

Polisensky E., et al., 2019, The Astronomer's Telegram, 13185, 1

Prialnik D., Kovetz A., 1995, ApJ, 445, 789

Readhead A. C. S., 1994, ApJ, 426, 51

Reynolds S. P., 2017, Dynamical Evolution and Radiative Processes of Supernova Remnants. Springer International Publishing, Cham, pp 1981–2004, doi:10.1007/978-3-319-21846-5_89, https://doi.org/10.1007/978-3-319-21846-5_89

Ribeiro V. A. R. M., Munari U., Valisa P., 2013, ApJ, 768, 49

Ribeiro V. A. R. M., et al., 2014, ApJ, 792, 57

Roy N., et al., 2012, Bulletin of the Astronomical Society of India, 40, 293

Roy N., Kantharia N. G., Dutta P., Anupama G. C., Ashok N. M., Banerjee D. P. K., 2013, The Astronomer's Telegram, 5376, 1

Ruiter A. J., Belczynski K., Sim S. A., Seitenzahl I. R., Kwiatkowski D., 2014, MNRAS, 440, L101

Rupen M. P., Dhawan V., Mioduszewski A., 2001, IAU Circ., 7717

Rupen M. P., Mioduszewski A. J., Sokoloski J. L., 2008, ApJ, 688, 559

Sarbadhicary S. K., Badenes C., Chomiuk L., Caprioli D., Huizenga D., 2017, MNRAS, 464, 2326

Schaefer B. E., 2009, ApJ, 697, 721

Schaefer B. E., 2010, ApJS, 187, 275

Schaefer B. E., 2018, MNRAS, 481, 3033

Schaefer B. E., Ringwald F. A., 1995, ApJ, 447, L45

Schaefer G. H., et al., 2014, Nature, 515, 234

Seaquist E., Bode M., 2008, Radio emission from novae, 2 edn. Cambridge University Press, pp 141–166, doi:10.1017/CBO9780511536168.009

Seaquist E. R., Palimaka J., 1977, ApJ, 217, 781

Seaquist E. R., Taylor A. R., 1990, ApJ, 349, 313

Seaquist E. R., Duric N., Israel F. P., Spoelstra T. A. T., Ulich B. L., Gregory P. C., 1980, AJ, 85, 283

Shara M. M., Zurek D., De Marco O., Mizusawa T., Williams R., Livio M., 2012, AJ, 143, 143

Shara M. M., et al., 2017, Nature, 548, 558

Shen K. J., Bildsten L., 2009, ApJ, 699, 1365

Shepherd M. C., 1997, in Hunt G., Payne H., eds, Astronomical Society of the Pacific Conference Series Vol. 125, Astronomical Data Analysis Software and Systems VI. p. 77

Shepherd M. C., Pearson T. J., Taylor G. B., 1994, in BAAS. pp 987–989

Shimamoto S., Sakon I., Onaka T., Usui F., Ootsubo T., Doi Y., Ohsawa R., Ishihara D., 2017, Publication of Korean Astronomical Society, 32, 109

Shore S. N., et al., 2016, A&A, 590, A123

Skopal A., 2019, ApJ, 878, 28

Slavin A. J., O'Brien T. J., Dunlop J. S., 1995, MNRAS, 276, 353

Sokoloski J. L., Luna G. J. M., Mukai K., Kenyon S. J., 2006, Nature, 442, 276

Sokoloski J. L., Rupen M. P., Mioduszewski A. J., 2008, ApJ, 685, L137

Sokoloski J. L., Lawrence S., Crotts A. P. S., Mukai K., 2017, arXiv e-prints, p. arXiv:1702.05898

Sokolovsky K. V., et al., 2019, The Astronomer's Telegram, 13050, 1

Solf J., 1983, ApJ, 273, 647

Solheim J. E., 2010, PASP, 122, 1133

Staley T. D., Anderson G. E., 2015, Astronomy and Computing, 13, 38

Stanishev V., Zamanov R., Tomov N., Marziani P., 2004, A&A, 415, 609

Starrfield S., 1996, in APS Meeting Abstracts. p. F4.03

Starrfield S., Sparks W. M., Truran J. W., 1985, ApJ, 291, 136

Starrfield S., Iliadis C., Hix W. R., 2016, PASP, 128, 051001

Starrfield S., Bose M., Iliadis C., Hix W., Woodward C., Wagner R., 2021, Proceedings of Science, 368, 030

Steffen W., Koning N., Wenger S., Morisset C., Magnor M., 2011, IEEE Transactions on Visualization and Computer Graphics, 17, 454

Stephenson F. R., 1976, QJRAS, 17, 121

Strader J., et al., 2019, The Astronomer's Telegram, 13047, 1

Strope R. J., Schaefer B. E., Henden A. A., 2010, AJ, 140, 34

Swinbank J. D., et al., 2015, Astronomy and Computing, 11, 25

Takeda L., Diaz M., 2015, New A, 39, 64

Takei D., Tsujimoto M., Drake J. J., Kitamoto S., 2014, PASJ, 66, 37

Tanaka J., Nogami D., Fujii M., Ayani K., Kato T., 2011, PASJ, 63, 159

Tang X., Chevalier R. A., 2017, MNRAS, 465, 3793

Tarasova T. N., Skopal A., 2016, Astronomy Letters, 42, 10

Taylor A. R., Seaquist E. R., Hollis J. M., Pottasch S. R., 1987, A&A, 183, 38

Taylor A. R., Hjellming R. M., Seaquist E. R., Gehrz R. D., 1988, Nature, 335, 235

Taylor A. R., Davis R. J., Porcas R. W., Bode M. F., 1989, MNRAS, 237, 81

Truran J. W., Livio M., 1986, ApJ, 308, 721

Van Loon J. T., 2008, in Evans A., Bode M. F., O'Brien T. J., Darnley M. J., eds, Astronomical Society of the Pacific Conference Series Vol. 401, RS Ophiuchi (2006) and the Recurrent Nova Phenomenon. p. 90 (arXiv:0710.5628)

Vaytet N. M. H., O'Brien T. J., Bode M. F., 2007, ApJ, 665, 654

Verbunt F., Zwaan C., 1981, A&A, 100, L7

Vlasov A., Vurm I., Metzger B. D., 2016, MNRAS, 463, 394

Waagen E. O., Pearce A., Otero S., Williams P., Camilleri P., 2013, Central Bureau Electronic Telegrams, 3732, 3

Wade R. A., Harlow J. J. B., Ciardullo R., 2000, PASP, 112, 614

Walder R., Folini D., Shore S. N., 2008, A&A, 484, L9

Warner B., 1995, Cambridge Astrophysics Series, 28

Warner B., 2008, Properties of novae: an overview, 2 edn. Cambridge University Press, pp 16–33, doi:10.1017/CBO9780511536168.004

Weiler K. W., Sramek R. A., Panagia N., van der Hulst J. M., Salvati M., 1986, ApJ, 301, 790

Weiler K. W., Panagia N., Montes M. J., Sramek R. A., 2002, ARA&A, 40, 387

Wendeln C., Chomiuk L., Finzell T., Linford J. D., Strader J., 2017, ApJ, 840, 110

Wenger T. V., Balser D. S., Anderson L. D., Bania T. M., 2018, ApJ, 856, 52

Wenzel W., 1990, Information Bulletin on Variable Stars, 3517, 1

Weston J. H. S., et al., 2014, in Woudt P. A., Ribeiro V. A. R. M., eds, Astronomical Society of the Pacific Conference Series Vol. 490, Stellar Novae: Past and Future Decades. p. 339 (arXiv:1306.2265)

Weston J. H. S., et al., 2016a, MNRAS, 457, 887

Weston J. H. S., et al., 2016b, MNRAS, 460, 2687

Whelan J., Iben Icko J., 1973, ApJ, 186, 1007

Williams R. E., 1992, AJ, 104, 725

Williams R., 2013, AJ, 146, 55

Williams R., 2016, in Journal of Physics Conference Series. p. 042001, doi:10.1088/1742-6596/728/4/042001

Wolf W. M., Bildsten L., Brooks J., Paxton B., 2013, ApJ, 777, 136

Woosley S. E., Kasen D., 2011, ApJ, 734, 38

Worters H. L., Eyres S. P. S., Bromage G. E., Osborne J. P., 2007, MNRAS, 379, 1557

Woudt P. A., Ribeiro V. A., 2014, Stella Novae: Past and Future Decades. Astronomical Society of the Pacific

Woudt P. A., Steeghs D., 2005, in Burderi L., Antonelli L. A., D'Antona F., di Salvo T., Israel G. L., Piersanti L., Tornambè A., Straniero O., eds, American Institute of Physics Conference Series Vol. 797, Interacting Binaries: Accretion, Evolution, and Outcomes. pp 647–650, doi:10.1063/1.2130306

Woudt P. A., et al., 2009, ApJ, 706, 738

Wright A. E., Barlow M. J., 1975, MNRAS, 170, 41

Yaron O., Prialnik D., Shara M. M., Kovetz A., 2005, ApJ, 623, 398

Zwart J. T. L., et al., 2008, MNRAS, 391, 1545